Novel Self-Sustained Oscillations and Giant Nonlinearity in Superconducting Resonators

Eran Arbel-Segev

Novel Self-Sustained Oscillations and Giant Nonlinearity in Superconducting Resonators

RESEARCH THESIS

SUBMITTED IN PARTIAL FULFILLMENT OF THE REQUIREMENTS FOR THE DEGREE OF MASTER OF SCIENCE IN ELECTRICAL ENGINEERING

Eran Arbel-Segev

SUBMITTED TO THE SENATE OF THE TECHNION - ISRAEL INSTITUTE OF TECHNOLOGY

SHVAT 5766 HAIFA FEBRUARY 2006

This Research Thesis Was Done Under The Supervision of Doctor Eyal Buks in the Faculty of Electrical Engineering.

THE GENEROUS FINANCIAL HELP OF ALEXAND GERTRUDE ZELIG FELLOWSHIP AND THE TECHNION IS GRATEFULLY ACKNOWLEDGED.

Contents

List of Figures

List of Tables

Abstract

We study microwave superconducting stripline resonators made of NbN on Sapphire substrate. A section in the resonator is made of a narrow and thin meander strip. A continuous wave at frequency close to one of the resonances is injected into the resonator and the reflected power off the resonator is measured. Novel, self-sustained oscillations of the reflected power, at frequencies of down to 0.01 Hz and up to 60 MHz are observed. To the best of our knowledge such oscillations were not reported before in similar systems.

Near the onset of these oscillations the device exhibits a chaotic like behavior and is characterizes by giant nonlinearity. Intermodulation characterization performed in this state yields extremely high intermodulation gain (about 30dB), which is accompanied by a very strong noise squeezing (about 45dB squeezing factor) and period doubling of various orders. We also study the response of the device to IR (1550 nm wavelength) illumination impinging on the meander strip. To characterize the response time of the system we modulate the impinging optical power with a varying frequency. We observe extremely fast (modulation frequencies of up to 8 GHz) and sensitive (optical power below 100 fW) response near the onset of the self-sustained oscillations.

To account for our findings we propose a theoretical model according to which the self-sustained oscillations are originated by thermal instability in the meander strip.

Glossary

Acronyms:

3DFV	Three dimensional flat view
AlN	Aluminium-Nitride
CW	Continuous wave
DI	De-ionized
DTx	Data-Translation digital to analog board
E13,E15,E16	Device number i
EBL	Electron beam lithography
ECR	Electron cyclotron resonance
ED	Exposure dose
HED	Hot-electron detector
HFSM	High frequency self modulations
IM	Intermodulation
LFSO	Low frequency self oscillations
LPF	Low-pass filter
NA	Network analyzer
NbN	Niobium Nitride
NC	Normal conducting
NMP	N-Methyl-2-Pyrrolidone
ORSM	Optical and RF signal mixing
OSC	Time domain oscilloscope
PDB	Period doubling bifurcation
PSA	Phase sensitive amplification
PMMA	PolyMethylMethacrylate
RIE	Reeactive ion etching
SA	Spectrum Analyzer
SC	Superconducting
SE	Self-exitation
SM	Self-modulations
SMA	SubMiniature version A
SYN	Synthesizer
NEP	Noise equivalent power

List of Symbols and abbreviation:

Z_0	Characteristic impedance
c	Speed of light in vacuum
ϵ_r	Dielectric constant of Sapphire
$\|S_{11}\|$	Power reflection coefficient
SF_6	Sulfur Hexafluoride
Al	Aluminium
Cl_2	Chlorine
H_2	Hydrogen
O_2	Oxygen
Cr	Chromium
N_2	Nitogen
Ar	Argon
Al	Aluminium
V_{Cn}	Critical voltage number n
(ω), f	(Angular) Frequency
(ω_0), f_0	(Angular) Resonance frequency
(ω_p), f_p	(Angular) Pump frequency
γ_1	Coupling constant between the resonator and the feedline
γ_2	unloaded damping rate of the resonance
P_{pump}	Pump power
f_{pump}	Pump frequency
P_{refl}	Reflected power
f_{SM}	Self-modulation frequency
nix	Resonance mode number i, index x
G_{sig}^{IM}	Signal intermodulation gain

Chapter 1

Introduction

Resonance parametric amplifiers are characterized by very low noise, high gain, and phase sensitive amplification. Parametric resonance in superconducting (SC) resonators [20] may allow some intriguing applications such as quantum squeezing [59], quantum non-demolition measurements [49], photon creation by the so-called dynamical Casimir effect [18], and more.

Parametric excitation occurs when the resonance frequency of an oscillator varies in time. The first parametric resonance occurs when the excitation is performed periodically at twice the resonance frequency f_0, namely $f(t) = f_0 [1 + \xi \cos(4\pi f_0 t)]$ [34]. The system's response to such an excitation depends on the dimensionless parameter ξQ , where Q is the quality factor of the resonator. When $\xi Q < 1$ the system is said to be in the subthreshold region, while above threshold, when $\xi Q > 1$, the system breaks into oscillation. Achieving parametric gain where $\xi Q > 1$ requires that the shift in the resonance frequency exceeds the width of its peak [23].

Spirited by this motivation, we have designed and manufactured (chapter 2) several novel SC devices, that integrates a hot-electron detector (HED) into a SC ring resonator. The HED is used as an optically tuned, lumped element, that changes the boundary conditions of the resonator [48], and thus manipulates its resonance frequencies. Several external constrains, such as dc voltage and current, RF power, and IR illumination can be applied on the HED. The switching time in superconductors is usually limited by the relaxation process of high-energy quasi-particles, also called 'hot-electrons', giving their energy to the lattice, and recombining to form Cooper pairs. Recent experiments with photodetectors, based on a thin layer of SC niobium nitride (NbN), have demonstrated an intrinsic switching time on the order of 30 ps and a counting rate exceeding 2 GHz (see [24] and references therein).

The resulting effect of applied dc voltage and current as well as continuous wave (CW) IR illumination on the resonance frequencies of the resonators is investigated (chapter 3) and found to be promising. Applying external constrains indeed shifts the resonance frequencies, and the parametric gain threshold condition is achieved in a CW illumination measurement. Moreover, the results are shown to be in a good agreement with a theoretical modeling.

The outcome of the integrated devices is discovered to be much more fruitful than expected. A wide variety of nonlinear phenomenons occur in the devices. Phenomenons such as strong intermodulation gain, quantum squeezing, period doubling

bifurcation and optical and RF signal mixing, are all coexist and observed in all devices (chapter 5). They are all governed by and correlated to novel, self-sustained oscillations of the reflected power, at frequencies of down to 0.01Hz and up to 60MHz, that are a robust behavior, which characterizes our devices (chapter 4). To account for our findings we propose a theoretical model according to which the self-sustained oscillations are originated by thermal instability in the HED.

The outmost goal of achieving parametric gain has not been achieved in this research. The probable cause is insufficient illumination intensity impinging on the HED (subsection 5.6.4), due to dispersion of the laser beam, traveling in free space towards the HED. Future devices, which integrates a Fresnel lens back to back with the HED, would hopefully solve this problem. This devices are already planed, and the Fresnel lenses are in preliminary manufacture stages (A).

Chapter 2

Circuit Design and Fabrication

2.1 Circuit Design

The research is done using three devices, named E13, E15, and E16, which differ in terms of width, layout, and optical detector design, as summarized in table 2.1.The circuit layouts are illustrated in Fig. 2.1(a) for E15, E16 and 2.1(b) for E13. E16 (E13, E15) device is made of 8 nm (200 nm) thick NbN stripline, fabricated on a Sapphire wafer, with dimensions of $34 \times 30 \times 1\,\mathrm{mm}^3$. The design integrates three components. The first is a SC ring resonator and its feedline. Ring configuration is a symmetric and compact geometry, which is generally suitable for applications, which require resonance tuning [9]. The first few resonance frequencies are designed for the S&C bands ($2 - 8\,\mathrm{GHz}$). The resonator is weakly coupled to its feedline, where the coupling gaps are 0.35 mm, 0.45 mm, 0.4 mm for E13, E15, and E16 respectively. The stripline width is set to $347\,\mu\mathrm{m}$, to obtain a characteristic impedance of $Z_0 = 50\,\Omega$.

The second component is a hot electron detector (HED), which is monolithically integrated into the ring structure. Its angular location, relative to the feedline coupling location, maximizes the RF current amplitude flowing through it, and thus maximizes its coupling to the resonator. E16's HED, shown in Fig. 2.1(c), has a $4 \times 4\,\mu\mathrm{m}^2$ meander structure, consists of nine NbN SC strips. Each strip has a characteristic area of $0.15 \times 4\,\mu\mathrm{m}^2$ and the strips are separated one from another by approximately $0.25\,\mu\mathrm{m}$ [61]. E13 and E15 has a simpler HED, shown in Fig. 2.1(d), which has a $10 \times 1\,\mu\mathrm{m}^2$ bridge structure.

The HED operating point is maintained by applying dc bias. The dc bias lines,

Table 2.1: Device Parameters

Device parameter	**E13**	**E15**	**E16**
Thickness (t)	200nm	200nm	8nm
HED Layout	Bridge	Bridge	Meander
HED Area	$1 \times 10\mathrm{m}^2$	$1 \times 10\mathrm{m}^2$	9 strips, each $0.15 \times 4\mu\mathrm{m}^2$
Targeted Resonance Modes	$n1$	$n2, n3$	$n2, n3$

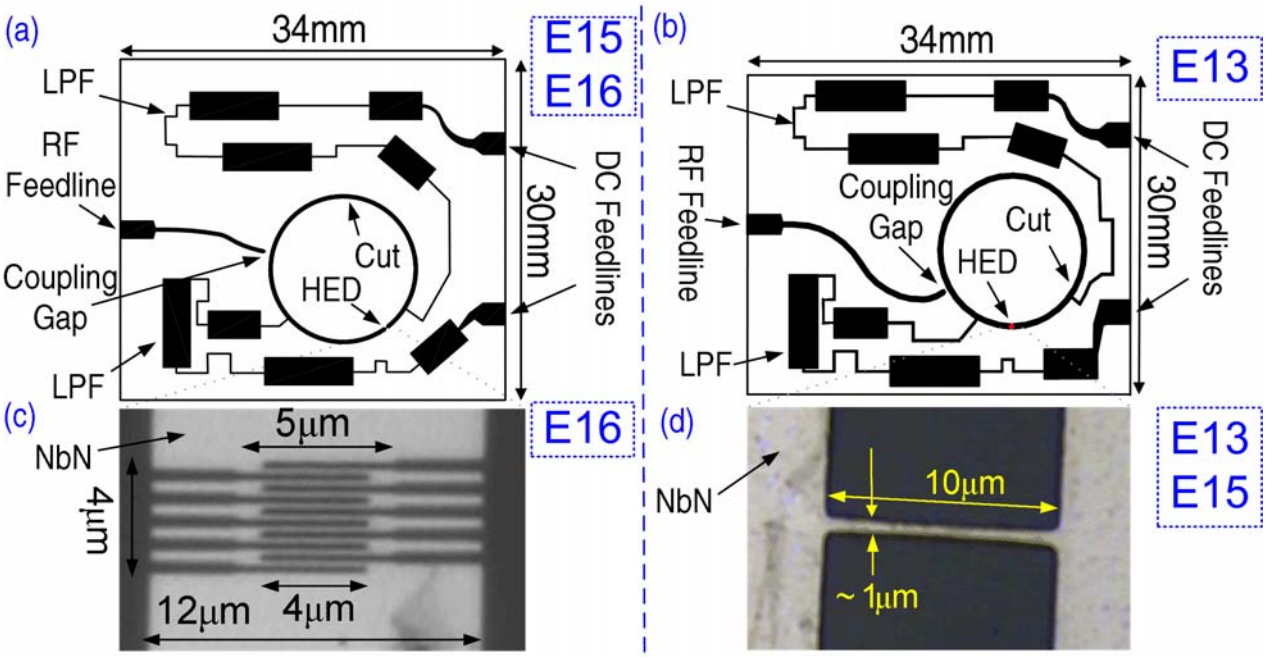

Figure 2.1: (a) E16, E15 and (b) E13 devices' layouts. (c) E16 and (d) E13, E15 optical microscope images of the HED.

forming the third component, are designed as two SC on-chip low-pass filters (LPF) with a cutoff frequency of 1.2 GHz. As this frequency is lower than the fundamental resonance frequency of the resonator, the intrinsic fields of the resonator are not appreciably perturbed. A cut of 20 μm is made in the perimeter of the resonator, to force the dc bias current flow through the HED.

The device, which is top covered by a bare Sapphire substrate, is housed in a gold plated Faraday package made of Oxygen Free High Conductivity Copper. SC Niobium ground planes are dc-magnetron sputtered on the inner covers of the package. RF power is fed using a SubMiniature version A (SMA) launcher, coupled to the feedline. A dc bias is fed through two π-LPFs, screwed to the package, having a cutoff frequency of 1 MHz. IR laser light is guided to the device by a fiber optic cable. A through hole of 1 mm in diameter, is drilled in the Faraday package, and a fiber optic connector affixes the tip of the fiber cable at approximately 9.55 mm above the HED. The resonance frequencies of the Faraday package are given by:

$$f_{n,m} = \frac{c}{2\sqrt{\varepsilon_r}}\sqrt{\left(\frac{N}{a}\right)^2 + \left(\frac{M}{b}\right)^2}, \tag{2.1}$$

where c is the speed of light in vacuum, ε_r is the dielectric constant of Sapphire, N and M are the mode numbers, and a and b are the package dimensions, which equals the Sapphire dimensions. The package has several resonance modes between $2 - 8$ GHz. Fig. 2.2 shows a measurement of the $|s_{11}|$ reflection coefficient, as a function of frequency, of the package filled by two bare sapphires, for various input

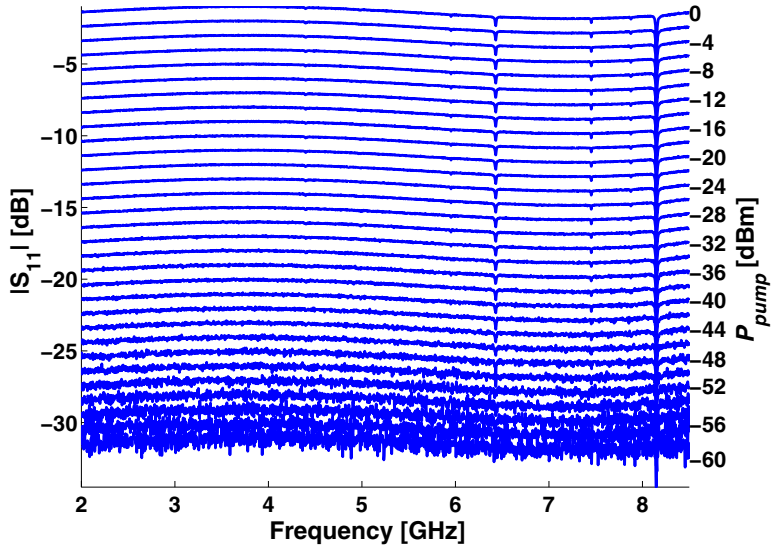

Figure 2.2: Several $|S_{11}|$ measurements, of the Faraday package, as function of frequency and input power. The measurements, shifted vertically for clarity, are obtained for increasing input powers.

power values. All of the resonance modes below 6 GHz are not observed,, and above 6 GHz they have a rather low Q-factor. Usually, when making the same test with a sample loaded into the package, several resonance mode, which are not sensitive to the input power, are observed, and referred to as belonging to the package. Their resonance frequencies can not be correlated one by one to the resonance frequencies measured here. The observation of additional resonance mode suggests, that coupling occurs between these modes and the samples' modes. Probably, there is only a weak coupling between the package and the injected power, at least as long as a sample is not loaded into the package.

2.2 Fabrication Process

The fabrication process starts with a thorough pre-cleaning of the Sapphire wafer in solvents. We have experienced that the commonly employed process of piranha followed by RCA cleaning substantially reduces the NbN adhesion to the Sapphire wafer. In the next step, 200 nm thick gold pads are thermally evaporated through a mechanical mask to form the dc contact pads. The mask partially shadows the evaporation and thus the pads' perimeters are smoothed. Epitaxy, 8 nm (200 nm) thick, NbN film is then deposited at 700 °C using a dc-magnetron sputtering system [25]. Sputtering parameters are summarized in table 2.2 and the process itself is further detailed in [4]. Next, an Aluminium-Nitride (AlN) layer of 7 nm thickness is *in-situ* sputtered in Nitrogen (N_2) atmosphere at a temperature bellow 100 °C. This layer protects the vulnerable NbN layer during the following fabrication processes and restrain degradation [16]. It has also a functional role, as at cryogenic temperatures, it serves as

Table 2.2: Sputtering Parameters

Process parameter	**NbN-E13**	**NbN-E15**	**NbN-E16**	**AlN-All**
Partial flow ratios (Ar,N_2)	(87.5%,12.5%)	$\longrightarrow$	$\longrightarrow$	(0%,100%)
Base temperature	700 °C	$\longrightarrow$	$\longrightarrow$	60 °C
Base pressure [10^{-7} torr]	1.4	0.87	3.6	1.8
Work pressure [10^{-3} torr]	8.7	8.4	6.8	2.9
Discharge current	360mA	$\longrightarrow$	$\longrightarrow$	$\longrightarrow$
Discharge voltage	310V	311V	$\longrightarrow$	292V
Deposition rate	3.6 Å/sec	$\longrightarrow$	$\longrightarrow$	1.1 Å/sec
Thickness (t)	200nm	$\longrightarrow$	8nm	7nm
Target-substrate distance	95mm	$\longrightarrow$	$\longrightarrow$	230mm

a thermal conducting layer, which enhances the cooling of the NbN layer. In the next step, the HED meander stripline is patterned using Electron Beam Lithography (EBL). The deposition of a 80 nm thick Poly-Methyl-Methacrylate (PMMA) 950K layer is followed by EBL with the following parameters: 40kV, 15pA, and 2.1nC/cm, corresponding to acceleration voltage, emission current, and line dose respectively. Afterwards, the AlN layer is directly etched through the PMMA mask using ion milling. The remaining AlN layer serves as a mask for the sequential etching of the NbN layer, using low power Reactive Ion Etching (RIE) in Sulfur Hexafluoride (SF_6) environment [37]. The remaining PMMA is removed by N-Methyl-2-Pyrrolidone (NMP). The last fabrication step is the patterning of the resonator and the LPFs features. This is achieved by using standard photolithography process. The photoresist development process (employing AZ-326 photoresist developer), also wet etches the AlN layer [44], while the remaining layer is again used as a mask for the RIE of the NbN film.

2.A Fabrication Processes

2.A.1 Introduction

The fabrication process described in section 2.2, is the final outcome of a long development process. Along the way various fabrication approaches were tried and failed. This appendix has several purposes. First it describes in details the fabrication process, giving a step by step recipe for producing a working device. Second, it describes various fabrication approaches that failed to succeed. Some of the processes are good as stand alone processes and only failed because they are destroyed by a sequencing process or destroys a previous one. These processes can be used at other designs. Other processes can be used as "don't do" examples.

2.A.2 Step by step fabrication process

The following fabrication procedure is the one used for the fabrication of E13, E15, and E16.

1. If the Sapphire wafer has earlier traces of NbN it should be etched by immersing the sample in HNO3:HF:H2O – 1 : 1 : 4 solution. This is a very dangerous and poisonous acid and adequate precautions should be taken.

2. Thorough pre-cleaning of the Sapphire wafer in solvents - Acetone , Methanol, and Isopropanol. The Sapphire should be cleaned in an ultrasonic bath for at least 5 minutes per solvent and then rinse with De-Ionized (DI) water.

3. Thermal evaporation of ~2000 Å Gold pads, preceded by an evaporation of ~150 Å of Titanium, for adhesion. The Sapphire is covered by an Aluminium (Al) foil, having two opening at the dc pads locations. The foil should not be tightly attached to the Sapphire, to enable partially shadowed deposition.

4. Thorough cleaning in solvents as described in 2.

5. NbN sputtering followed by AlN sputtering according to the parameters in table 2.2.

6. Electron Beam lithography:

   (a) PMMA deposition as described in section 2.A.4.

   (b) EBL exposure as describes in section 2.A.4.

   (c) PMMA development using EHBK:Isopropanol 1 : 3 solution for 60 s, followed by Isopropanol solution for 20 s.

7. Direct etch of the AlN layer through the PMMA mask using ion-milling for 210 s.

8. Direct etch of the NbN through the AlN mask, using RIE.

   (a) The RIE process parameters are:

      i. SF_6 gas flow - 10 sccm.

      ii. Chamber pressure - 10 mtorr.

      iii. RF power - 30 W.

      iv. Room temperature.

   (b) The exact etch rate of the RIE process is not so clear. It seems that a lower etching rate characterizes the beginning of the etching process, probably due to the native Oxygen (O_2) layer. The etching rate can not be calibrated precisely because the RIE machine does not have a glass window. The approximated etch rate is ~3 Å/ s for thick layers and 2 Å/ s for thin layers. Some examples of processes that succeeded are:

i. Etching of 80 Å thick NbN layer. First 25 s were not enough. Additional 15 s finished the job.
ii. Etching of 2000 Å thick NbN layer was performed in 12 min.
iii. Etching of 1000 Å thick NbN layer was performed in 6 min.

(c) AlN has a strong durability to this process. Etching of a 400 Å AlN layer was not finished, even after more than 10 min.

9. Sections 7 and 8 can be replaced by direct etch process using Electron Cyclotron Resonance (ECR) etching in Chlorine (Cl_2) and Hydrogen (H_2) environment [47], [35] (note that the suggested process using $CH_4/H_2/Ar$ failed to succeed in our system. We believe that this process works more due to the Argon (Ar), and less due to the selectivity of the CH_4/H_2). This process etches both AlN and NbN layers. It is important to pre-bake the PMMA in 110 °C oven for 30 min, prior to etching. This etching process usually produces better results than ion-milling followed by RIE process.

   (a) The process parameters are:
      i. Cl_2 gas flow - 10 sccm, H_2 gas flow - 15 sccm.
      ii. Chamber pressure - 2 mtorr.
      iii. RF1 power - 75 W, RF2 power - 250 W.
      iv. Upper magnet - 180 W, Lower magnet - 0 W.
      v. Room temperature.

   (b) Etch rates are 600 Å/30 s and 500 Å/50 s for the NbN and AlN layers, respectively.

10. PMMA removal. Soak sample in NMP on a 140 °C hot plate. Do not pre-hit the NMP before soaking the sample. An additional overnight soak is preferable.

11. Patterning of the resonator and the LPFs features using photolithography.

   (a) Thorough cleaning of the Sapphire wafer in solvents, as describes in 2.
   (b) Dry sample on a 110 °C hot plate for 10 min.
   (c) Deposition of 4533 photoresist, by spinning at 4000 r/min for 60 s.
   (d) Baking in 90 °C oven for 10 min.
   (e) Exposure of sample - exact time is microscope dependent.
   (f) Baking in 90 °C oven for 3 min.

12. Development using AZ-326 photoresist developer for 60−80 s. This development process also wet etched the AlN layer [44].

   (a) Two calibration of the etching rate of AlN by AZ-326 were made. The first measured etching rate is 1000 Å/77 s. The second measured etching rate is 400 − 500 Å/25 s.

13. Direct etch of the NbN layer using RIE.

14. Thorough cleaning of the Sapphire wafer in solvents, as describes in 2.

2.A.3 Examples of unsuccessful fabrication processes

The following fabrication procedures were tried and failed:

EBL liftoff using various metals As described in section 2.A.4, sputtered Al, thermal evaporated Al and thermal evaporated Chromium (Cr) were used as a mask for a sequential etching processes. Sputtered Al failed due to its high quality crystallographic properties. It was lifted-off as a foil and was not removed completely. Thermal evaporated Al produced nice liftoff results, but when it was etched in the sequential photolithography process. Cr produced the best liftoff results, but we failed in removing it later, after the etching process, for unknown reason.

Oxidizing processes The NbN is vulnerable to oxidizing processes that produces Pentoxide Niobium (Nb_2O_3) and destroy its superconductive properties. During the development process we tried some processes and solutions that had been found to act as superconductivity destroyers:

1. The commercially available Al and Cr etching solutions.

2. O_2 plasma that was used after PMMA development and before metal deposition to remove PMMA monolayer.

3. Drying the sample on a very hot plate, when exposed to air.

This experience led us to the insight that the NbN should be well protected from air and oxidizing solutions. This led to the addition AlN layer, which is deposited *in-situ* above the NbN layer.

Natural NbN oxidation layer In one of the development processes we tried to produce a device built from two layers of NbN, one on top of the other. Natural oxidation layer, about 30 Å thick, substantially destroyed the ohmic contact between the layers and caused a failure of the device. This problem also occurs when evaporating the gold pads on top of the NbN instead underneath it.

Using photoresist as a mask for Ion-milling etching processes This process is a big failure, and should not be used. The photoresist is being heated very fast and burned. Burned photoresist is almost impossible to be removed.

Piranha and RCA cleaning Sapphire cleaning by using Piranha and RCA cleaning was found to substantially reduce the adhesion of the NbN to the Sapphire wafer, and therefore this process is not recommended. If remaining metals must be etched away, solvent cleaning should be made afterwards.

2.A.4 Electron Beam lithography (EBL)

Working methods

During the fabrication process development two methods of controlling the microscope were used:

1. Using NPGS software and the PC attached to the microscope.
2. Direct control using a Data-Translation digital to analog board (DTx).

Using NPGS has a few advantages:

1. A drawing software is used to design the written pattern. There are no limitation on its shape and geometry.
2. The parameter file that characterizes the EBL (in terms of exposure dose (ED), etc.) is clear and well explained.
3. The NPGS controls the fast beam blanker.

The NPGS has also a few limitations:

1. The drawing program is cumbersome and inflexible. It also has some unfixed bugs that limits the ability to plan complex writing sequences.
2. Designing a pattern, that includes repetitive structures, can be an exhausting task.
3. The writing frequency is limited to 100 kHz.

Using the DTx boards has the following advantages:

1. The writing frequency is exceeded to 500 kHz.
2. Maximum flexibility in planning complex writing sequences at various ED.
3. Easy design of patterns having repetitive structures.

And disadvantages:

1. The geometry shape is currently limited.
2. There is no control on the beam blanker.
3. The design is more abstractive, good only for experienced writers.

Calibration of the DTx to the microscope The voltage limits of the microscope's screen are $\pm 10\,\mathrm{V}$, that is, the upper right corner and lower left corner coordinates are $(10\,\mathrm{V}, 10\,\mathrm{V})$ and $(-10\,\mathrm{V}, -10\,\mathrm{V})$, respectively. The change in the applied voltage, that is needed to create a $1\,\mu$m movement at 800 amplification, is $0.157\,\mathrm{V}/\,\mu\mathrm{m}$. For other amplification the voltage needed is calculated using $V = 0.157/800*$(current magnitude) [V]. These calibration holds for both X and Y axes.

Writing methods

During the fabrication process development, two approaches of EBL have been used:

1. EBL patterning for liftoff
2. EBL patterning for direct etching.

As far as the EBL process concerns these approaches differ in the preparation of the PMMA layers and in different ED during the EBL writing itself. The following expands the subject. Additional practical information is found in [43].

PMMA layer deposition for liftoff process

Introduction The rule of thumb for the width of the PMMA layer, used in liftoff process, demands that it would be at least three times the width of the layer that would be deposited on it. Therefore, usually the PMMA layer should be relatively thick. The thickness of the PMMA is determined by the PMMA dilution level in Azinole and the spinning speed of the spinner during the deposition itself. Usually, the PMMA dilution level ranges between $2-6\%$ and the spinning speed is determined using the graphs found in [1].

We use two variations of the PMMA polymer, PMMA-950 and PMMA-495, which differ in their sensitivity to electrons. The first has low sensitivity and therefore suitable for high resolution EBL. The second has higher sensitivity and therefore suitable for moderate resolution EBL. The PMMA layer suitable for liftoff processes made of both these polymers, a bottom thick layer of PMMA-495 and a top thinner layer of PMMA-950 above it. Ebeam exposure, and after development of this double layer, a small hole is opened in the top layer and a larger one in the bottom, creating an upside down funnel like hole shape under cut, which is best for liftoff processes.

PMMA layer deposition recipe for lift off process The following recipe produces a PMMA layer with a total thickness of $1500-1700\,\text{Å}$, and has a ratio of $1:2$ between PMMA 950 and PMMA 495 layers. The PMMA layer is deposited on a NbN layer having a thickness of ~$100\,\text{Å}$. This recipe was used for producing a meander shaped having lines width and gap of ~$100\,\text{Å}$ and ~$300\,\text{Å}$, respectively. In practice, due to proximity effect, a ratio of $1:1$ between line width and gap is measured after development.

1. Thorough pre-cleaning as described in subsection 2.A.2#2 . If wafer is sensitive to ultrasonic bath use hot plate instead.
2. Dry sample on a 110 °C hot plate for 10 min.
3. Deposit PMMA 495 3% at a spinning speed of 4500 r/min for 45 s.
4. Dry sample on a 180 °C hot plate for 6 min.
5. Deposit PMMA 950 2% at a spinning speed of 4500 r/min for 45 s.
6. Dry sample on a 180 °C hot plate for 6 min.

PMMA layer deposition for a direct etching process

Introduction The rule of thumb for direct etching process says that, the thinner the PMMA layer the higher the writing resolution. But, on the other hand, the layer should be sufficiently thick to stand the etching process that follows the EBL. The PMMA polymer has low durability to plasma etching, that is, usually the rate at which the PMMA is etched is much higher than the rate at which the base layer is etched. Therefore, in order to achieve high resolution, in a thick base layer, we need a two-layers mask, in which a thin PMMA is deposited on top an even thinner layer that has a good selectivity for the specific sequent plasma etching process. The ratio between the width of that layer and the PMMA should be at least 1 : 4. The AlN layer is used as that layer in our design.

PMMA layer recipe for direct etching processes The following recipe produces a PMMA layer with a total thickness of ~800 Å. The PMMA layer is deposited on an AlN layer having a thickness of ~70 Å, which is deposited on top of a NbN layer having a thickness of ~100 Å. This recipe was used for meander shaped EBL having lines width and gap of ~100 Å and ~300 Å, respectively. In practice, due to proximity effect, a ratio of 1 : 1 between line width and gap is measured, after development.

1. Thorough precleaning, as described in 2.A.4.
2. Dry sample on a 110 °C hot plate for 10 min.
3. Deposit PMMA 950 2% at a spinning speed of 3250 r/min for 45 s.
4. Dry sample on a 180 °C hot plate for 6 min.

The following recipe produces a PMMA layer with a total thickness of ~1750 Å. The PMMA layer is deposited on a AlN layer having a thickness of ~70 Å, which is deposited on top of a NbN layer having a thickness of ~1000 Å. This recipe was used for EBL of Fresnel zone plate (Fig. A.3), whose narrowest width is ~500 Å, and for a matrix of dots, whose smallest dimension is ~200 Å.

1. Thorough precleaning, as described in 2.A.4.

2. Dry sample on a 110 °C hot plate for 10 min.

3. Deposit of PMMA 950 3% at a spinning speed of 1500 r/min for 45 s.

4. Dry sample on a 180 °C hot plate for 6 min.

EBL exposure

Exposure consideration There are various consideration that should be taken into account when planning the right exposure dose (ED):

1. **PMMA layer width** - The more thicker the PMMA layer is the more ED is needed, but the ratio between the two is not 1 : 1, and the ED increases in a more moderate way.

2. **Proximity effect** - This effect is caused by unabsorbed electrons, that reflects off the substrate at various angles, and then are absorbed by the PMMA. As so, the line width that is achieved in practice can be much larger that the one designed. This effect is significant for lines narrower than 1 μm. For example, lines narrower than 200 Å are widened by as much as 140%. When planning the ED, one must remember, that each points absorbs the direct impinging electrons and in addition, electrons that are reflected from its surrounding area, which are aimed at other points. As so denser shapes should have a lower ED. The following summarizes some of the problems that this effect causes, and various ways of dealing with them.

   (a) The ED needed for surfaces is much lower that the one needed for stand alone lines and dots. In general when ever the density of the shape is changed, a new ED calibration is needed.

   (b) Line broadening - one should draw narrower lines than needed, as they would be widened. Calibration is needed whenever the line width changes significantly.

   (c) Under-dose exposure of lines at the peripherals of the shape - Even after a thorough calibration, lines at the peripherals of a shape are less exposed than lines in the center of the shape. There are two ways to cope with this problem:

      i. Explicit increment of the ED at the peripherals.

      ii. Add an additional structures whose only purpose is to increase the ED at the peripherals. These structures are usually referred to as sacrificing structures. Such a structure can also aid in balancing the development process, that for some geometries may be more rough at the peripherals than in the center of the shape. Clearly such a structure should not interfere with the actual design.

Table 2.3: EBL Liftoff Parameters - I

Design parameters		**NPGS parameters**	
Geometry	Meander	**Magnification**	800
Line Width [nm]	100	**Dot space** [Å]	206
Line Gap [nm]	500	**Line Space** [Å]	326.2
PMMA width [Å]	1500	**Beam current** [**pA**]	25
		Line Dose [**n** C/ cm]	2.9-3.1

3. **Acceleration voltage** - There is a linear, 1 : 1, correlation between the electron beam acceleration voltage and the ED, that is, when doubling the acceleration voltage a doubling in the ED is needed.

4. **Exposure current** - The exposure current determines the diameter of the electron beam spot. It should not exceed $10 - 25$pA for high resolution EBL.

5. **Amplification** - Usually a $800-3000$ amplification is needed for high resolution writing. In general its is not recommended to write at amplifications close to 1000 (or 100, 10k) as in this amplification a mechanical change of lenses occurs. The microscope magnification determines the following:

   (a) The electron beam diameter.

   (b) The boundaries of the effective writing area.

   (c) Writing resolution - together with the voltage resolution of the DTx board, the magnification determines the smallest possible deviation of the electron beam

Exposure dose recipes The ED can be calculated as ED for surface ([μ C/ cm^2]) or ED for line ([n C/ cm]). When area ED is used, the ED for each line is calculated according to the density of lines per centimeter, which is calculated using to the space-between-lines design parameter. If line ED is used, the over all surface ED is set according to the number of lines in the design. The bottom line is, that calibration using line ED is more flexible, and is required when writing stand alone lines, that have variable gaps between them. Keep in mind that, the line ED calibration itself is sensitive to the gaps between the line, and to the microscope amplification. As so, if the shape does not include patterns smaller than 1 μm, then surface ED calibration is preferred

Following are a few tables that summarizes various parameters used for successful liftoff EBL processes:

Following are a few tables that summarizes various parameters used for successful direct etching EBL process:

Table 2.4: EBL Liftoff Parameters-II

Design parameters		**NPGS parameters**	
Geometry	Pads	**Magnification**	600
Line Width [nm]	100	**Dot space** [**Å**]	206
Line Gap [nm]	500	**Line Space** [**Å**]	343.3
PMMA width [**Å**]	1500	**Beam current** [**pA**]	50
		Line Dose [**n** C/ cm]	2.9-3.1

Table 2.5: EBL Direct-Write Parameters - I

Design parameters		**NPGS parameters**	
Geometry	Meander	**Magnification**	800
Line Width [nm]	100	**Dot space** [**Å**]	206
Line Gap [nm]	350	**Line Space** [**Å**]	257.5
PMMA width [**Å**]	800	**Beam current** [**pA**]	25
		Line Dose [**n** C/ cm]	2.1

Table 2.6: EBL Direct-Write Parameters-II

Design parameters		**NPGS parameters**	
Geometry	Meander	**Magnification**	800
Line Width [nm]	100	**Dot space** [**Å**]	206
Line Gap [nm]	700	**Line Space** [**Å**]	257.5
PMMA width [**Å**]	800	**Beam current** [**pA**]	25
		Line Dose [**n** C/ cm]	2.7

Table 2.7: EBL Direct-Write Parameters-III

Design parameters		**NPGS parameters**	
Geometry	Meander	**Magnification**	3000
Line Width [nm]	100	**Dot space** [**Å**]	201.4
Line Gap [nm]	450	**Line Space** [**Å**]	256.3
PMMA width [**Å**]	800	**Beam current** [**pA**]	15
		Line Dose [**n** C/ cm]	1.9-2.1

Table 2.8: EBL Direct-Write Parameters-IV

Design parameters		**NPGS parameters**	
Geometry	Meander	**Magnification**	3000
Line Width [nm]	100	**Dot space**[Å]	201.4
Line Gap [nm]	900	**Line Space** [Å]	256.3
PMMA width [Å]	800	**Beam current** [**pA**]	15
		Line Dose [**n**C/cm]	2.5

Table 2.9: EBL Direct-Write Parameters-V

Design parameters		**NPGS parameters**	
Geometry	Pads	**Magnification**	1500
Line Width [nm]	100	**Dot space**[Å]	210.6
Line Gap [nm]	900	**Line Space** [Å]	256.3
PMMA width [Å]	800	**Beam current** [**pA**]	15
		Line Dose [**n**C/cm]	0.6

Metal deposition for liftoff

Expected problems The main problem with liftoff process is to achieve a complete liftoff of all the unneeded metal layer. Especially at small geometries, problem of remaining metal occasionally happens. There are two probable causes for problems in liftoff processes. First, if the ratio between the evaporated metal and the PMMA thickness is not large enough, metal might cover the sidewalls of the opening in the PMMA and prevent successful liftoff. The second arise from a bad choice of evaporated metal layer. Two observation are possible for these cases. First, metal is left at places where is should not be, and second, lifted metal drags and removes metal from places where it should have stayed. In order to avoid these problems the following should be kept:

1. **Low quality crystallographic metals** - The deposition process should produce a low quality crystallographic metals. Such a metal tends to break into tiny shard during liftoff, which greatly helps the process to succeed. High quality crystallographic metals tends to be lifted as a continuous foil, a character that causes metal liftoff difficult.

2. **Large sample-target distance** - Prior to deposition, the distance between the target and the sample should be set to maximum, so the angle of incidence would be as small as possible, and side walls won't be covered.

Crystallographic Properties of Metals

1. **Sputtered Aluminum** - This Al has high crystallographic quality and therefore is not recommended.

2. **Thermal evaporated Aluminum** - This Al has low crystallographic quality and therefore is recommended. Note that Al is being etched by standard photoresist developers [54], and therefore should be carefully adjust to sequential processes.

3. **Thermal evaporated Chromium** - This Cr breaks into tiny shard during liftoff, and therefore is excellent for liftoff. Nevertheless, frequently, for unknown reason, a sequent process of Cr etch failed to succeed after liftoff.

Liftoff performing

The liftoff process itself is not a trivial task, and should be taken with an extra care. The PMMA layer can not be easily removed [2], especially as violent tools, such as ultrasonic bath, are usually avoided, to prevent damages to sample. The sample should be kept wet at all times, until a complete liftoff is achieved. In general, PMMA is dissolved in Acetone and NMP, and has high etching rate at O_2 plasma (70 nm/ s). The following describes a successful liftoff process:

1. Soak sample in NMP on a 140 °C hot plate. Do not pre-hit the NMP before soaking the sample. An additional overnight soak is preferable.

2. Clean sample using Acetone gun.

3. Repeat $1, 2$ until a complete liftoff is achieved.

4. Remove PMMA monolayer using 10 s O_2 plasma etching.

Example pictures

Fig. 2.3 shows a few optical microscope pictures of meander-shaped photon detectors. Panels $(a) - (c)$ show meanders, that were made using EBL liftoff process. Panel (a) shows an example for the importance of redundancy in every step of the fabrication process in general, and in particular in the EBL process. Six different meander shapes were written, each with a slightly different ED. Indeed some were more successful, as the lower right one, which was also chosen, and some were not, such as the one on the lower left, which can hardly be seen. Each meander has a $100 \times 100\,\mu\text{m}^2$ meander shape, and two contact pads. The contact lines were deposited in a sequential photolithography process, which also employed liftoff technique. The difference in color between the shapes is caused by the Cr, which had not been removed properly from all shapes. Panel (b) shows a closer look on the connection of the meander to the contact pad. One can clearly see the meander's sections, each section has a written dimension of a $0.1 \times 100\,\mu\text{m}^2$, and the gap between the sections is $400\,\mu\text{m}$ (written dimensions). The nice connection between the contact pad and the meander line is indicated. In addition four sacrificing lines were designed, according to the discussion in section item 2c. Panel (c) shows another example of the sacrificing

lines. In this example the lines protects the corner of the meander, which is the most vulnerable point of the shape. Panel (d) shows a meander, that was made using EBL direct etching process. In this precess the EBL writes a complementary shape of the meander. The written lines (black) are etched and function as the gaps between the meander sections. This design is simpler than the one made for the liftoff process as it does not include sacrificing lines.

2.B Sputtering Machine Characteristics

The sputtering process of SC NbN depends of many parameters, where the outcome of the process can differ substantially for different combinations of choice. A detailed explanation of the process is found in [4]. Here we give a short complementary description, regarding the sputtering of the AlN.

Like NbN, also AlN sputtering process has as many parameters [17], [40], [39]. Fortunately, the only quality we demand from the AlN we deposit is that it would behave as an insulator at low temperature. This is easily achieved by sputtering the AlN in a pure N_2 environment, with the parameters detailed at table 2.2. Fig. 2.4 shows the AlN sputtering-machine characteristics for various combinations of N_2 and Ar gas atmospheres. Panels (a) and (b) plot the deposition rate and discharge voltage of the AlN as a function of the applied current, respectively.

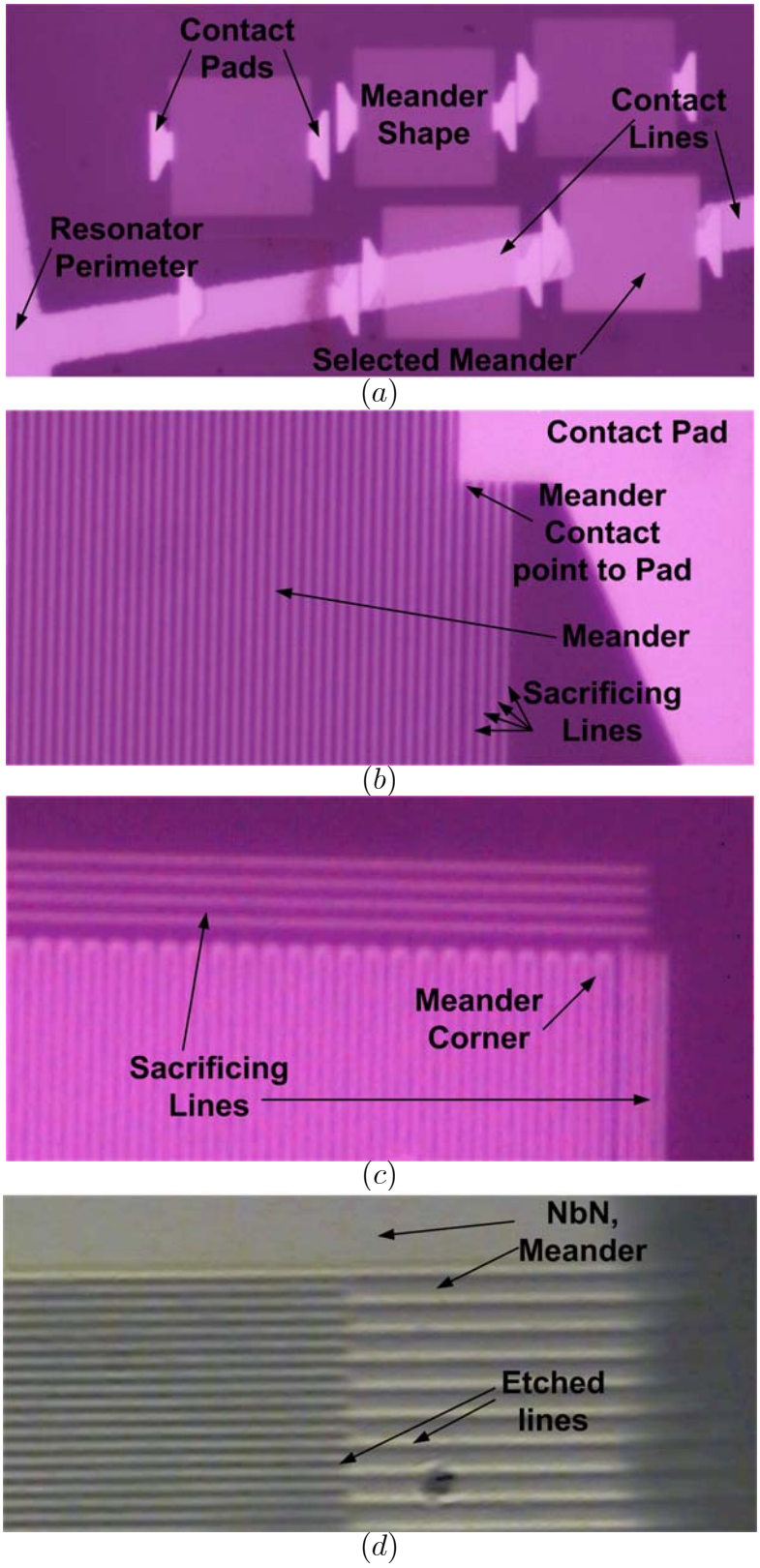

Figure 2.3: Optical pictures of meander shapes photon detectors, made using EBL and liftoff process $(a - c)$. (a) shows six different $100 \times 100\,\mu m^2$ meander shapes, made for redundancy. (b) shows a closer look of the connection of the meander shape to the contact pad. (c) shows an example of the sacrificing lines. (d) shows a meander made using EBL direct-write process

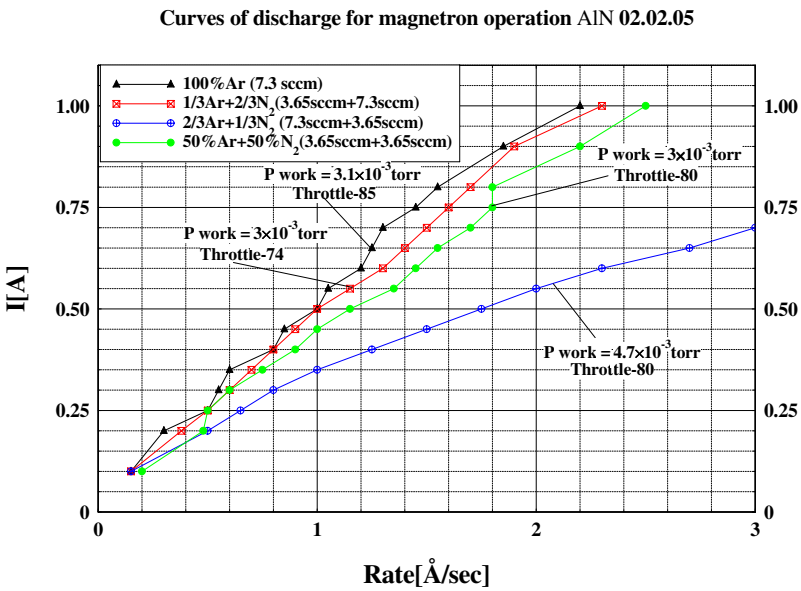

(a)

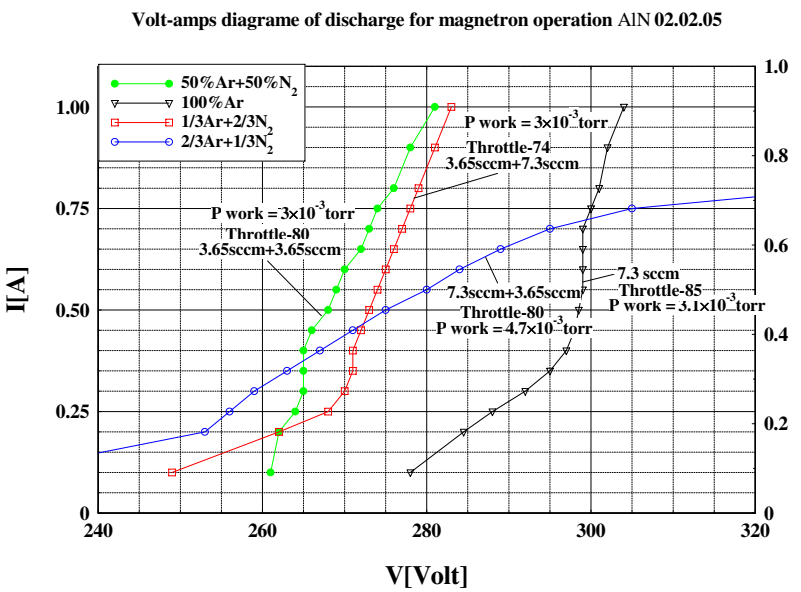

(b)

Figure 2.4: AlN sputtering-machine characteristics for various combinations of N_2/Ar gas atmospheres. (a) Deposition rate and (b) discharge voltage as a function of the applied current.

Chapter 3

Stationary Behavior under External Constraints

3.1 Introduction

The aim of the first few experiments is to test the response of the device to slowly varying external constrains such as dc voltage, current and IR illumination. This chapter begins by showing the HED response to applied dc voltage and current, and the resulting effect on the resonance frequencies. These results are followed by a comparison with a theoretical model. Afterwards, the effect of CW IR light on the resonance frequency is described.

All measurements presented in this chapter are performed of E16 device, and are carried out in a fully immersed sample in liquid helium (4.2 K). The experimental setup, used for stationary reflection measurements, is schematically depicted in Fig. 3.1. The samples's RF feedline is connected to a vector network analyzer (NA) using a semi-rigid coax cable. The dc feedlines are connected to a dc source-measure unit using 4-probe wiring. The laser source has a wavelength of 1550 nm.

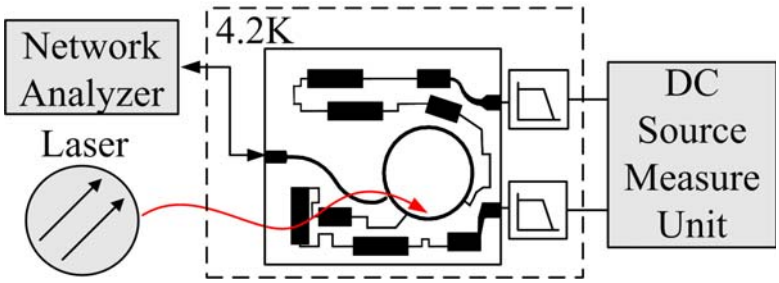

Figure 3.1: Setup used for reflection measurements.

3.2 DC I-V Measurements

The basic I-V characteristics of the HED meander stripline, shown in Fig 3.2, exhibit a highly complex hysteretic behavior. Panel 3.2(a) plots nine current measurements, obtained while increasing the applied voltage (blue), one on top of the other, where each measurement starts at zero voltage and ends at a different maximum voltage, slightly above the voltages V_{Cn}, depicted in the figure. The corresponding nine current measurements, obtained while decreasing the applied voltage are also plotted (red). The magenta and black curves correspond to similar measurements, taken while the HED is being illuminated. The measurements for low applied voltages and currents are enlarged in the insets of Fig 3.2(a) and 3.2(b) respectively, where the finite resistance is due to the contacts.

At panel 3.2(a), nine, clearly distinguished, abrupt jumps in the measured current are noticed. The number of current jumps corresponds to the number of stripline sections that compose the meander shape of the HED. Each jump is the result of a large increase in the HED resistance due to a transition of one section from the SC state to the normal conducting (NC) one. This behavior is typical for a SC microbridge and is caused by the formation of a hotspot in the bridge area [29]. Each critical voltage V_{Cn}, varies, in general, between different scans, indicating thus, the stochastic nature of the transitions between bistable states. The fluctuation ΔV_{Cn} in V_{Cn}, between different scans, characterizes the lifetime of the pre-jump metastable states of the system. The increase in ΔV_{Cn} at high voltages indicates a decrease in the lifetime of metastable states because of larger temperature fluctuations. The combined results of the increasing and decreasing applied voltage measurements show that large hysteresis is present at all current jumps except for the first one. This observation indicates, that only one section at a time can be biased into subcritical conditions. Furthermore, only the section responsible for the first jump, at V_{C1}, doesn't suffer form hysteresis and thus can repetitively respond to radiation. Probably, the cause for this discretization of the critical current is the non-uniformity in the meander shape of the HED [29], [60]. Our finding clearly shows that the non-uniformity may substantially reduces the effective area of the HED, up to a fraction of one ninth of its printed area.

The same measurements are repeated while constantly illuminating the HED with approximately 27 nW IR laser. In these measurements the current jumps occur at lower applied voltages, $V'_{Cn} < V_{Cn}$. In addition, ΔV_{Cn} are substantially widened. Although the decrease in the critical voltage values can be explained by local heating due to the IR illumination, the increase in ΔV_{Cn}, especially at low voltages, imply that photon absorptions cause discrete events that considerably increase the instability of the HED.

Panel 3.2(b) shows voltage measurements, obtained while increasing the applied current, with (magenta) and without (blue) IR illumination, and while decreasing the applied current, with (black) and without (red) IR illumination. Two abrupt voltage jumps occur at distinguishable critical currents of $I_{C1} \cong 4.2\,\mu$A and $I_{C2} \cong 9.8\,\mu$A. IR illumination has a negligible measured effect on I_{C1} and a strong effect on I_{C2} values. All voltage jumps suffer from hysteresis and therefore current bias is an unsuitable method for repetitive radiation detection.

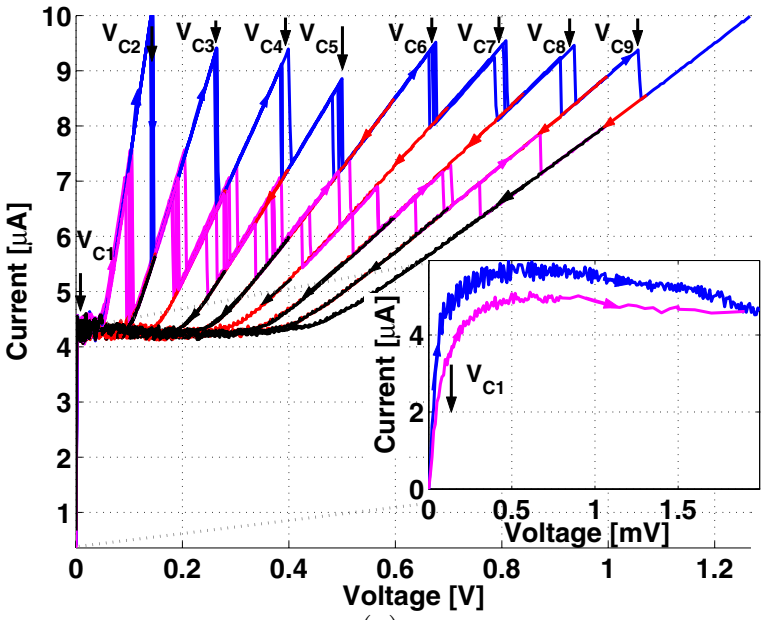

(a)

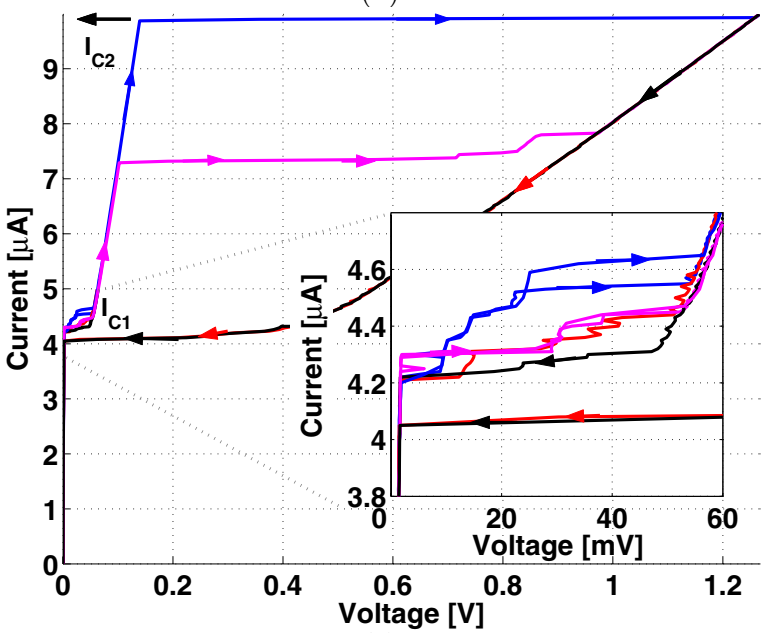

(b)

Figure 3.2: Basic I-V characteristic of the HED meander stripline. (*a*) Current vs. voltage and (*b*) voltage vs. current measurements. The magenta (blue) curves show an increasing applied voltage and current measurement, with (without) laser illumination. The black (red) curves show a decreasing applied voltage and current measurement, with (without) laser illumination. The insets of (a) and (b) magnify the results for small applied voltages and currents respectively.

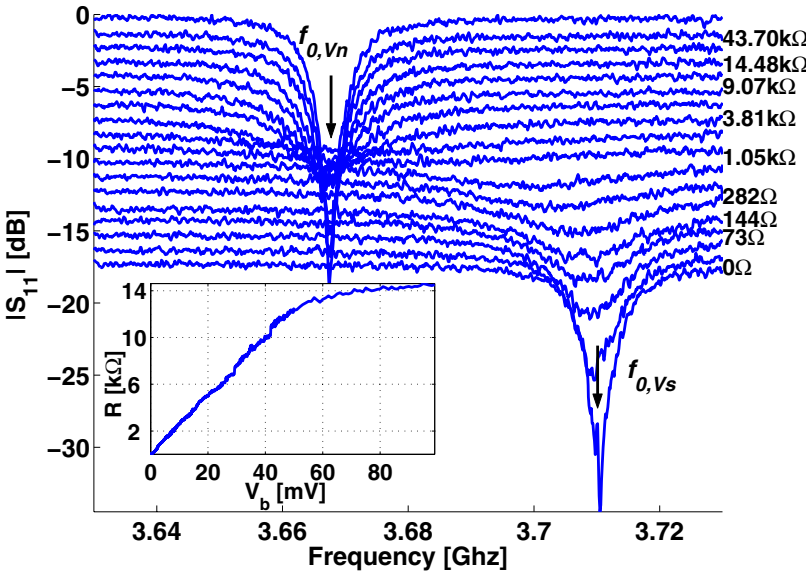

Figure 3.3: Several $|S_{11}|$ measurements of the second resonance mode, as a function of frequency, for various HED resistance values. The measurements are obtained while applying variable voltage and the HED resistance is measured using 4-probe technique. Plots are shifted vertically for clarity. The inset shows the resistance vs. voltage characteristics of the HED.

3.3 DC I-V Effect on the Resonance Lineshape

Fig. 3.3 shows several $|S_{11}|$ measurements as a function of frequency, in the vicinity of the second resonance mode, for various HED resistance values. For clarity, the resonance curves are vertically shifted upwards, for increasing resistance values. The measurements are obtained while applying variable voltage V_b, and the resistance is measured simultaneously with the $|S_{11}|$ data using standard 4-probe technique. The RF input power is set to -64.7dBm, where the resonator is in the linear region [6]. The inset of Fig. 3.3 plots the measured HED resistance as a function of V_b.

The dependence of the resonance characteristics on the HED resistance R_{HED}, can be described as followed. At zero applied voltage the resonance frequency is $f_{0,Vs} \cong 3.71\,\text{GHz}$. At very low voltages, as the HED is biased far below critical conditions, its resistance is negligible and its influence on the resonance curve as well. As the resistance increases, the resonance frequency slightly red shifts, and more important, the Q-factor is significantly reduced due to dissipation in the HED. This behavior continues up to a point, at $R_{\text{HED}} \cong 1k\Omega$, where the resonance curve can be hardly detected. When increasing the resistance beyond that point the trend of the Q-factor changes, the dissipation decreases, and the resonance curve reemerges at a new resonance frequency, $f_{0,Vn} \cong 3.665\,\text{GHz}$, red shifted by approximately 45 MHz relative to its original value. The new resonance Q-factor has a value similar to the original one. When further increasing the resistance, the trend of the Q-factor continues but no additional resonance shift occurs. The behavior of the Q-factor suggests that as R_{HED} increases, the RF current amplitude of the resonance mode in the HED is

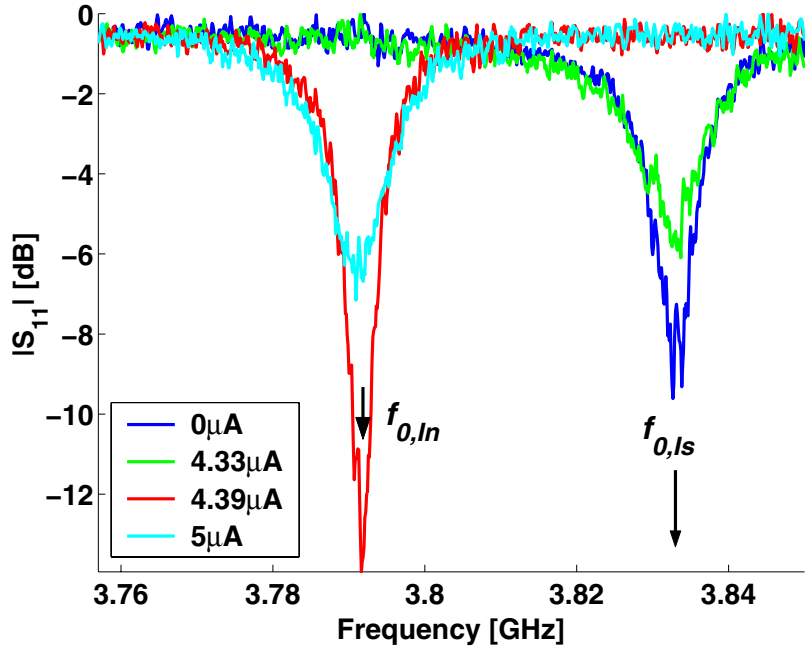

Figure 3.4: Several $|S_{11}|$ measurements of the second resonance mode, as a function of frequency. The measurements are obtained while applying variable current.

reduced, due to current redistribution, and thus the total power dissipation decreases.

Similar behavior, with one major exception, can be observed under applied current, as shown in Fig 3.4. The blue, green, red, and cyan curves are taken with subcritical $0\,\mu$A, $4.33\,\mu\text{A} < I_{C1}$, and over critical $4.39\,\mu$A, $5\,\mu\text{A} > I_{C1}$ applied currents, respectively, where I_{C1} is the current at which a first jump in the measured voltage occurs. There are two well defined resonance frequencies, $f_{0,Is} = 3.83\,\text{GHz}$, and $f_{0,In} = 3.79\,\text{GHz}$, which corresponds to applied currents below, and above I_{C1} respectively. $f_{0,Is}$, and $f_{0,In}$ slightly differ from $f_{0,Vs}$, and $f_{0,Vn}$ as the two measurements were taken at different thermal cooldown cycles. Low Q-factor curves are absent from this measurement because under applied current, the HED can not be biased into intermediate resistance values. At bias currents below I_{C1}, the HED has low resistance, which only slightly increases as the current approaches I_{C1}. As a result, no resonance shift occurs, and only the Q-factor slightly reduces as the current increases. This behavior changes abruptly once the HED resistance crosses a rather low, critical value, R_C. A self-sustained hotspot is generated [29], quickly expends, and the HED becomes resistive. I_{C1} is the bias current at which $R_{\text{HED}} = R_C$ is obtained. This thermal runaway causes an abrupt red shift of $\Delta f_0 \cong 40\,\text{MHz}$ in the resonance frequency. Further increase of the bias current beyond I_{C1} increases the power dissipation and heat generation in the HED. This increases the local temperature and dissipation near the HED, and thus causes Q-factor reduction.

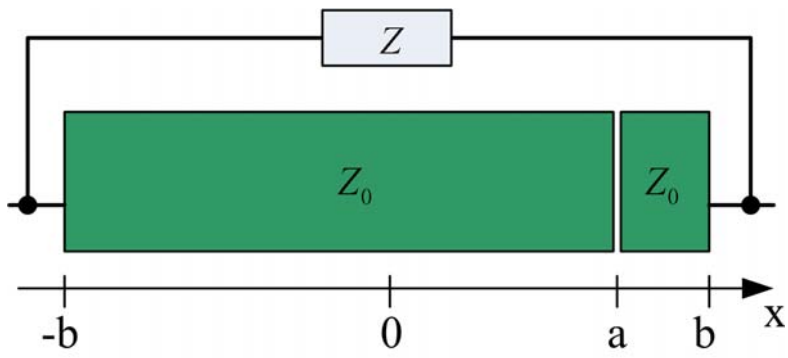

Figure 3.5: Resonator transmission line model.

3.4 Resonance Frequency Shift Modeling

To account for our results we calculate the resonance characteristics of our device, as a function of HED resistance.

As shown in Fig. 3.5, the ring resonator is modeled as a straight transmission line, extending in the $\pm x$ directions. The HED is represented by a lumped discontinuity, $Z = R + jwL$, connecting $x = \pm b$ points together, where R is the resistance, ω is the angular frequency, and L is the total inductance of the meander shape of the HED. The transmission line has a cut at point $x = a$. The couplings to the RF and dc feedlines are neglected.

3.4.1 Field solution

The voltage along the resonator's transmission line is given by a standing waves expression of the form [22]

$$V(x) = \begin{cases} A\cos(\beta x) + B\sin(\beta x) & -b < x < a \\ C\cos\beta(x-a) + D\sin\beta(x-a) & a < x < b \end{cases}, \tag{3.1}$$

where $\beta = 2\pi f\sqrt{\epsilon_r}/c$ is the propagation constant along the transmission line, f is the frequency, ϵ_r is the relative dielectric constant, and c is the speed of light in vacuum. The current is given by $I(x) = (i/\beta Z_0)\, dV/dx$, thus,

$$I(x) = \begin{cases} \frac{i}{Z_0}(B\cos x\beta - A\sin x\beta) & \text{if} \quad -b < x < a \\ \frac{i}{Z_0}(C\sin\beta(a-x) + D\cos\beta(a-x)) & \text{if} \quad a < x < b \end{cases}, \tag{3.2}$$

where Z_0 is the characteristic impedance of the line. By applying the following boundary conditions: (1) $I(a_-) = I(a_+) = 0$, (2) $I(-b) = I(b)$, and (3) $V(b) - V(-b) = I(b)\,Z$, we easily derive a boundary condition equation,

$$\begin{gathered} \cos[\beta(b-a)](\tan a\beta\cos b\beta + \sin b\beta) - \sin[\beta(a-b)]\cos(\beta b) + \\ \sin[\beta(a-b)]\tan a\beta\sin(\beta b) = \\ \sin[\beta(a-b)](\tan a\beta\cos b\beta + \sin b\beta) * \xi, \end{gathered} \tag{3.3}$$

where ξ is a constant defined by $\xi \equiv iZ/Z_0$. The solution of the boundary equation yields,

$$\beta = \beta^{'} + i\beta^{''}, \tag{3.4}$$

where β is the complex propagation constant of the resonator, where, β' is the real propagation constant and $\beta^{''}$ is correlated to the loss factor according to,

$$\gamma_2 = \frac{c\beta^{''}}{\sqrt{\epsilon}} = 2\pi f^{''}. \tag{3.5}$$

3.4.2 Model stationary parameters.

The following stationary parameters characterizes the behavior of the model:

1. Ring resonator characteristic impedance Z_0,
2. HED resistance at the SC state,
3. HED inductance at the SC state.

The model numerical calculations are done with a normalized impedance $\xi \equiv iZ/Z_0$, so Z_0 only affects the fitting of the numerical data to measured data. For the SC state $\omega L \gg R$, The HED resistance is negligible and as so considered zero. Z thus, is governed by its inductive part, $Z = iwL$, and $\xi = -wL/Z_0 \in \mathbb{R}$. The HED inductance at the SC state, L^{SC}, is a very important parameter, that greatly effects the device behavior. Fig. 3.6(a) plots the resonance frequency of the second resonance mode, as a function of the normalized HED resistance, for various initial values of L^{SC}. One observes, that the larger L^{SC} is, the larger the initial deviation of the resonance frequency, and the smaller the remaining possible shift in the resonance frequency, due to a change in the HED's resistance. In addition, as seen in Fig. 3.6(b), for smaller L^{SC}, the smaller the resistance range, in which high losses occur in the resonator. The strait forward conclusion is that, L^{SC} should be kept as low as possible, but in order to do so the area of the HED should be reduced, or its thickness should be increased. Both requirements are problematic, as far as photon detection is considered, so the actual design is a compromise between the detector area and its thickness and inductance.

3.4.3 Model Results

A phase transition of Z from SC to NC state simultaneously causes changes in its resistive, $\Delta R > 0$, and inductive, $\Delta L > 0$, parts. Both changes contribute to a resonance shift in the same direction. For a very thin SC films $\Delta R \gg \Delta L$ resulting in $\Delta Z \cong \Delta R$. Three fitting parameters are used in the model. Best fit results are obtained for $R = 0\Omega$, $Z_0 = 55\Omega$, and $\omega L = 14.5Z_0$, which leads to $L = 37.3$nH for the second resonance mode. In the SC state $R \ll Z_0$, and thus negligible. The characteristic impedance Z_0 value is in a very good agreement with the designed value

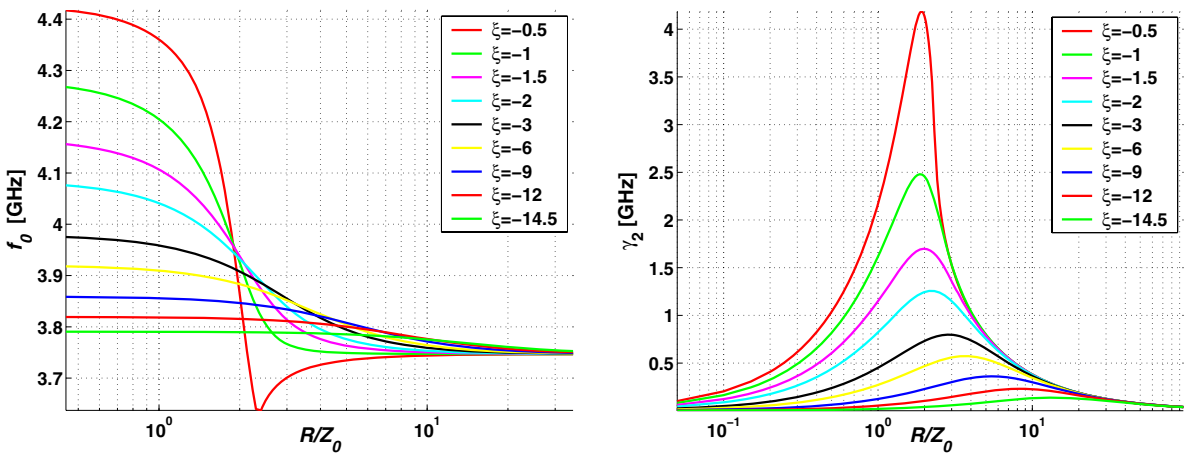

(a) (b)

Figure 3.6: (a) Resonance frequency and (b) loss factor for the $n2$ resonance mode, as a function of the normalized HED resistance, for various initial values of HED inductance.

Table 3.1: Resonance Frequency Characteristics

	Numerical Results			**Experimental Results**		
n	f_0 [GHz] $\Delta R = 0$	f_0 [GHz] $\Delta R \to \infty$	Δf_0 [MHz]	f_0 [GHz] $\Delta R = 0$	f_0 [GHz] $\Delta R \to \infty$	Δf_0 [MHz]
1	1.913	1.873	39.8	1.59	1.58	10
2	3.791	3.747	43.7	3.874, 3.711	3.829, 3.668	45, 43
3	5.654	5.62	34.1	5.634, 5.38	5.608, 5.35	26, 30

of 50Ω. The calculated inductance L of the meander line at 4.2 K without any applied current is [11]

$$L_k = \frac{\mu_0 \lambda^2}{\sigma} \left[\frac{1}{2} \left(\frac{2}{3} \left[1 - \frac{I}{I_c} \right] \right)^{-\frac{1}{2}} \right] \Bigg|_{I=0} = 6.05\text{nH}, \tag{3.6}$$

where μ_0 is the permeability of free space, σ is the cross sectional area of the line, λ is the magnetic penetration depth, and I_c is the critical current. This value is strongly dependent on temperature and current density, so the fit parameter value is in reasonable agreement with the calculated one [7].

Table 3.1 summarizes the first three solutions of Eq. 3.3 for the two extreme cases of $\Delta R = 0$ and $\Delta R \to \infty$. Comparing these results with the measured results (taken at two different cooldown cycles), is also summarized in table 3.1, showing a good agreement, especially for the second and third modes, for which the resonator is designed.

Fig. 3.7 shows the second resonance characteristics, resonance frequency and unloaded damping rate γ_2 [59], of the experimental data (blue) and the numerically

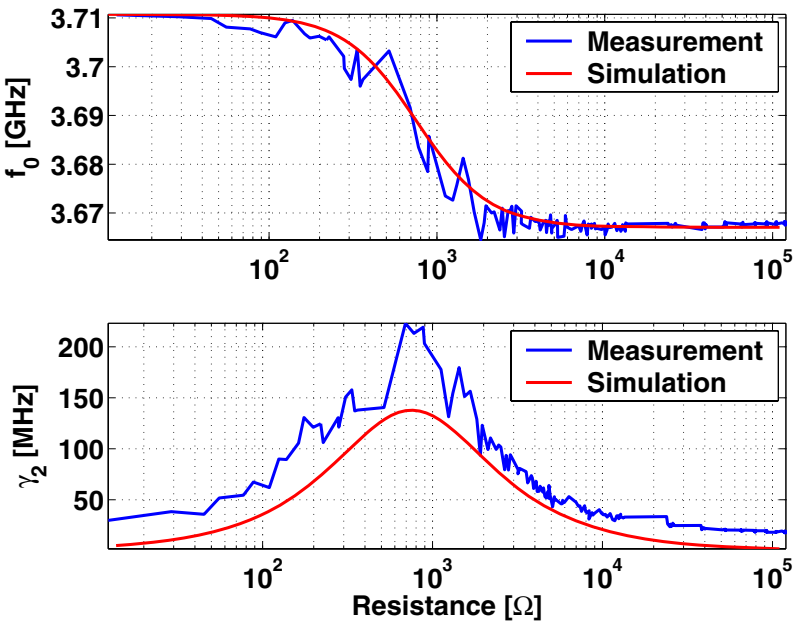

Figure 3.7: Resonance frequency and unloaded damping rate γ_2 of the second resonance mode, as a function of the HED resistance.

calculated data (red). The rate γ_2 is extracted from the data plotted in Fig. 3.3 using the method presented in the appendix of this chapter. The upper subplot shows the resonance frequency as a function of ΔR. The calculated resonance frequency, at zero resistance, is $f_0 = 3.791$ GHz, which equals the mean value of the resonance frequency measured at different cooldown cycles. In this subplot, the calculated data is corrected by -80 MHz to overlap between the first calculated and measured point. Both curves show the same dependence on ΔR. The lower subplot shows the unloaded damping rate γ_2, as a function of ΔR. Also in this case, a good agreement with the experiment is obtained, and as expected, the measured damping rate exceeds the calculated one, due to losses, which are not taken into account in the model.

The coupling between the different modes and the HED can be characterized by the current amplitude through the HED. The model predicts normalized current amplitudes of 7.3% and 5.7% inside the lumped element, for the second and third modes respectively. This rather weak coupling is the result of the rather high kinetic inductance of the HED. To estimate the coupling of modes two and three to the feedline [13], we show in Fig. 3.8 the normalized voltage amplitudes, as a function of the ring's angular location. The calculated normalized voltage amplitudes, at the feedline coupling location, are 71% and 92%, respectively. The voltage amplitudes distribution have, in general, a strong dependence on the resonance frequency, and hence on ΔR, but because of the rather small resonance shift, the voltage amplitudes at the coupling location change by less than 2%.

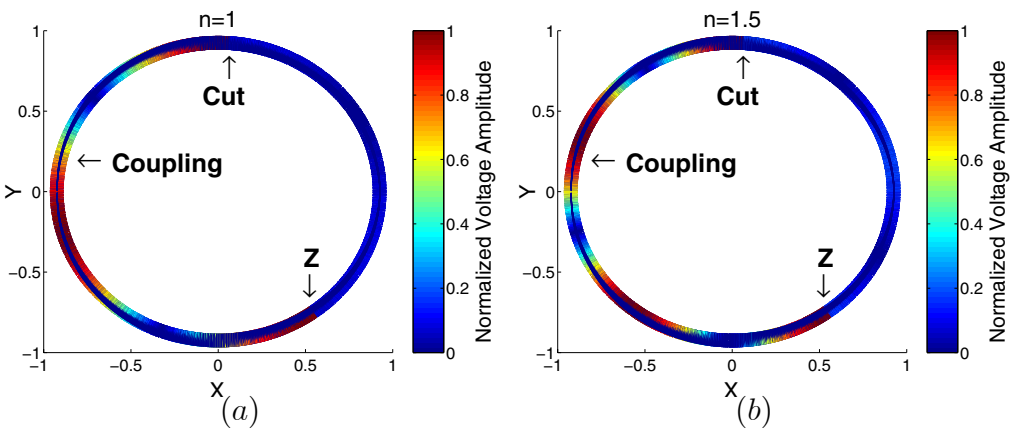

Figure 3.8: Normalized voltage amplitudes as a function of the ring's angular location, for the (a) second and (b) third resonance modes.

3.5 IR Illumination Effect on the Resonance Lineshape

Fig. 3.9 plots $|S_{11}|$ measurements with (red) and without (blue) IR illumination. The effective IR illumination power, impinging on the HED, is approximately 27 nW. The RF input power is set to -64.7dBm and the HED is biased with a subcritical dc current of $4.14\,\mu$A, which only weakly influences the resonance curve. When the illumination is turned on, the resonance frequency abruptly shifts to a lower frequency. The new resonance lineshape has the same characteristics as the resonance lineshape measured without illumination under supercritical bias current of $I = 4.39\,\mu\text{A} > I_{C1}$. This measurement clearly shows that the resonance frequency is sensitive to IR illumination. The measured results in this experiment yield $\xi Q \cong 4.14$.

3.6 Summary

The resulting effect of applied dc voltage and current as well as CW IR illumination on the resonance frequencies is investigated. The parametric gain threshold condition is achieved in the CW measurement. Moreover, the results are shown to be in a good agreement with a theoretical modeling.

3.A Damping Rate Extraction

The universal expression for the reflection amplitude of a linear resonator near resonance is [59], [3]

$$S_{11} = \frac{i\Omega + (\gamma_1 - \gamma_2)}{i\Omega - (\gamma_1 + \gamma_2)}, \tag{3.7}$$

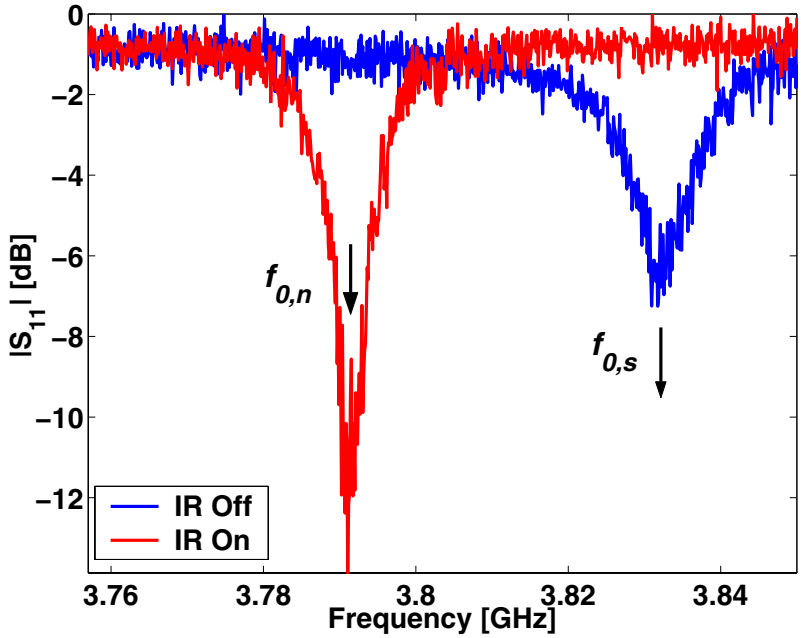

Figure 3.9: Several $|S_{11}|$ measurements of the second resonance mode, as a function of frequency, while applying sub-critical current, with (red) and without (blue) IR illumination.

and the reflection probability R is

$$R = |S_{11}|^2 = \frac{\Omega^2 + (\gamma_1 - \gamma_2)^2}{\Omega^2 + (\gamma_1 + \gamma_2)^2} \tag{3.8}$$

where $\Omega = \omega_p - \omega_0$ is the pump angular frequency ω_p, relative to the angular resonance frequency ω_0, γ_1 is the coupling constant between the resonator and the feedline, and γ_2 is the unloaded damping rate of the resonance.

3.A.1 First Order Extraction

The damping rate is numerically extracted by expanding Eq. (3.7) to first order in Ω,

$$S_{11} = r_0 + r_1\Omega + O\left(\Omega^2\right), \tag{3.9}$$

where r_0 is the S_{11} value at the resonance frequency,

$$r_0 = \frac{\gamma_2 - \gamma_1}{\gamma_1 + \gamma_2}, \tag{3.10}$$

and r_1 is the slope of the imaginary part of S_{11},

$$r_1 = -i\frac{2\gamma_1}{(\gamma_1 + \gamma_2)^2}. \tag{3.11}$$

Note that the extraction of r_1 is less accurate for low Q-factor curves, and thus the calculated loss factor suffers from a rather large impreciseness at that region.

3.A.2 Second Order Extraction

The damping rate is numerically extracted by expanding Eq. (3.8) to second order in Ω,

$$R = R_0 + R_2\Omega^2 + O\left(\Omega^4\right) \tag{3.12}$$

where R_0 is the S_{11} value at the resonance frequency,

$$R_0 = \frac{\left(\gamma_1 - \gamma_2\right)^2}{\left(\gamma_1 + \gamma_2\right)^2} \tag{3.13}$$

and R_2 is the curvature of the resonance curve in the vicinity of the resonance frequency,

$$R_2 = \frac{1 - R_0}{\left(\gamma_1 + \gamma_2\right)^2}. \tag{3.14}$$

The coupling constant and the damping rate are analytically extracted, and given by

$$\begin{aligned} \gamma_2 &= \frac{1}{2}\left[\sqrt{\frac{1-R_0}{R_2}}\left(1 \pm \sqrt{R_0}\right)\right], \\ \gamma_1 &= \frac{1}{2}\left[\sqrt{\frac{1-R_0}{R_2}}\left(1 \mp \sqrt{R_0}\right)\right]. \end{aligned} \tag{3.15}$$

Note that the second order extraction is less effected by noise than the first order extraction, but on the other hand, as it ignores the measured phase data, it is less accurate.

Chapter 4

Self-Sustained Oscillations

4.1 Introduction

Current-carrying superconductors are known to have two or more metastable states sustained by Joule self-heating [29]. One state is the SC state and the other is an electrothermal local state, known as hotspot, which is basically an island of NC area, with a temperature above the critical one, surrounded by a SC domain. This phenomenon can be explained by the heat balance equation holding at more than one temperature, as explained in section 4.5. Due to an external [31] or internal [32] perturbation, the hot spot can recover to the SC state or vice versa, and thus oscillates between bistable states. Such self-sustained oscillations were often observed in experiments, for the case of a SC microbridge driven by external voltage or current (see [29] and reference therein). This phenomena attracts new attention with the growing field of SC hot-electron bolometers aimed at detecting terahertz radiation [27], [28].

In this chapter we report on a new nonlinear phenomena, in which self-sustained oscillations are generated in the resonator, that is, the resonator undergoes limited cycle oscillations. The oscillations frequency is not a natural resonance frequency of the resonator, and thus the oscillations are referred to as self-modulations (SM) of the stimulating pump signal. Oscillation at several different time periods are observed. Oscillations frequency ranges between tenth of MHz, to which we'll refer to as high frequency self modulations (HFSM), and few Hz or less, to which we'll refer to as low frequency self oscillations (LFSO). To the best of our knowledge such SM were not reported before in similar systems. To account for our findings we propose in section 4.5 a theoretical model according to which the self-sustained oscillations are originated by thermal instability in the meander strip. The origin of instability is the coupling between the heat balance equation and the equation of motion of the mode amplitude in the resonator.

This chapter is organized as follows. First, section 4.2 describes the HFSM characteristic behavior, common to all the devices and resonance modes. Than, section 4.3 describes additional HFSM characteristic behaviors which are device dependent, that is, behaviors which are usually measured at only one of the devices. Following, , section 4.4 describes the LFSO characteristic behavior, and its correlation to the HFSM. Finally, section 4.5 presents a preliminary theoretical model, which yields a partial

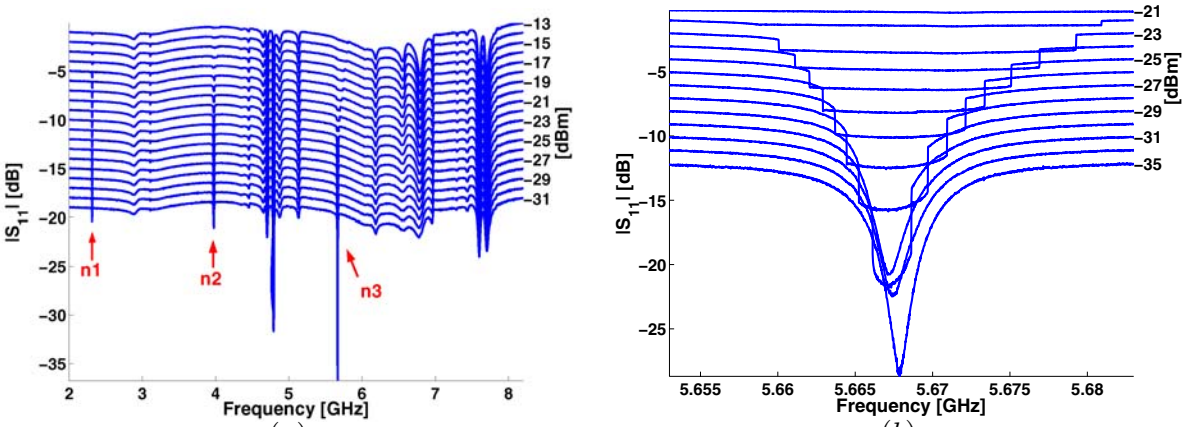

Figure 4.1: Several $|S_{11}|$ measurements of E15 resonator as a function of frequency in the (a) resonator frequency range and (b) vicinity of the third resonance frequency. The measurements, shifted vertically for clarity, are obtained for increasing input powers.

qualitative agreement with the experimental results.

4.2 Common Self-Modulation Characteristic Behavior

The following section describes the HFSM phenomena. In order to give a coherent observation, all measurements presented in this section are performed on E15 device, at the same resonance mode. Experimental results taken at other resonance modes or devices, that gives additional perspective on the phenomena are described in the next section.

4.2.1 Collapsing Resonance Curves

The first measurement, that indicates the presence of some unusual nonlinear behavior in our resonator, is a simple broadband $|S_{11}|$ reflection measurement of the resonator's frequency range, using a NA connected to the resonator's RF port. Fig. 4.1(a) plots various $|S_{11}|$ curves as a function of frequency. Each curve represents a measurement with a different RF input power. The curves are vertically shifted upwards, for increasing power values, for clarity. The resonator has only one port and therefore resonance frequencies are characterizes by a deep in the $|S_{11}|$ curve. E15 has three resonance modes at the observed frequency range, marked as $n1 - n3$, found at frequencies, $f_1 = 2.314\,\text{GHz}$, $f_2 = 3.976\,\text{GHz}$, and $f_3 = 5.666\,\text{GHz}$ respectively. In this simple measurement all resonance curves seem to collapse and disappear as the input power increases.

Fig. 4.1(b) shows a similar $|S_{11}|$ measurement in the vicinity of $n3$ resonance. At low input powers the resonance lineshape is linear, but above a certain threshold power the $|S_{11}|$ lineshape looses its normal Lorensian shape. In this power range the

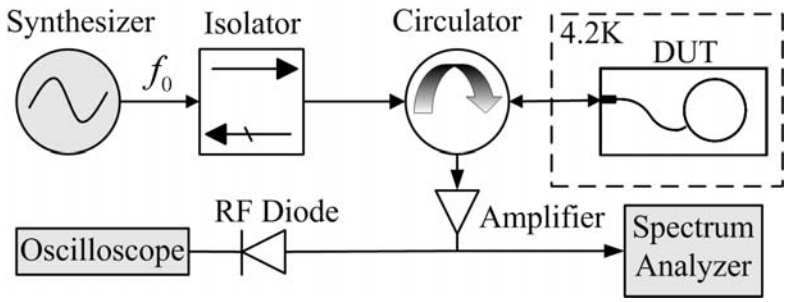

Figure 4.2: Setup used for SM reflection measurements.

$|S_{11}|$ value substantially increases, the resonance curve is substantially broaden and has steep edges. This behavior continues and intensifies, as the pump power increases, until no resonance curve in detected.

To gain more insight on the HFSM phenomena we change our experiment setup to a more flexible one. The NA is replaced with a synthesizer (SYN) and the reflected power off the resonator, amplified at room temperature, is measured with a Spectrum Analyzer (SA) and a time domain oscilloscope (OSC), as shown in Fig 4.2.

The next experiment checks the existence of power hysteretic behavior of the $n3$ resonance curve. We test the dependence of the reflection parameter $|S_{11}|$ on the input pump power P_{pump}, as we fix the pump frequency f_{pump}, and increase or decrease the pump power. Fig. 4.3(a) and 4.3(b) show these two measurements, respectively. One can easily identify the threshold power region, at which the $|S_{11}|$ changes dramatically and the resonance curves loose their Lorensian shape. An even smaller region, at which the $|S_{11}|$ is extremely low, is observed. Comparing the two graphs we notice that at relatively low power range the resonance line shapes are similar but at relatively moderate and high power range the resonance line shapes differ one from another. This indicates the presence of an hysteresis loop corresponding to a change of the input power.

4.2.2 Self-Modulation Characterization in the Frequency Domain

HFSM Dependence on Pump Power

The measurements presented so far only describes the response of the resonator at the frequency at which it is being stimulated. Next we examine its response, to a CW stimulation, at a wider frequency band.

In the next experiment the resonator is excited with a CW pump signal, at frequency f_3. Fig. 4.4 shows the reflected power P_{refl}, measured in a frequency band of 200 MHz around $n3$ resonance. $f_c = f - f_3$ is the centered span frequency around the resonance frequency.

Panel (a) plots P_{refl} while the pump power is set below threshold. The resonator behavior is linear so the only measured signal is the pump signal, reflected off the resonator. Panel (b) plots P_{refl} while the pump power is set to the threshold power.

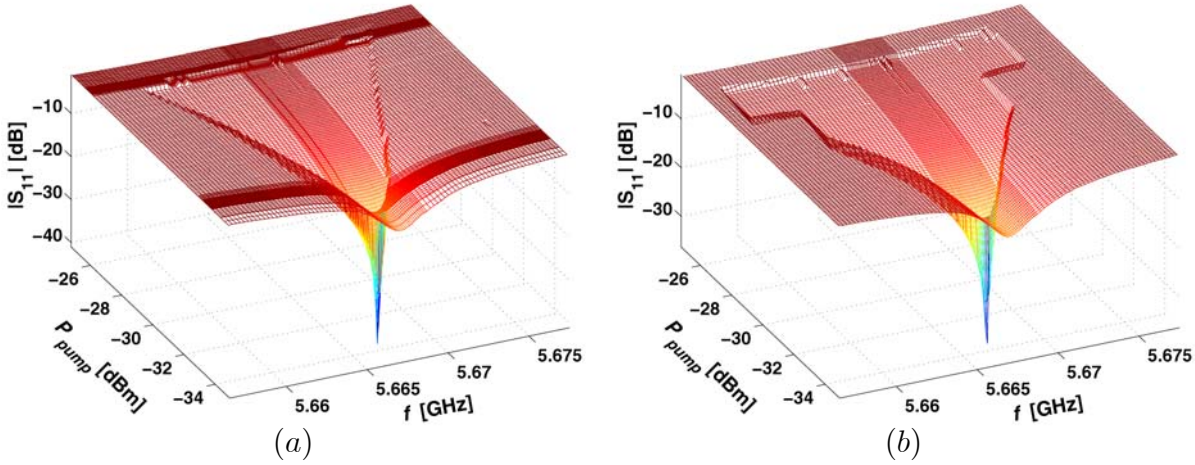

Figure 4.3: $|S_{11}|$ measurement as a function of pump frequency and (a) increased pump power sweep, (b) decreased pump power sweep.

The behavior of the resonator turns chaotic-like, and is characterized by a strong amplification of the noise floor, over a rather large frequency bandwidth, centered around the resonance frequency. The amplification is always strong in the vicinity of the resonance frequency, but in general, it is not always symmetric nor continuous. The threshold power range is very narrow, and spans only about 10 nW. When the input power is increased above threshold, the resonator breaks into regular HFSM of the pump signal. Panel (c) shows a common measurement of the reflected power spectrum at that region. The reflected pump power has several strong and rather sharp sidebands, symmetrically splitting around it. The self modulation frequency, f_{SM}, is defined as the different between the pump frequency and the frequency of the first sideband. These measurements indicate the presence of a strong nonlinear mechanism in the resonator, that causes modulations of the pump signal. Panel (d) plots P_{refl} while the pump power is set to the second threshold power, before which the HFSM ends. This range is characterized by a large amplification of the noise floor on a noncontinuous broadband frequency range, similar to the first chaotic-like range.

The HFSM is strongly dependent on the pump power. Fig. 4.5 plots a three dimensional flat view (3DFV) of the reflected power P_{refl}, in a frequency band of 200 MHz around $n3$ resonance, as a function of the pump power, P_{pump}, while the resonator is stimulated with a CW signal at frequency $f = f_3$. This graph shows the dependence of the HFSM on the pump power, which can be divided into 5 power ranges:

1. At low input power, approximately below -32dBm the behavior of the device is linear, and no HFSM are observed.

2. The threshold power of the HFSM occurs on a very narrow power range of approximately 10 nW. At this range the behavior of the device is chaotic-like. There is a strong amplification of the noise floor over a rather large frequency band and especially around the resonance mode itself.

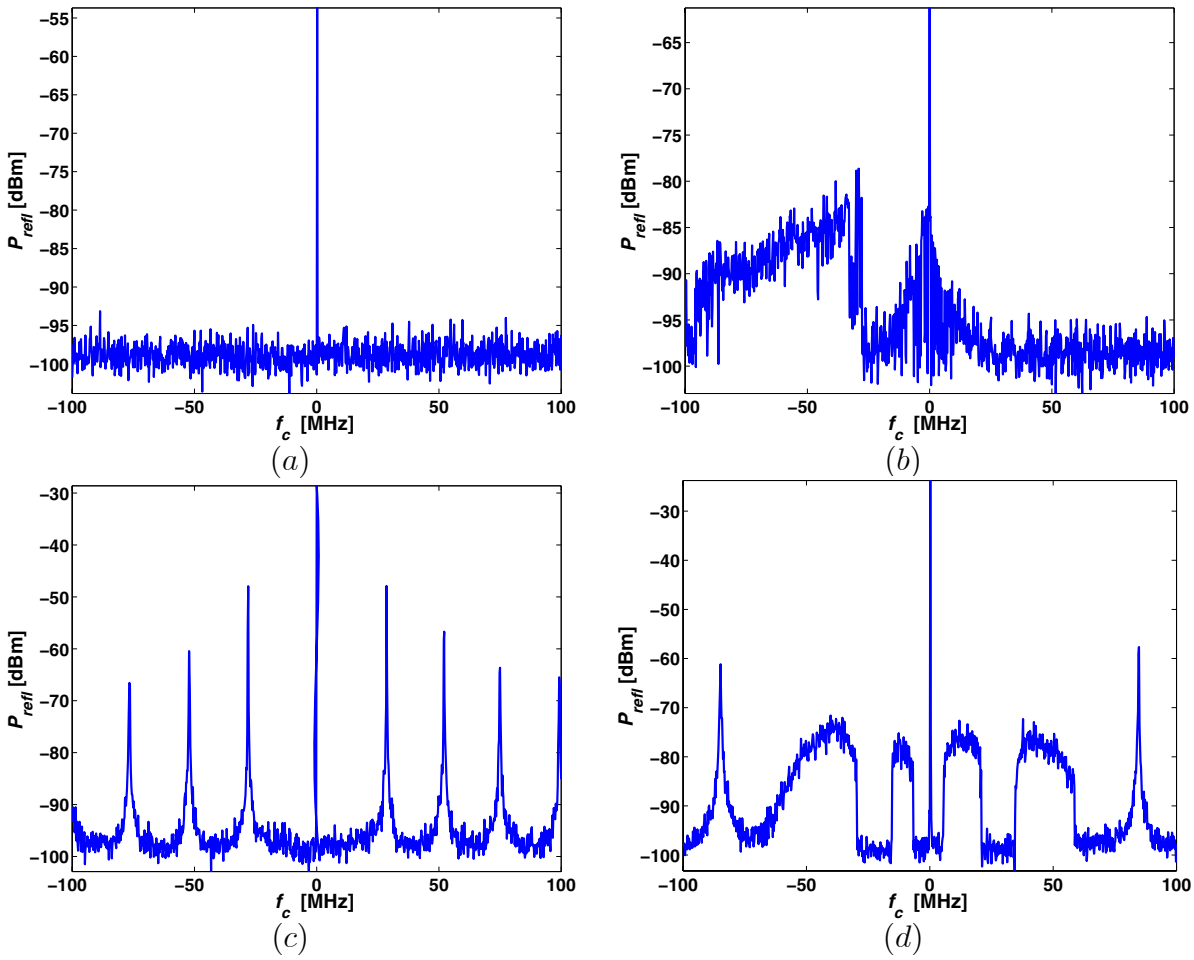

Figure 4.4: Reflected power measured in a frequency band of 200MHz around n3 resonance. The pump power is set (a) below first threshold power, (b) at the first threshold power, (c) above first threshold power, and (d) at second threshold power.

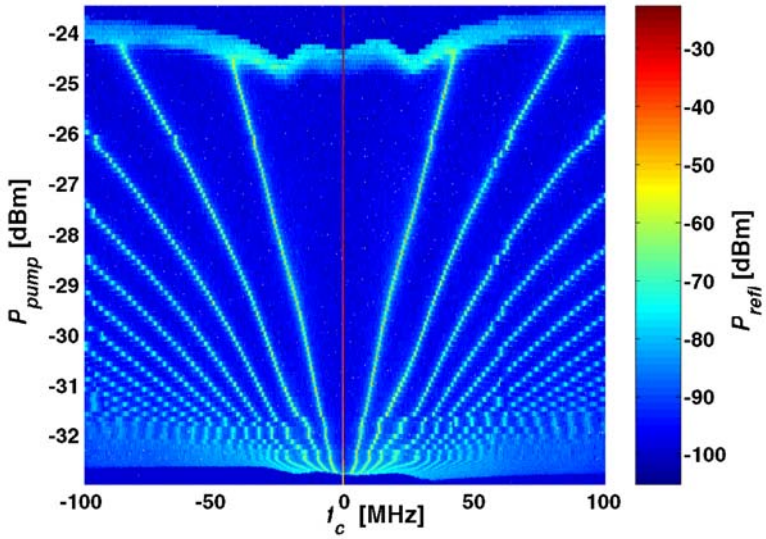

Figure 4.5: 3DFV of the reflected power P_{refl}, in a frequency band of 200 MHz around $n3$ resonance, as a function of the pump power P_{pump}. The pump frequency equals the resonance frequency.

3. Above threshold power, there is a rather large power range, at which regular HFSM of the pump signal occur. The modulation frequency is dependent on the pump power, and is increased as the pump power increases.

4. Another chaotic-like behavior occurs before the HFSM ends. It occurs on a slightly larger power range than the first one and is characterized by a large amplification of the noise floor on a noncontinuous broadband frequency range.

5. Above this power range the HFSM ends and the resonator behavior is linear.

HFSM Dependence on Pump Frequency

The HFSM is also strongly dependent on the pump frequency. Fig. 4.6 plots a 3DFV of the reflected power P_{refl}, in a frequency band of 200 MHz around $n3$ resonance, as a function of the centered pump frequency around $n3$ resonance frequency, f^c_{pump}. The resonator is stimulated by a CW pump power of $P_{pump} = 23.6$dBm, which sets the resonator to the regular HFSM region. The reflected pump signal is the strongest reflected signal and can be detected as the red diagonal line in the center of the figure. At both its sides the reflected sidebands power is detected. We notice that the HFSM only occurs in a well defined pump frequency range around the resonance frequency. The HFSM can start and end abruptly as a response to a small change in the pump frequency. Once started the HFSM frequency has a rather weak dependence on the pump frequency, which suggest a low effective Q-factor at that region.

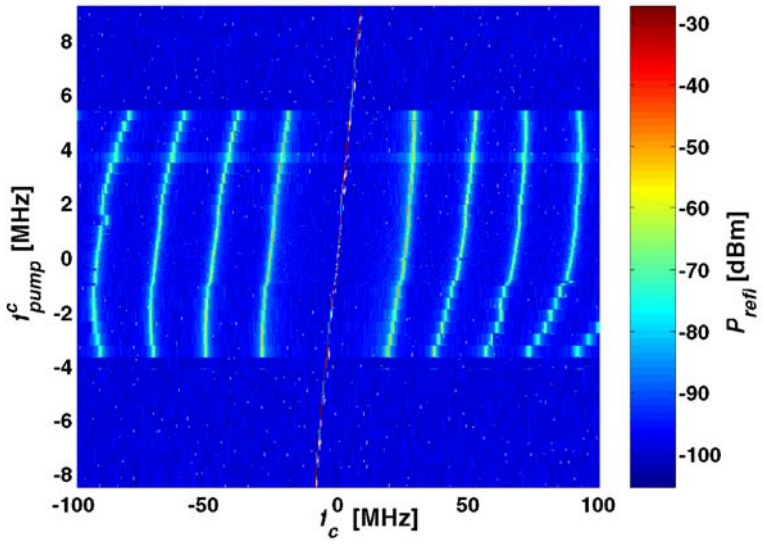

Figure 4.6: 3DFV of the reflected power P_{refl}, in a frequency band of 200 MHz around $n3$ resonance, as a function of f^c_{pump}, the centered pump frequency around $n3$ resonance frequency. The resonator is set to the regular SM power regime.

HFSM Dependence on Pump Power & Frequency

Fig. 4.7 plots the HFSM frequency f_{SM}, as a function of the pump power P_{pump}, and pump frequency f_{pump}. It completely describes the HFSM dependence on these parameters. A few points should be emphasized:

1. The HFSM only occur at a well defined frequency range around the resonance frequency. The onset power, at which the SM start, is strongly dependent on the pump frequency, and occurs at a lower power when the pump frequency is closer to the resonance frequency.

2. A small change in the pump frequency can abruptly start or stop the HFSM. On the other hand, once started, the modulation frequency has a week dependence on the pump frequency. This week dependence suggests that the resonator has a rather small effective Q-factor at that region.

3. There is a positive correlation between the pump power and the SM frequency. The maximum SM frequency measured on this device is approximately 40 MHz, where an even higher maximum SM frequency of approximately 60 MHz, is measured on other devices.

4.2.3 Self-Modulation Characterization in the Time Domain

Observation of the HFSM in the time domain gives a complementary view on the phenomena. For this purpose we added a fast oscilloscope which samples the reflected

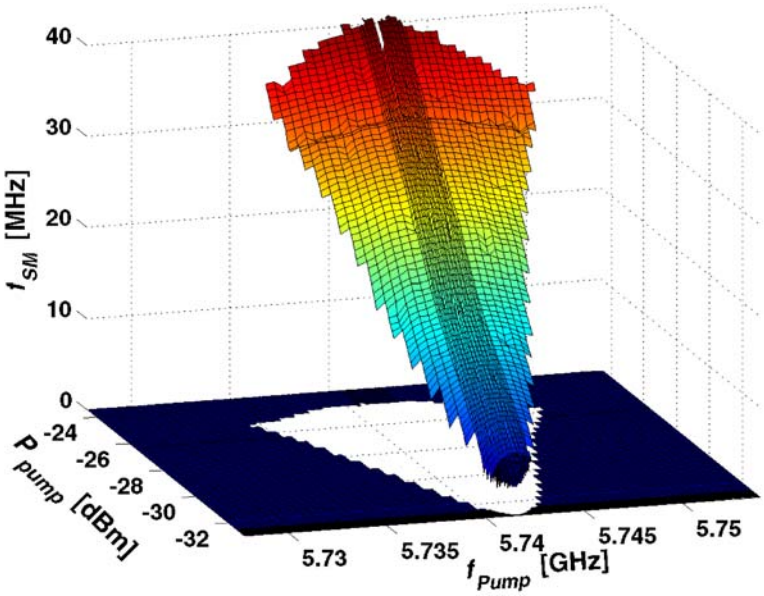

Figure 4.7: SM frequency f_{sm}, as a function of the pump power P_{pump}, and pump frequency f_{pump}.

power at the time domain. The reflected power is linearly converted by an RF diode into a correlated voltage amplitude, prior to sampling.

The results of the experiment are shown in Fig. 4.8, where the resonator is excited by a CW pump signal at f_3 frequency. It has four panels, where each has two subplots. The upper subplot shows the reflected power P_{refl}, as a function of time and the lower subplot shows P_{refl} in the frequency domain, measured simultaneously by the SA, for comparison. The panels, marked $(a) - (d)$, refer to measurements taken with pump powers of -34.44dBm, -34.43dBm, -28.55dBm, and -26.67dBm, respectively. Each panel refers to a different state of the resonator, (a) first threshold, (b) regular modulation, right above threshold (c) regular modulation, and (d) second threshold.

The dependence of the HFSM on the input power, as observed in the time domain, is described as follows. Naturally, below threshold power, no oscillations of the reflected power are observed. Once the threshold power is achieved sporadic oscillations appear. Panel (a) shows a measurement, in which only one oscillation fits into the measured time frame. Additional measurements show that the lineshape of the oscillations is rather repetitive, but the time phase at which they appear, looks random. Above threshold power regular oscillations occur. At first, the lineshape of the oscillations is composed of a sharp drop in the reflected power and an exponential, rather slower, incline, as seen in panel (b). As the oscillations' frequency gets higher the exponential incline gets faster and oscillations' lineshape resembles saw like shape, as seen in panel (c). At the second chaotic-like power range (d), the oscillations change their shape and again appear randomly in time. Above this power range the oscillations stop.

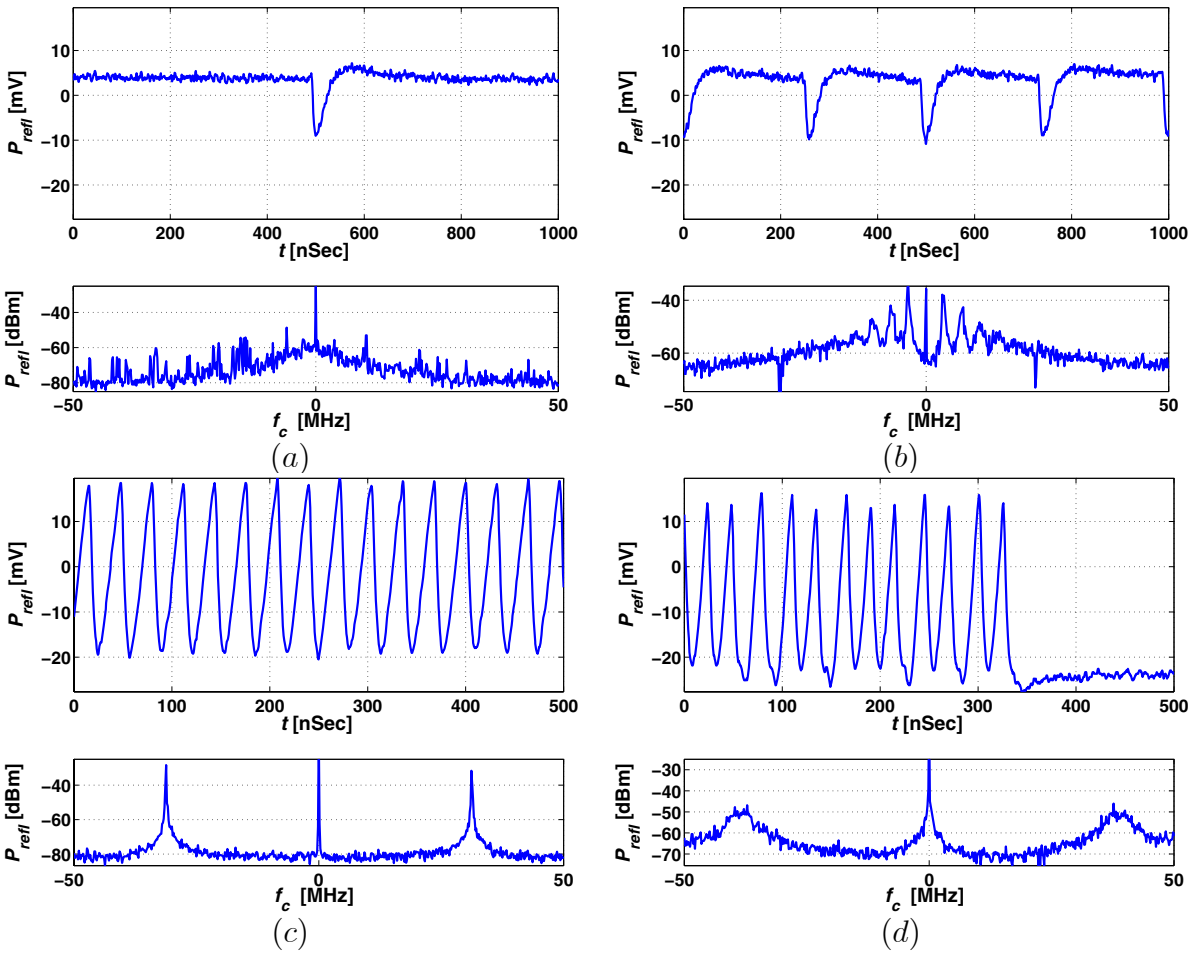

Figure 4.8: Reflected power as a function of time. Pump frequency equals f_3 frequency.Each panel refers to a different state of the resonator, (a) first threshold, (b) regular modulation, right above threshold (c) regular modulation, and (d) second threshold. Each panel has two subplots. The upper subplot shows the reflected power as a function of time. The lower subplot shows the reflected power in the frequency domain, for comparison

4.3 Unique Self-Modulation Characteristic Behavior

The SM phenomena is a robust behavior of our devices. It is observed in all devices, at various resonance frequencies and various power ranges. As the devices differ in geometry, the HFSM behavior also has device dependent characteristics. For example, the threshold power, at which the SM end, only shows chaotic-like behavior in E15 device. For the sake of coherent description of the HFSM, section 4.2 presents measurement data that is collected from the $n3$ resonance mode of E15 only. The following section presents additional HFSM results, that are collected at different resonance modes and devices. The measurement results, shown in this section, can be divided into three categories. The first are results that are not common to all devices, but are robust in the mode at which they are measured. The second are results of measurements that were not performed on all devices. The third are important measurements that should be presented for more that one mode.

4.3.1 Self-Modulation at Two Distinct Power Ranges

The HFSM behavior, as presented in the previous section for E15, does no reveal the full extent of the phenomena at that device. The full extent is only revealed once we measure the $|S_{11}|$ parameter at low input powers. The results are shown in Fig. 4.9, which extends the results shown in Fig. 4.1(b) to input powers lower than -35dBm. It plots various $|S_{11}|$ curves as a function of frequency, in the vicinity of $n3$ resonance, $f_3 = 5.666\,\text{GHz}$. The curves are vertically shifted, for clarity. The green curve, marked for clarity, measured at input power of -60dBm, shows a second resonance curve, red shifted by approximately 10 MHz relatively to f_3. The resonance curve, marked as $n3^*$, represents a linear behavior of the resonator. As the input power is increased from -55dBm to -46dBm the resonance curve slowly blue shifts towards f_3 frequency and the Q-factor increases. The red curves, marked for clarity, show the resonance curve at the transition itself. The behavior of the resonance frequency above this power range is described at 4.1(b).

Fig. 4.10(a) plots the reflected power P_{refl}, as a function of frequency in the vicinity of $n3^*$, and shows a typical measurement of the HFSM at low power range. The data is taken at pump power and frequency of -58.2dBm and 5.656 GHz respectively. Comparing this graph to 4.1(b) we notice that the sidebands measured at low power are broaden, weaker and less symmetric than the ones measured at high power. Nevertheless, they follow the same power dependence, in which the HFSM start with a chaotic-like region and followed by regular HFSM. Fig. 4.10(b) summarizes the HFSM frequency f_{SM}, as a function of the pump power P_{pump}, and pump frequency f_{pump} in the vicinity of $n3^*$. As one can see, the HFSM exhibit the same dependence on the pump power and frequency as the high power HFSM and a maximum SM frequency of 20 MHz is measured.

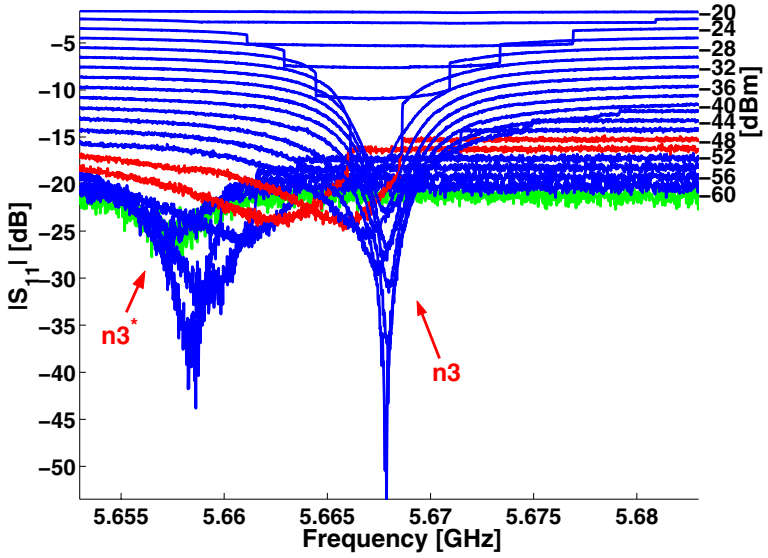

Figure 4.9: Several low power $|S_{11}|$ measurement of E15 resonator as a function of frequency in the vicinity of $n3$ resonance. The measurements, shifted vertically for clarity, are obtained for increasing input powers.

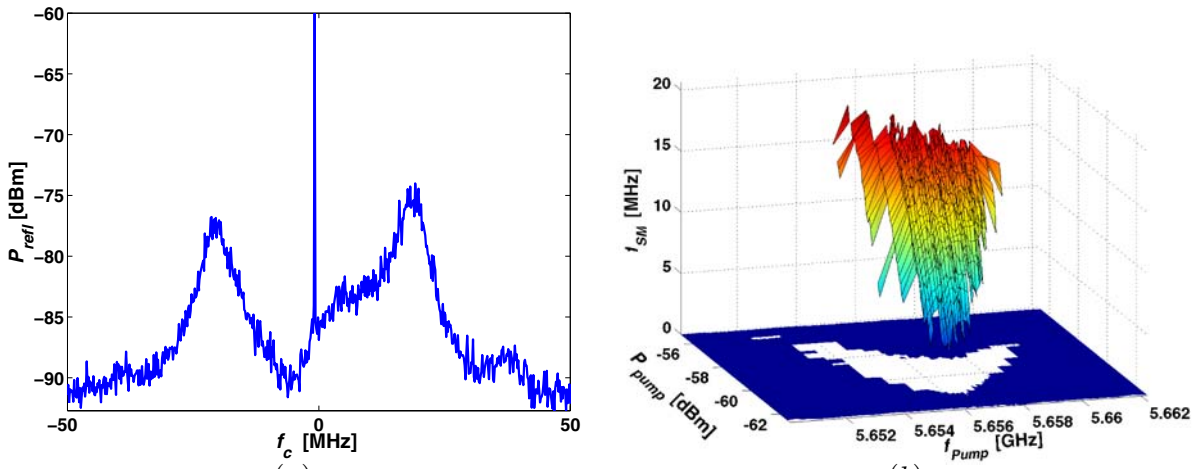

(a) (b)

Figure 4.10: (a) Reflected power measured in a frequency band of 200MHz around $n3^*$ resonance. Pump power is set above the rather low threshold power. Pump frequency equals $N3^*$ resonance frequency.(b) SM frequency as a function of the pump power and pump frequency in the vicinity of $n3^*$.

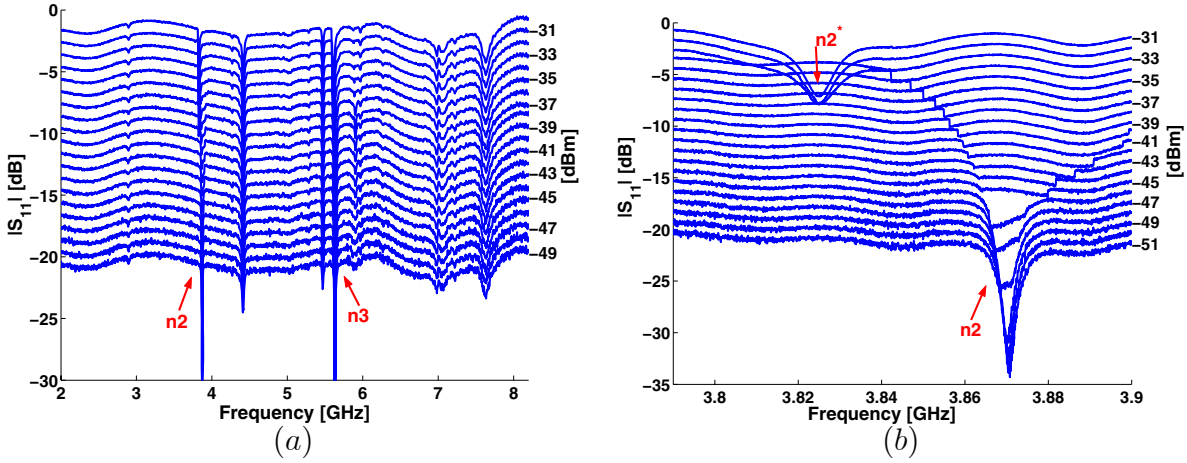

Figure 4.11: several $|S_{11}|$ measurements of E16, as a function of frequency in the (a) resonator frequency band and (b) vicinity of the second resonance mode. The measurements, shifted vertically for clarity, are obtained for increasing input powers.

4.3.2 Self-Modulation Phenomena at low powers

The same measurements that have been performed on E15 are also performed on E16. E16 is designed for the same resonance frequencies as E15, but differs in two major aspects. First, it has a much thinner NbN layer than E16, 8 nm as opposed to 200 nm, therefore all nonlinear phenomenons in general, and in particular the HFSM should start at a lower threshold power. Second, E16's HED has a meander shape as opposed to the single, wider strip, composing E15's HED.

Collapsing Resonance Curves

Fig. 4.11(a) plots various broadband $|S_{11}|$ measurements, as a function of frequency, of E16 frequency range. The curves are vertically shifted upwards, for increasing measurement power, for clarity. The first resonance mode is not observed and the second and third modes, marked as $n2$ and $n3$, are observed at frequencies $f_2 = 3.87$ GHz and $f_3 = 5.63$ GHz, respectively. Fig. 4.11(b) shows a similar $|S_{11}|$ measurement in the vicinity of $n2$ resonance. The lineshape of the resonance curve follows the same power dependency as in Fig.4.1(b), but at respectively high power levels, the resonance curve is reconstructed at a new resonance frequency, red shifted by approximately 40 MHz relative to f_2. The lineshape of the new resonance frequency, marked as $n2^*$, represents a linear behavior of the resonator at that region. The difference between this measurement and the one presented in Fig.4.1(b) is not surprising. As E16's HED has much smaller dimensions that E15's HED, its has a much higher characteristic impedance at the NC state, and an higher radio of z/z_0 is achieved in Eq. 3.3.

The resonance frequencies of E16 has similar power hysteresis loop as the resonance curves of E15. In addition, we performed a measurement that checks the presence of frequency hysteresis loops. We test the dependence of the $|S_{11}|$ reflection parameter on the input pump frequency f_{pump}, as we fix the pump input power P_{pump}, and increase or decrease the pump frequency. The results are plotted in 4.12, where

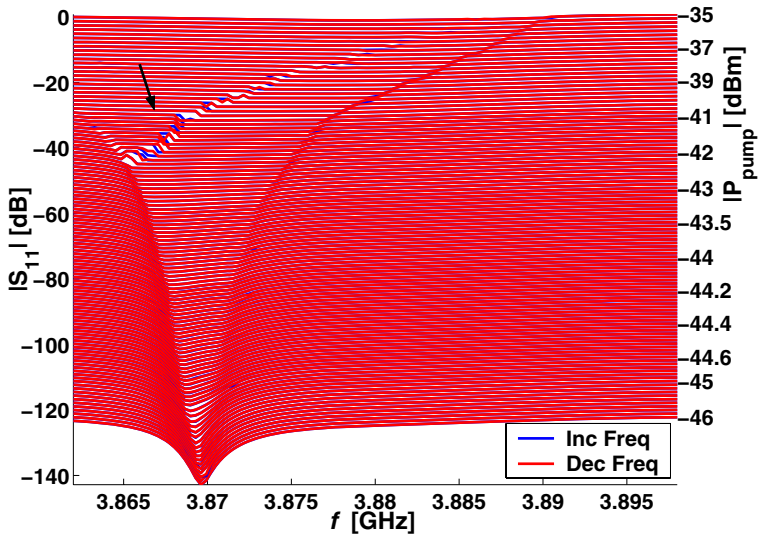

Figure 4.12: Several $|S_{11}|$ curves, in the vicinity of $n2$ resonance, as a function of pump power and increasing (blue) or decreasing (red) pump frequency sweeps.

various $|S_{11}|$ curves are plotted as a function of frequency. The curves are vertically shifted upwards, for increasing power values, for clarity. Blue (red) curves represent measurements with increasing (decreasing) frequency sweep. As one sees, the red curve totally covers the blue curve at most of the employed power levels and frequencies. Slight hysteresis may be present at the area pointed, marked by the black arrow, but no further measurements were made to characterize it.

SM Observations in the Frequency Domain

The HFSM phenomena, as measured in E16, follows the same power and frequency dependence as in E15, with two major differences. First, the HFSM threshold power is about two orders of magnitude lower than the threshold power in E15. This is a reasonable difference, as there is more than 3 order of magnitude difference between the narrowest cross section of E15 and E16 (at the HED). Second, E16 has no chaotic-like behavior at the HFSM turn-off power region as E15 has. At this point we have no explanation for that behavior.

Mainly for the sake of redundancy, Fig. 4.13 shows the reflected power P_{refl}, measured in a frequency band of 200 MHz, in the vicinity of the $n2$ resonance. $f_c = f - f_2$ is the centered span frequency around f_2. The resonator is excited with a CW signal at frequency f_2. Panel (a) is measured, while the pump power is set below threshold, and the resonator behavior is linear. Panel (b) is measured while the pump power is set to the threshold power. The behavior of the resonator is chaotic-like, and characterized by a strong amplification of the noise floor, over a rather large frequency bandwidth, centered around the resonance frequency. In E16, the amplification is always strongest in the vicinity of the resonance frequency, and is continuous but asymmetric in frequency. The threshold power range is still very narrow. When the

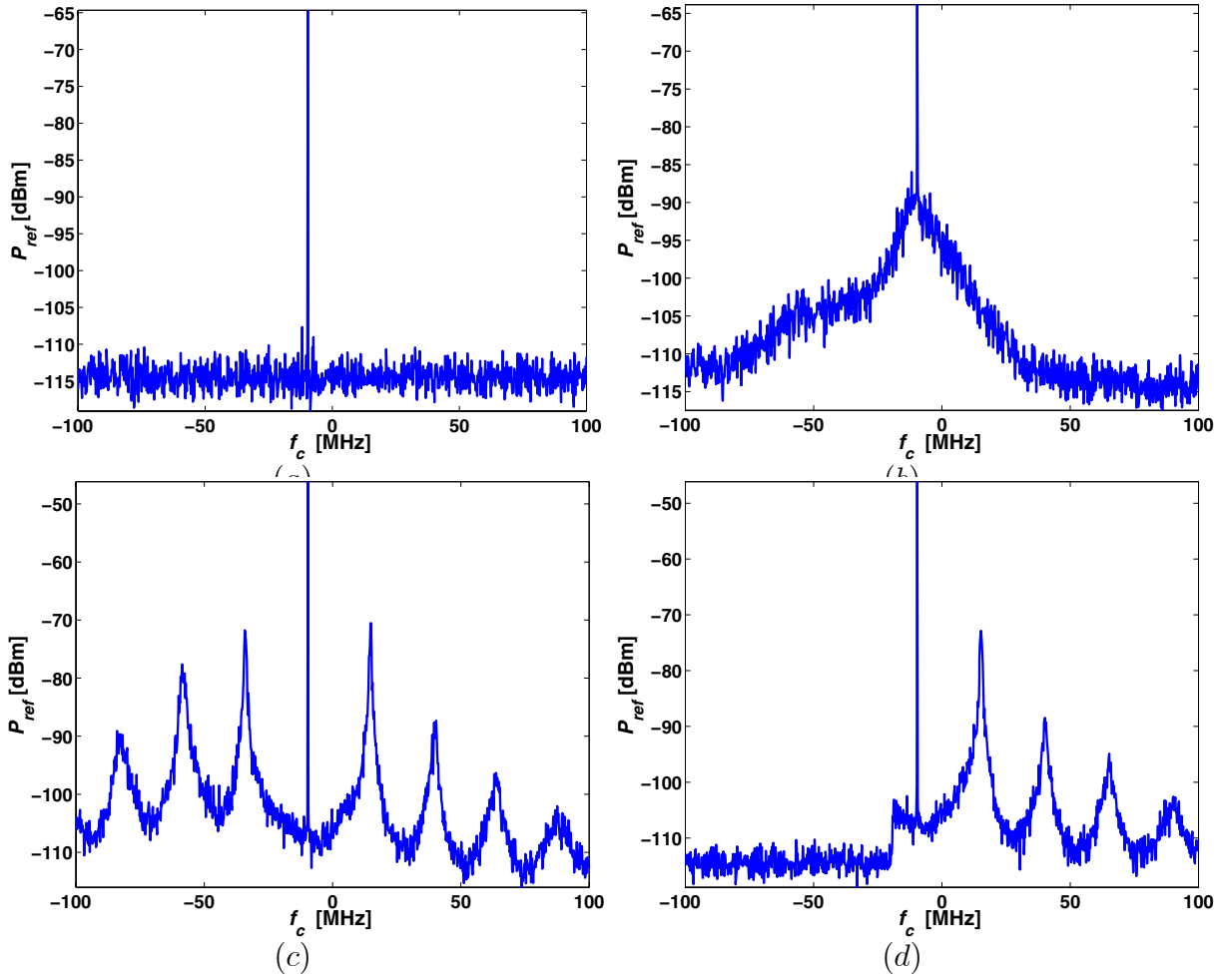

Figure 4.13: Reflected power measured in a frequency band of 200MHz around $n2$ resonance. The pump power is set (a) below first threshold power, (b) at the first threshold power, (c) above first threshold power, and (d) at second threshold power.

input power is increased above threshold, the resonator breaks into regular HFSM of the pump signal. Panel (c) shows a typical reflected power spectrum of a modulated signal, in which the asymmetric character of the sideband is observed. Panel (d) is measured while the pump power is set to the second threshold power, before which the HFSM ends. The resonator is highly unstable and switch back and forth from a state, at which HFSM exists to a state where it does not. The switching is so rapid that, as seen in panel (d), the HFSM sidebands are only measured approximately half of the SA sweep cycle.

The resonance frequencies of E16 show power hysteresis loop. Fig. 4.14 plots the SM frequency f_{SM}, as a function of the pump power P_{pump}, and pump frequency f_{pump}. Panels (a) and (b) are taken under an increasing and decreasing input power sweeps respectively. At both panels the asymmetric dependence of the HFSM on the pump frequency is realized. The presence of the power hysteresis loop is clear, where the maximum modulation frequency measured at cases (a) and (b) are 57.6 MHz and 34.8 MHz, respectively.

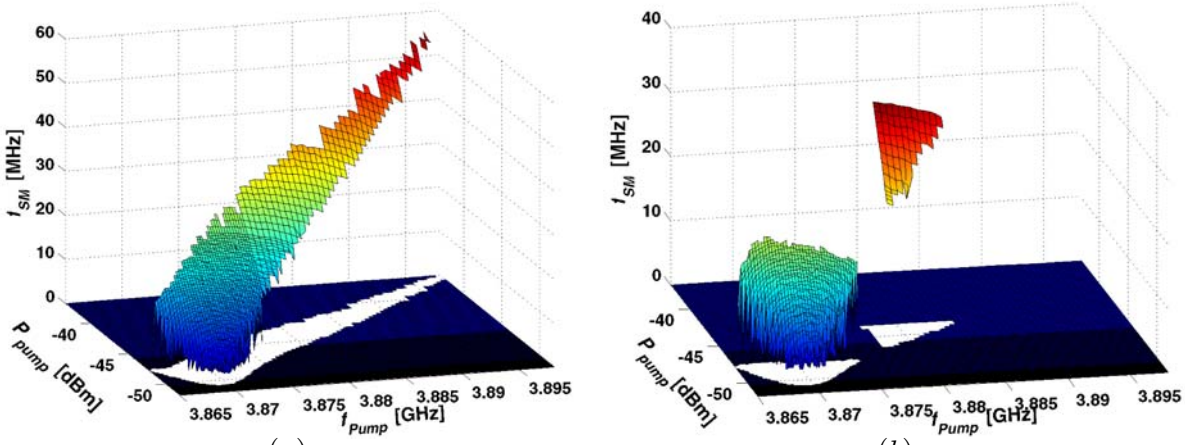

(a) (b)

Figure 4.14: SM frequency as a function of the pump frequency and (a) increasing or (b) decreasing pump power sweeps.

SM Observations in the Time Domain

The measured HFSM in the time domain are shown in Fig. 4.15, where the resonator is excited by a CW signal at f_2 frequency. It has three panels, where each has three subplots. The upper two subplots show the reflected power P_{refl}, as a function of time, where the right subplot shows the same measurement at a narrower time slot. The lower subplot shows the reflected power at the frequency domain, measured by the SA, for comparison. The panels, marked $(a) - (c)$, refer to measurements taken with pump powers of -51.53dBm, -50.88dBm, and -47.58dBm respectively. Each panel refers to a different state of the resonator, (a) threshold region, (b) regular modulation, right above threshold, and (c) regular modulation before turn off.

Despite the differences between E16 and E15, both have similar self-oscillation lineshape at the time domain. The lineshape and the time phase between oscillation in E16 are slightly less regular, which explains the wider sidebands at the frequency domain.

4.3.3 Noncontinuous Amplification at Threshold Power

E13 has similar design properties as E15. They both share the same NbN thickness and HED geometric profile. E13 is aimed at different resonance frequencies than E15, and as so differ in the angular location of the HED, in respect to the feedline and the cut. Measuring the $|S_{11}|$ reflection parameter as a function of frequency and input power, as shown in Fig. 4.16 reveals, that the difference between the two is more fundamental. Four groups of resonance frequencies are observed, marked as $n1x - n4x$, where x is an index. Each group has few resonance frequencies that are coupled one to another in a way that would be describes shortly. Some resonance modes, such as $n1a$, $n3b$, $n3c$, and $n4a$ collapses and disappear as the input power increases, as similar to the behavior measured at E15. Other modes collapse and then are reconstructed at a new resonance frequency, a few tenth of MHz away from their

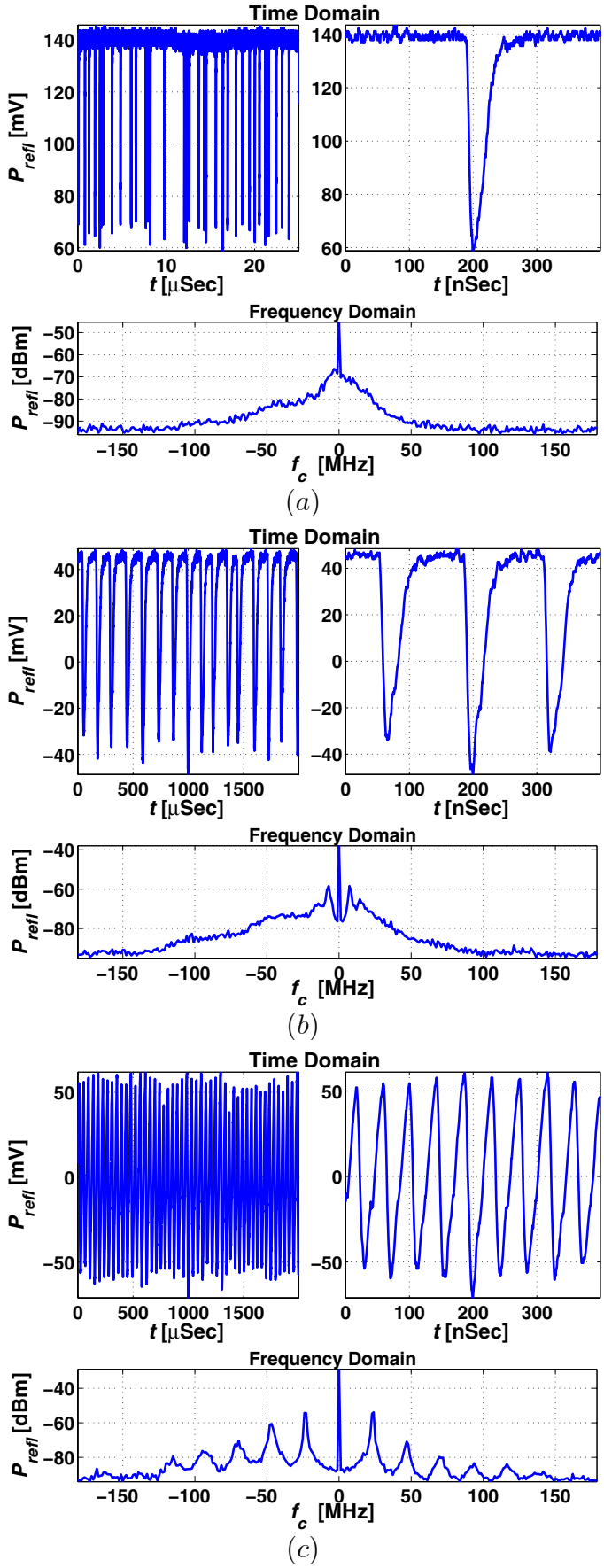

Figure 4.15: Reflected power as a function of time, at three different states of the resonator, (a) SM threshold, (b) regular oscillations, and (c) high frequency regular oscillations. Each panel has three subplots. The upper two subplots show the reflected power as a function of time. The lower subplot shows the reflected power in the frequency domain.

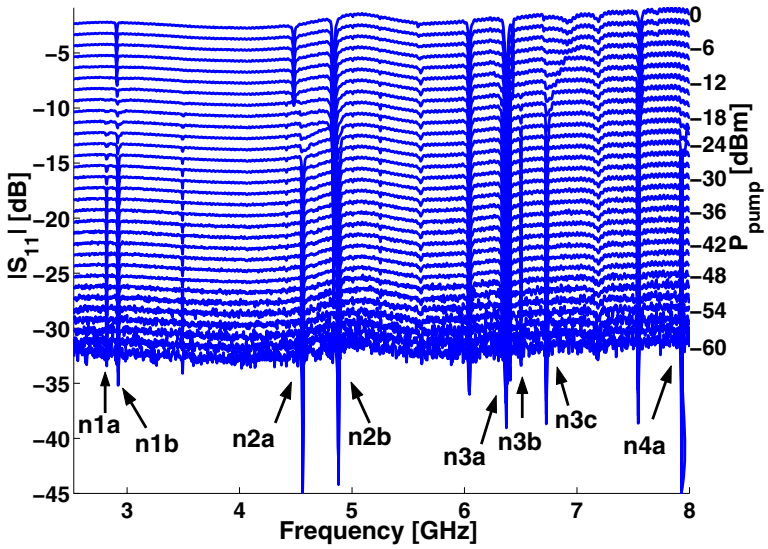

Figure 4.16: Several $|S_{11}|$ measurement of E13 resonator, as a function of frequency, in the vicinity of the third resonance frequency. The measurements, shifted vertically for clarity, are obtained for increasing input powers.

original location, as similar to the behavior measured at E16. At present we don't have an explanation for the multiplicity of the resonance modes. The different in the modes behavior might results from different coupling strengths of the modes to the HED. HFSM was measured at all marked resonance modes in experiments followed the first cooldown cycle. In experiments followed additional cooldown cycles, HFSM was not measured at $n3x$ resonance modes, and instead they experienced a threshold power at which the $|S_{11}|$ was abruptly increased. The origin for this change is yet unclear.

E13 experiences noncontinuous noise amplification at threshold power. Fig. 4.17 plots a high resolution 3DFV of the reflected power P_{refl}, in a frequency band of 1 GHz around $n4a$ resonance, as a function of the pump power P_{pump}, while the resonator is stimulated with a CW signal at frequency $f = f_4$. $f_c = f - f_4$ is the centered span frequency around the resonance frequency. This measurement shows the dependence of the HFSM on the pump power over a broadband frequency range. The frequencies marked as SS1, SS2 are probably self-stimulated resonance modes, a term that would be explained in section 5.2. The threshold power, at which the HFSM starts, is hard to determined. First, the frequency response around the resonance frequency is not symmetric. Second, the chaotic-like behavior, characterizing the threshold power behavior, is not observed. Third and most important, at low powers the HFSM can only be observed at frequencies far from the resonance frequency, about 50 MHz at each direction. The HFSM are observed in the vicinity of the resonance frequency only after an additional increase of approximately 0.5dBm in the pump power. This behavior is robust in this resonance mode and repeats for various pump frequencies, at that mode.

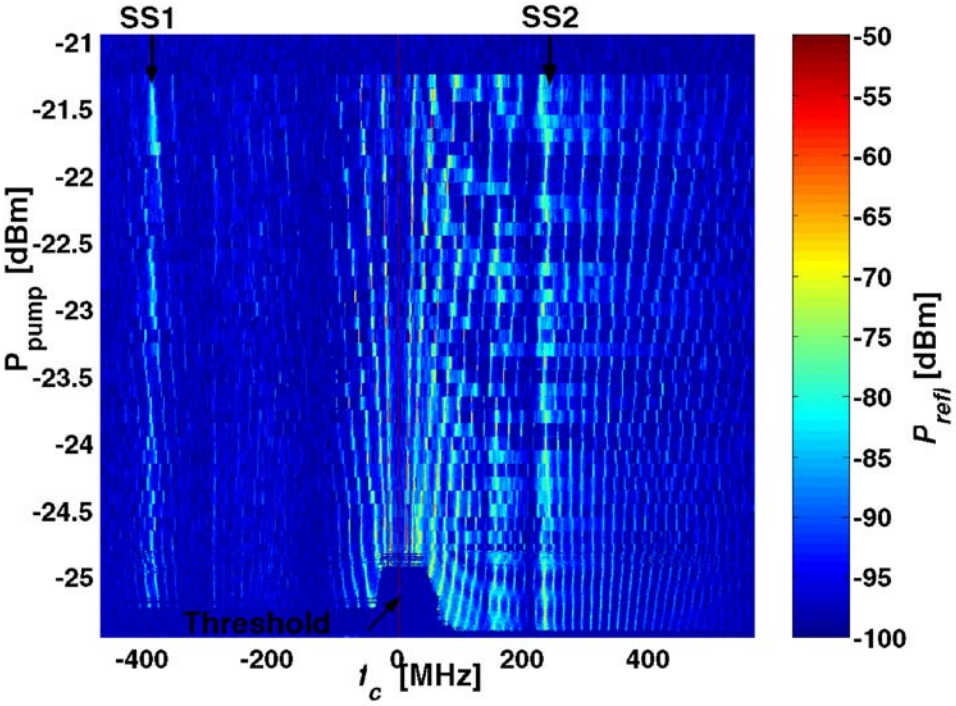

Figure 4.17: 3DFV of the reflected power P_{refl}, in a frequency band of 1 GHz around $n4a$ resonance, as a function of the pump power P_{pump}.

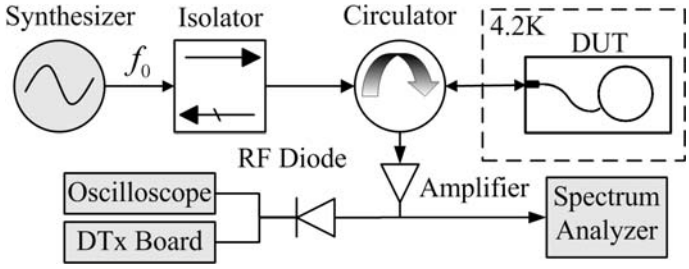

Figure 4.18: Setup used for LFSO reflection measurements.

4.4 Low Frequency Self-Sustained Oscillations

4.4.1 Introduction

The previous sections describe the SM phenomena in an incomplete way. This section enhances the description of the HFSM and describes another aspect of the phenomena, which regards self-sustained oscillations at much lower frequencies. The frequency of the LFSO ranges between $10 - 0.01\,\mathrm{Hz}$. The LFSO are measured at all devices, at various resonance frequencies and are robust phenomena in our resonators.

There are several time scales at which LFSO are observed. The most common are LFSO which have a frequency of several Hz, and would be referred to as type one LFSO or simply LFSO1. The LFSO1 are correlated to the high frequency HFSM, through their dependence on the pump power. They start at a slightly higher pump power than the HFSM threshold power, and oscillate concurrently with the HFSM. At the second threshold power, at which the HFSM ends, the LFSO amplitude is significantly decreased, but nevertheless they continue to oscillate. A second kind of LFSO, referred to as LFSO2, occurs at a lower pump power range than the LFSO1, and ends or becomes negligible as the LFSO1 begin. The LFSO2 has a longer period of a few seconds, different lineshape, and is less regular than the LFSO1. A third kind of LFSO, referred to as LFSO3, has an even longer period of a few tenth of seconds. It occurs concurrently to the LFSO1 and has a step-like shape, on which the LFSO1 rides. Due to its long period, it was only thoroughly measured in E15, but hints of its existence were also measured in E13.

The LFSO is best viewed in E13 and E15, where in E13 the LFSO are best coupled to the HFSM. In this chapter we show comprehensive data collected in E13, and E15. E16 also experiences LFSO, but due to the low power at which nonlinear effects occur in E16, their time domain measurements tend to be noisy.

The experiment setup used for the LFSO measurement is similar to the one used for the HFSM measurements and is depicted in Fig. 4.18. The resonator is stimulated by a CW pump signal and the amplified reflected power is measured by three instruments. The first is the SA, set to 'zero span' option, in which a time domain measurement of a limited frequency band is performed. This measurement has the advantage of being least noisy, but it has a sampling depth of only 8192 data points. The second is a OSC which has a sampling depth of 50 K data points, but the measurement is more noisy due to noises introduced by the preamplifiers. The third is a DTx,

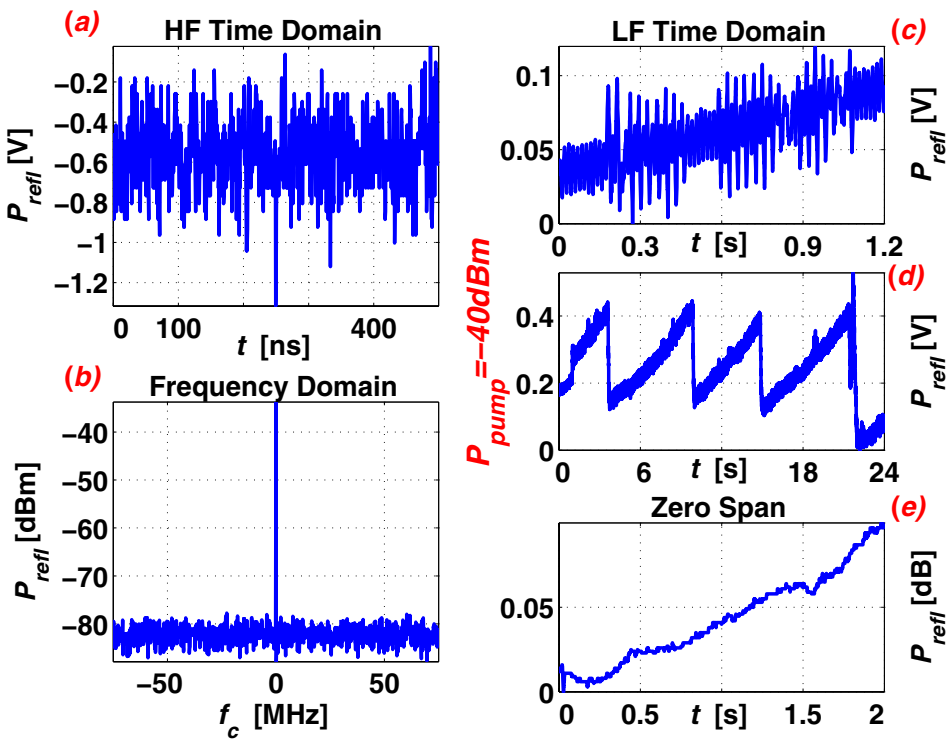

Figure 4.19: LFSO measurement, showing LFSO2. (a) and (b), aimed at measuring the HFSM, show the reflected power as a function of time and frequency, respectively. $(c) - (e)$, aimed at measuring the LFSO, show the reflected power as a function of time, where (c), (d) are taken using the OSC, and differ in time frame, and (e) is taken using the SA, zero-span option, and serves as an independent measurement. All measurements are AC coupled, or normalized.

which has unlimited sampling depth, but is the most noisy. Common noise in these measurements are the 50 Hz and 100 Hz line frequencies.

4.4.2 Low Frequency Self-Oscillation Characterization

Self-Oscillation Characterization at E13

Figures 4.19 - 4.23 show typical measurements, taken at E13, at which LFSO are observed. The pump frequency is set to the $n2a$ resonance, where each figure refers to a different pump power, and thus a different state of the resonator. Each figure has five subplots, marked $(a) - (e)$. Subplots (a) and (b), aimed at measuring the HFSM, show the reflected power as a function of time and frequency, respectively, and are taken using the OSC and SA, respectively. Subplots $(c) - (e)$, aimed at measuring the LFSO, show the reflected power as a function of time, where (c) and (d) are taken using the OSC, and differ in time frame, and (e) is taken using the SA, zero-span option, and serves as an independent measurement. All measurements are ac coupled, or normalized.

Fig. 4.19 shows a typical measurement of LFSO2. The pump power is set below the

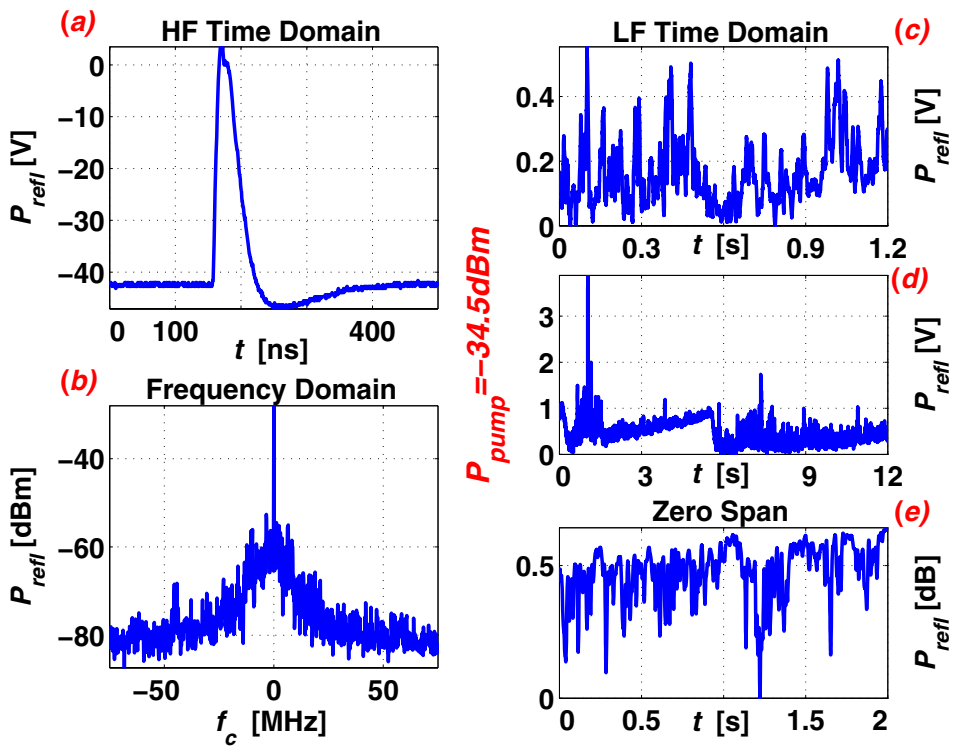

Figure 4.20: LFSO measurement, showing LFSO1 at threshold power. (a) and (b), aimed at measuring the HFSM, show the reflected power as a function of time and frequency, respectively. $(c) - (e)$, aimed at measuring the LFSO, show the reflected power as a function of time, where (c), (d) are taken using the OSC, and differ in time frame, and (e) is taken using the SA, zero-span option, and serves as an independent measurement. All measurements are AC coupled, or normalized.

HFSM threshold power so no oscillations are observed in (a) and (b). The LFSO2 are observed at (d), where oscillations with a right-angled triangle shape, and frequency of approximately 6 s, are observed. The cycles' lineshape and period time slightly differ from period to period, and in any case, do not fit any expected behavior. The measurement in (e) supports the ruling that this type of oscillations is not an artifact of the measurement equipment.

Fig. 4.20 shows a measurement of LFSO1 at its threshold power. The pump power is set to the HFSM threshold power so a single oscillation is observed in (a) and a broadband amplification in (b). The threshold region of the LFSO1 found expression in the time domain as unregulated oscillations, both in shape and time phase, which resembles noise. (d) shows that this so called noise, rides on the LFSO2, but can have a much larger amplitude.

Fig. 4.21 shows a measurement, in which regular LFSO1 are observed. The pump power is set to the regular HFSM power range. HFSM are observed in (a) and (b) in the time and frequency domains, respectively. LFSO1, which start at a slightly higher threshold power than the HFSM, and have a cycle time of approximately 3.25 s, are observed in $(c) - (e)$. Both (c) and (e), taken by two independent instruments, show

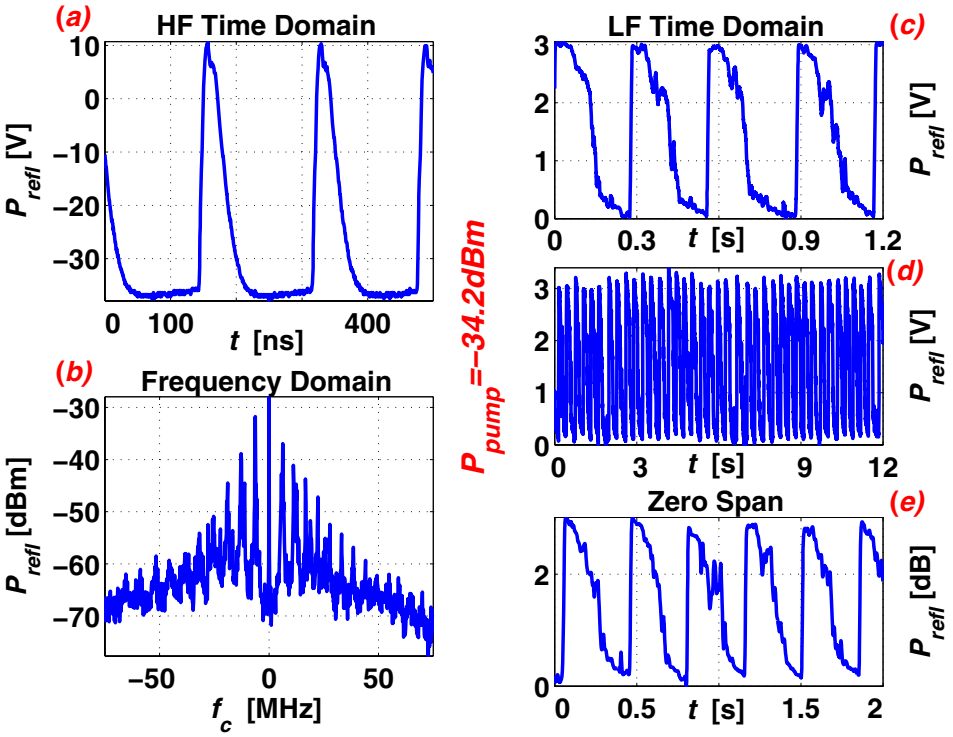

Figure 4.21: LFSO measurement, showing regular LFSO1. (a) and (b), aimed at measuring the HFSM, show the reflected power as a function of time and frequency, respectively. $(c) - (e)$, aimed at measuring the LFSO, show the reflected power as a function of time, where (c), (d) are taken using the OSC, and differ in time frame, and (e) is taken using the SA, zero-span option, and serves as an independent measurement. All measurements are AC coupled, or normalized.

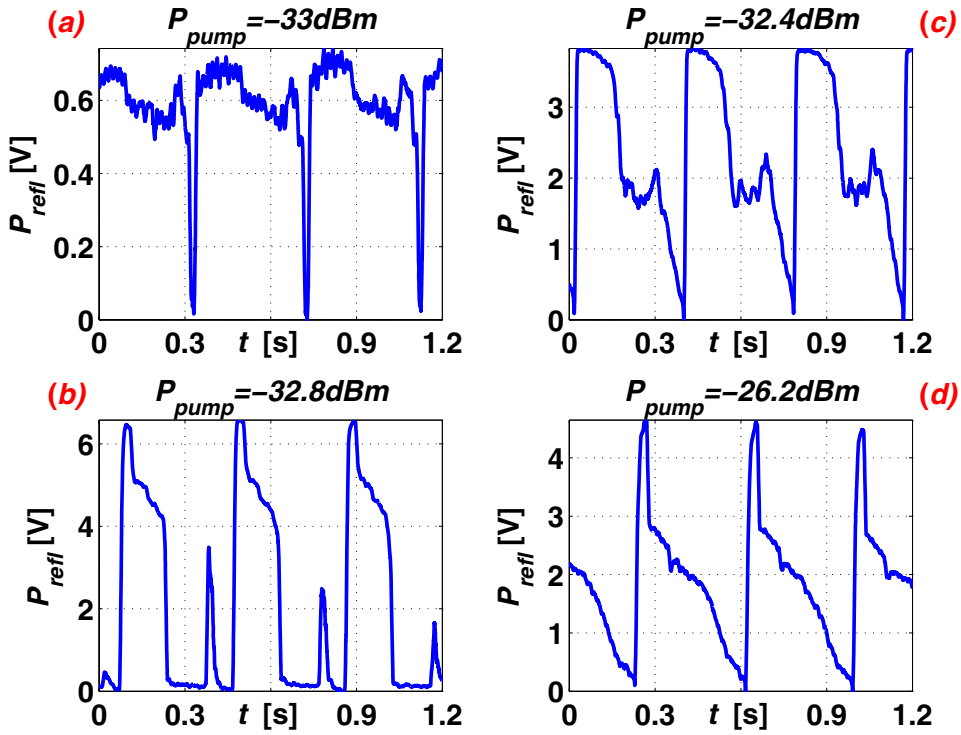

Figure 4.22: LFSO measurement, showing regular LFSO1. (a) - (d) show the normalized reflected power as a function of time, for different values of pump power.

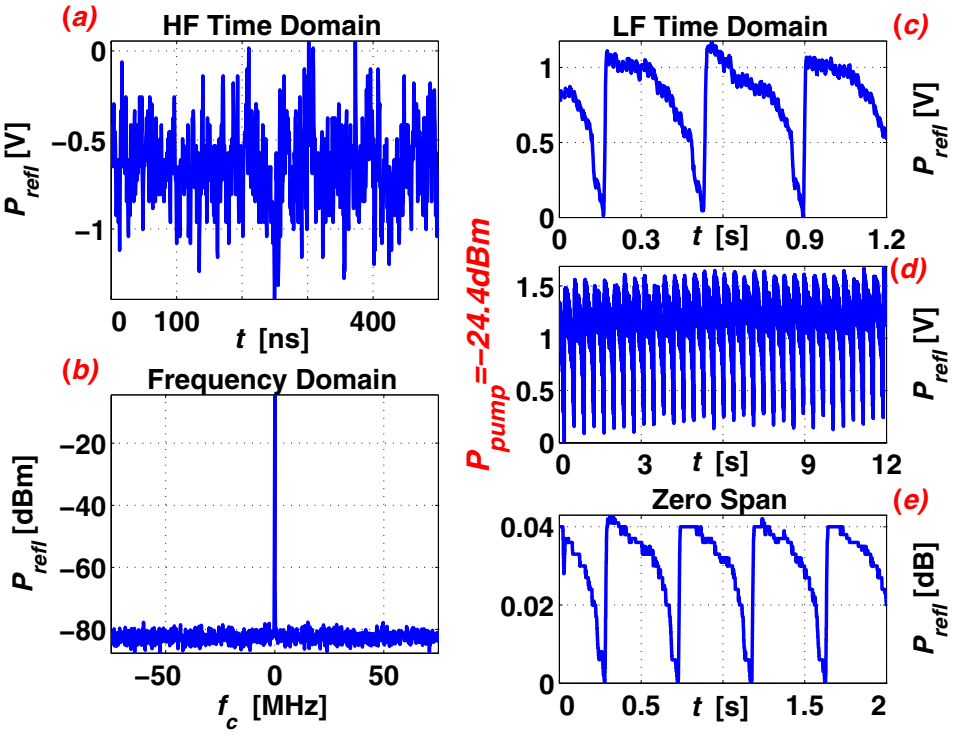

Figure 4.23: LFSO measurement, showing regular LFSO1, without HFSM. (a) and (b), aimed at measuring the HFSM, show the reflected power as a function of time and frequency, respectively. $(c) - (e)$, aimed at measuring the LFSO, show the reflected power as a function of time, where (c), (d) are taken using the OSC, and differ in time frame, and (e) is taken using the SA, zero-span option, and serves as an independent measurement. All measurements are AC coupled, or normalized.

similar LFSO line shapes, which, in general, is composed of a sharp increase in the reflected power, followed by a relaxation decrease, but changes as the pump power changes. Several more LFSO lineshape, taken at different pump powers are observed in Fig. 4.22. All line shapes resembles relaxation behavior, but have nonnegligible differences between them. The theoretical model suggests that this difference may results from different time periods, that the system spends in the intermediate way between the SC and the NC states. This time period is very sensitive to the mode amplitude in the resonator, the resonance shift, and the loss factor in the bridge. Similar line-shapes were reported in [27], but in a non resonant system, and different time scale.

Fig. 4.23 shows a measurement is which regular LFSO1 are observed, but the pump power is set above the 2nd HFSM threshold power, so no HFSM occurs. The amplitude of the LFSO is decreased significantly as the HFSM ends, but no additional changes in their lineshape or time period occur. In this measurement no threshold power, in which the LFSO ends, is observed.

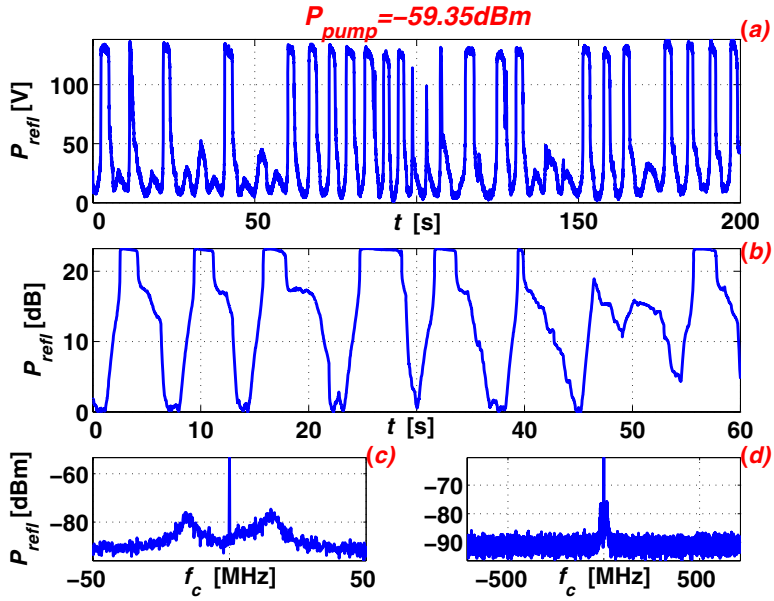

Figure 4.24: LFSO2 measurement. Subplots (a) and (b) show LFSO2 in the normalized reflected power, as a function of time, taken using the OSC, and SA, respectively. (c) and (d), show the reflected power as a function frequency.

Self-Oscillation Characterization at E15

Figures 4.24 - 4.24 show typical measurements, taken at E15, in which LFSO of various time scales are observed. The pump frequency is set to the $n3$ resonance, where each figure refers to a different pump power, and thus a different state of the resonator. Each figure has four subplots, marked $(a) - (d)$ or alternatively $(I) - (IV)$. Subplots (a) and (b) , aimed at measuring the LFSO, and show the reflected power as a function of time, where (a) is taken using the OSC, and (b) is taken using the SA, zero-span option. Subplots (c) and (d), show the reflected power as a function frequency, at different frequency bands of 100 MHz and 1.4 GHz respectively, for comparison. All measurements are ac coupled, or normalized.

Fig. 4.24 shows a LFSO measurement, in which the pump power is set to a relatively low power, and the resonator experiences low-power HFSM of $n3^*$ resonance, as explained in 4.3.1. LFSO2 with a time period of approximately 6 s, and respectively large amplitude, are measured, as shown in subplots (a) and (b). Their lineshape is moderately repetitive, and cycle time is moderately stable.

Fig. 4.25 shows a similar LFSO measurement, in which the pump power is set to a relatively low power, but the resonator does not experiences low-power HFSM of $n3^*$ resonance. The time period of the LFSO2 is approximately 7 s. Subplots (a) and (b) show, that the LFSO have a much smaller amplitude than the one measured during the low power HFSM. Again, their lineshape is moderately repetitive, and cycle time is moderately stable.

Fig. 4.26 shows a LFSO measurement, in which the pump power is set slightly below the threshold of the HFSM. The measurements used for subplots (a) and (b)

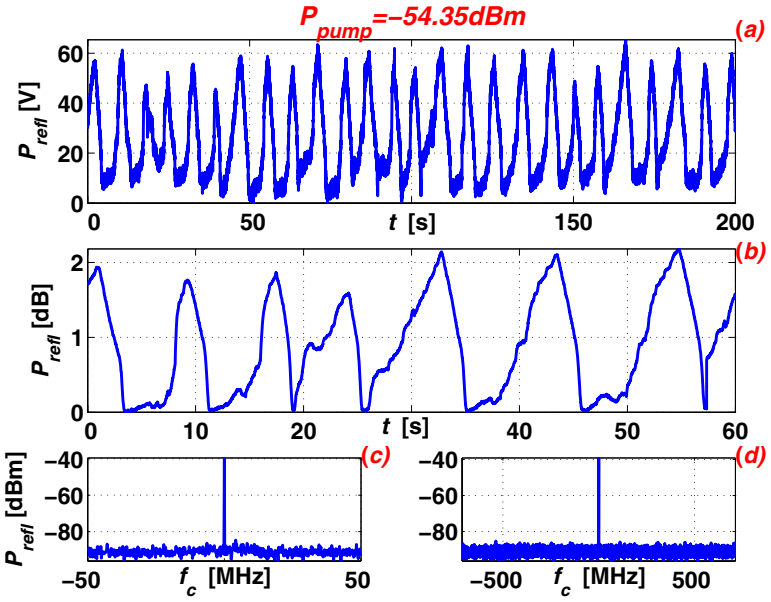

Figure 4.25: LFSO2 measurements, where no HFSM occur. Subplots (a) and (b) show LFSO2 of the normalized reflected power as a function of time, taken using the OSC, and SA, respectively. (c) and (d) show the reflected power as a function frequency.

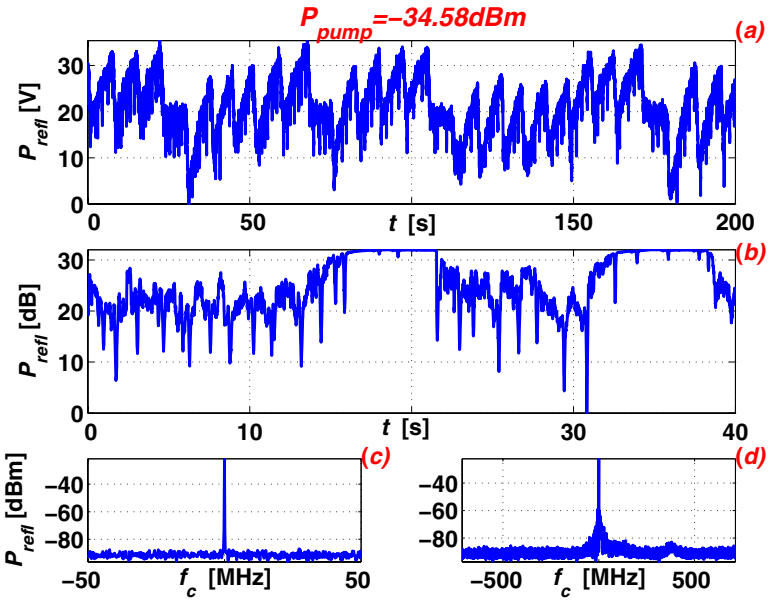

Figure 4.26: LFSO2 & traces of LFSO3 measurement. Subplots (a) and (b) show LFSO2 of the normalized reflected power as a function of time, taken using the OSC, and SA, respectively. (c) and (d) show the reflected power as a function frequency.

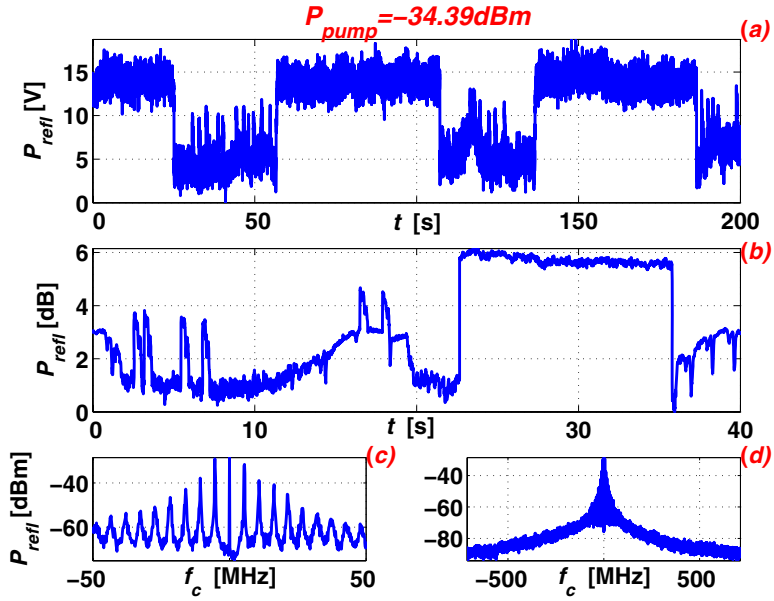

Figure 4.27: LFSO3 & traces of LFSO2 measurement. Subplots (a) and (b) show LFSO3 of the normalized reflected power as a function of time, taken using the OSC, and SA, respectively. (c) and (d) show the reflected power as a function frequency.

were not taken simultaneously, and as so, they show a slightly different observation of the oscillations at that range. LFSO2 are clearly seen in (a), it has a time period of approximately 6.5 s, and saw like shape. In additions, occurring at a rather larger time scan, one can observe dips or the reflected powers. These are hints for an even slower time scale, that exist in the resonator. LFSO2 are also observed in (b), but experiences a less repetitive lineshape, and higher frequency. Again traces of a longer time scale oscillations is observed.

Fig. 4.27 shows a LFSO measurement, in which the resonator concurrently experiences HFSM. A new type of LFSO, referred to as LFSO3, that has a large time scale of around 82 s, with unequal duty cycle, and step like shape, are observed. The resonator is set to the threshold of these oscillations. Looking at (b) one sees, that when the resonator is in the low reflection state its behavior resembles the one shown in Fig. 4.27, for lower pump powers. When the resonator is in the high reflection state LFSO2 can be seen in (a) but not in (b). Looking at the broadband frequency response (d) one notes the large broadband frequency range, to which the HFSM sidebands spread.

Fig. 4.28(a) shows a LFSO measurement, in which the resonator concurrently experiences HFSM. Nice and clear LFSO3, with a slightly shorter time scale of approximately 78 s, are observed. In addition, LFSO1, which have an average frequency of 1.5 Hz, appear when the resonator is in the low reflection state. Fig. 4.28(b) magnifies the LFSO1 seen at Fig. 4.28(a, II) into two time frames. The lineshape, as seen in subplot II, follows a typical relaxation pattern. The evolution of the oscillations in time (subplot I), is governed by the coupling of the LFSO1 and the slower LFSO3

oscillations. After a few tenth of LFSO1 cycles, they start to decay, where there is no observed clue for an external, or internal perturbation, that triggered this behavior. They decay both in amplitude and in cycle time, up to the point, where no oscillations are observed, and then, after a final drop of the reflection power, the low reflection period of the LFSO3 ends. Looking at the broadband frequency response (III), one notes the large broadband frequency range, to which the HFSM sidebands spread.

Fig. 4.29(a) shows a LFSO measurement, in which the resonator is set above the HFSM power range, and to the second threshold of the LFSO1. In general, as the pump power is increased, the amplitude of the LFSO gets smaller (in dB units), and their frequency increases. The second LFSO1 threshold power is characterized by a relatively sharp drop in the oscillation amplitude, as can be seen in both subplots (I) and (II). Apart for this behavior, no other changes occur, and the oscillations maintain their lineshape, as can be also seen in Fig. 4.29(b), which was taken for an higher pump power.

4.4.3 Discussion

The presence of LFSO concurrently to the HFSM is not as surprising as one might think. The reported oscillation frequency, for the case of a SC microbridge driven by external voltage or current, ranges between several Hz [29] and up to several MHz [27]. Gurevich *et. al.* describes several hotspot mechanism, that results different time scales. Mechanisms such as formation and destruction of an hotspot, vibrations of the size of the hotspot's perimeter, drifting of the hotspot along the bridge, may all concurrently exist and result various thermal time scales in the devices. In addition, different thermal coupling of the NbN to the Sapphire substrate and the AlN might exist. Another possible explanation is interaction between two or more hotspots that produces more that one time scale. At the current state of the research we can not proof nor contradict any of these suggestions.

Much effort has been put to measure and characterize the LFSO as well to find the correlations between these oscillations and the high-frequency HFSM. The LFSO of types one and three have threshold power, which is correlated to the HFSM threshold power, and both roughly start at the same power. In addition the LFSO experiences a change in their lineshape in the threshold power, at which the HFSM ends, but not power was measured, at which they completely end. No correlation between the LFSO2 and the HFSM is observed.

4.4.4 Summary

Three types of low-frequency self-sustained oscillations are observed. LFSO with a frequency of a few Hz exist concurrently, and coupled to LFSO with a time period of tenth of seconds. Both are correlated to the high frequency self-modulations. In addition, LFSO, with a time period of several second, are observed at lower pump power frequencies, and are probably not correlated to thee HFSM.

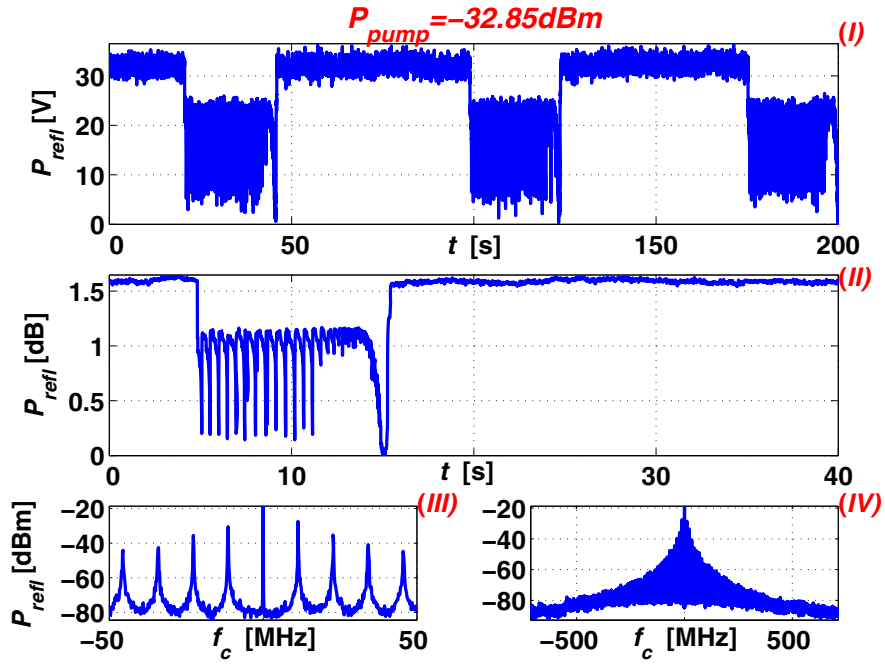

(a)

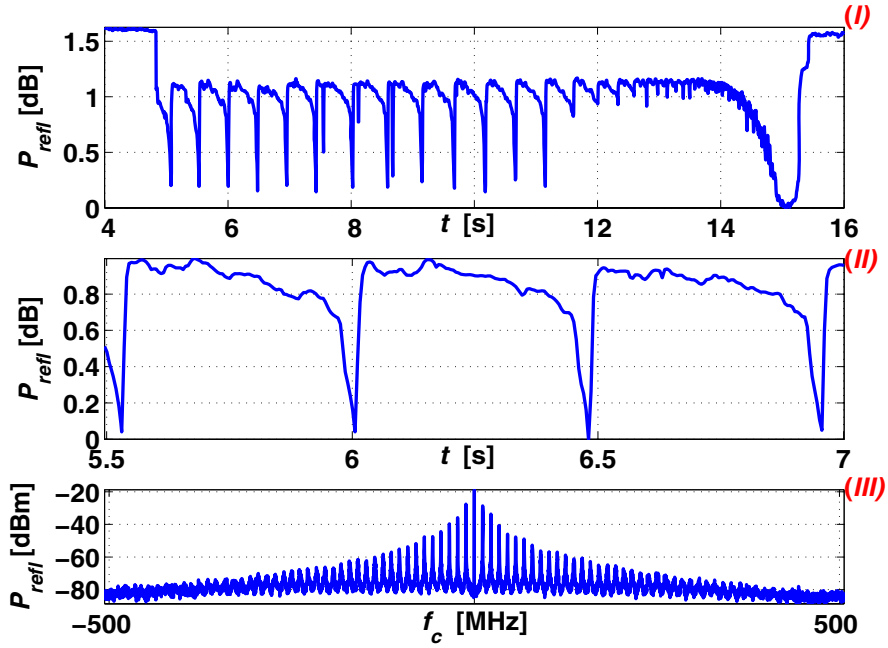

(b)

Figure 4.28: LFSO1 coupled to LFSO3 measurement. Panel (a) has four subplots. Subplots (I) and (II) show the normalized reflected power as a function of time, taken using the OSC, and SA, respectively. LFSO1 coupled to LFSO3 are observed. (III) and (IV) show the reflected power as a function frequency.Panel (b) magnifies two smaller time frames of the LFSO trace seen at panel (a), subplot II

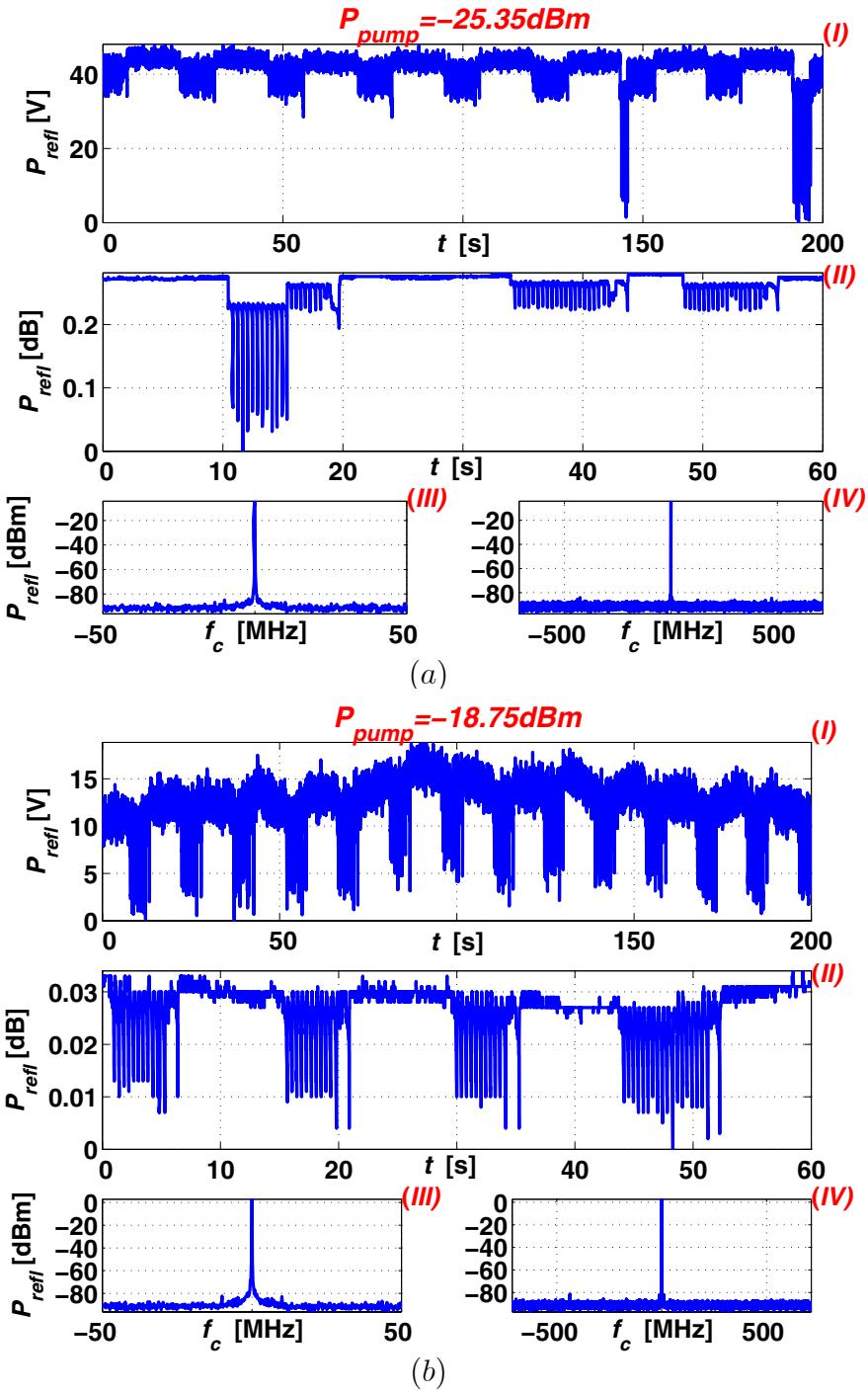

Figure 4.29: LFSO1 coupled to LFSO3 measurement. Each Panel has four subplots. Subplots (I) and (II) show the normalized reflected power as a function of time, taken using the OSC, and SA, respectively. (III) and (IV) show the reflected power as a function frequency.

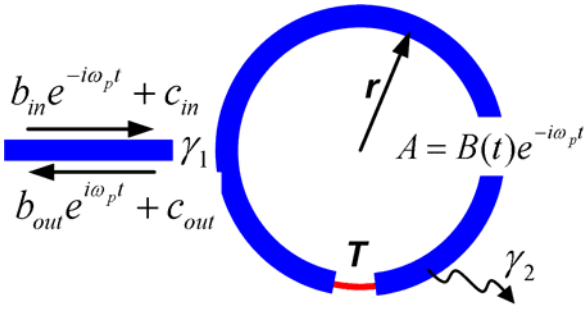

Figure 4.30: Resonator model, coupled to a test port and a linear dissipation port.

4.5 Theoretical Model

To account for our findings we propose a theoretical model according to which the self-sustained oscillations are originated by thermal instability in the meander strip. The model is based on the coupling between the equation of motion of the mode amplitude in the resonator and thermal balance equation in the meander strip. A comparison of the model's predictions with experimental results, taken for the HFSM, yields a partial qualitative agreement. The model is presently still being developed. The outcome is still not final and we present here the best results achieved so far.

4.5.1 Steady State Solutions

Equation of Motion of the Mode Amplitude

Fig. 4.30 plots the resonator model, in which the resonator couples to a test port and a linear dissipation port. The resonator is driven by a coherent tone $b^{in}e^{-i\omega_p t}$ injected into the test port, which is weakly coupled to the resonator, where b^{in} is a constant complex amplitude and ω_p is the driven angular frequency. The mode amplitude A is written as $A = Be^{-i\omega_p t}$, where $B(t)$ is a complex amplitude, which is assumed to vary slowly on a time scale of $1/\omega_p$. In this approximation, the equation of motion of B reads [59]

$$\frac{dB}{dt} = \left[i\left(\omega_p - \omega_0\right) - \gamma\right] B - i\sqrt{2\gamma_1}b^{in} + c^{in}, \tag{4.1}$$

where ω_0 is the angular resonance frequency, $\gamma = \gamma_1 + \gamma_1$, where γ_1 is the coupling constant between the resonator and the test port, and γ_2 is the damping rate of the mode. The term c^{in} represents input noise with random phase

$$\langle c^{in}\rangle = 0, \tag{4.2}$$

$$\langle c^{in}(t)c^{in}(t')\rangle = \langle c^{in*}(t)c^{in*}(t')\rangle = 0, \tag{4.3}$$

and correlation function given by

$$\langle c^{in}(t)c^{in*}(t')\rangle = G\omega_0\delta\left(t - t'\right). \tag{4.4}$$

In thermal equilibrium, and for the case of high temperature $k_B T >> \hbar\omega_0$, where k_B is Boltzmann's constant, one has

$$G = \frac{2\gamma}{\omega_0}\frac{k_B T}{\hbar\omega_0}. \tag{4.5}$$

The steady state solution of Eq. 4.1 is denoted as

$$B_\infty = \frac{i\sqrt{2\gamma_1}b^{in}}{i\left(\omega_p - \omega_0\right) - \gamma}. \tag{4.6}$$

In terms of the dimensionless time $\tau = \omega_0 t$ Eq. 4.1 reads

$$\frac{db}{d\tau} + \lambda b = \frac{c^{in}}{\omega_0}, \tag{4.7}$$

where

$$b = B - B_\infty, \tag{4.8}$$

$$\lambda = \frac{\gamma - i\left(\omega_p - \omega_0\right)}{\omega_0}. \tag{4.9}$$

The output signal a^{out} reflected off the resonator is written as $a^{out} = b^{out}e^{-i\omega_p t}$. The input-output relation, relating the output signal to the input signal [21], is given by

$$\frac{b^{out}}{\sqrt{\omega_0}} = \frac{b^{in}}{\sqrt{\omega_0}} - i\sqrt{\frac{2\gamma_1}{\omega_0}}B. \tag{4.10}$$

The total power dissipated in the resonator Q_t is given by

$$Q_t = \hbar\omega_0 2\gamma_2 \left|B\right|^2. \tag{4.11}$$

Thermal Balance Equation

Consider the case where the nonlinearity is originated by a local hotspot in the stripline resonator. If the hotspot is assumed to be sufficiently small, its temperature T can be considered as homogeneous. The temperature of other parts of the resonator is assumed be equal to that of the coolant T_0. The power Q heating up the hotspot is given by $Q = \alpha Q_t$ where $0 \leqslant \alpha \leqslant 1$. The heat balance equation reads

$$C\frac{dT}{dt} = Q - W, \tag{4.12}$$

where C is the thermal heat capacity, $W = H\left(T - T_0\right)$ is the power of heat transfer to the coolant, and H the heat transfer coefficient. In terms of the dimensionless time τ and the dimensionless temperature

$$\Theta = \frac{T - T_0}{T_c - T_0}, \tag{4.13}$$

Eq. 4.12 reads

$$\frac{d\Theta}{d\tau} + g\left(\Theta - \Theta_\infty\right) = 0, \tag{4.14}$$

where

$$g = \frac{H}{C\omega_0}, \tag{4.15}$$

$$\Theta_\infty = \frac{2\hbar\alpha\gamma_2 \left|B\right|^2}{gC\left(T_c - T_0\right)} = \frac{2\alpha\gamma_2\rho E}{\omega_0 g}, \tag{4.16}$$

$$\rho = \frac{\hbar\omega_0}{C\left(T_c - T_0\right)}. \tag{4.17}$$

The steady states solution of 4.14, where $B = B_\infty$ is given by

$$\Theta_{\infty 0} = \frac{2\hbar\alpha\gamma_2 \left|B_\infty\right|^2}{gC\left(T_c - T_0\right)} = \frac{2\alpha\gamma_2\rho \left|B_\infty\right|^2}{\omega_0 g}. \tag{4.18}$$

Considering the fluctuation of B around B_∞ as small, one has to first order

$$\Theta_\infty = \Theta_{\infty 0}\left[1 + \frac{b}{B_\infty} + \left(\frac{b}{B_\infty}\right)^*\right]. \tag{4.19}$$

Thus Eq. 4.14 can be written as

$$\frac{d\theta}{d\tau} + g\theta = f \tag{4.20}$$

where

$$\theta = \Theta - \Theta_{\infty 0}, \tag{4.21}$$

$$f = g\Theta_{\infty 0}\left[\frac{b}{B_\infty} + \left(\frac{b}{B_\infty}\right)^*\right]. \tag{4.22}$$

In general, the reflection coefficient r, in steady state, is giving by

$$r = \frac{b^{out}}{b^{in}} = \frac{\gamma_2 - \gamma_1 - i\left(\omega_p - \omega_0\right)}{\gamma_2 + \gamma_1 - i\left(\omega_p - \omega_0\right)}. \tag{4.23}$$

The resonance frequency ω_0, γ_1 and α are assumed to have a step function dependence on the temperature and the damping rate γ_2, is assumed to increase substantially when the temperature is close the critical one

$$\begin{aligned} \omega_0 &= \begin{cases} \omega_{0s} & \Theta < 1 \\ \omega_{0n} & \Theta > 1 \end{cases}, \quad \gamma_1 = \begin{cases} \gamma_{1s} & \Theta < 1 \\ \gamma_{1n} & \Theta > 1 \end{cases}, \\ \alpha &= \begin{cases} \alpha_s & \Theta < 1 \\ \alpha_n & \Theta > 1 \end{cases}, \quad \gamma_2 = \begin{cases} \gamma_{2s} & \Theta < 1 \\ \gamma_{2high} & \Theta \cong 1 \\ \gamma_{2n} & \Theta > 1 \end{cases}. \end{aligned} \tag{4.24}$$

In general, disregarding noise, the coupled equations 4.7 and 4.14 may have up

to two different steady state solutions. A SC steady state exists when $\Theta_{\infty 0} < 1$, or when $E < E_s$, where $E_s = gC\left(T_c - T_0\right)/2\alpha_s\gamma_{2s}\hbar$. Similarly, a NC steady state exists when $\Theta_{\infty 0} > 1$, or when $E > E_n$, where $E_n = gC\left(T_c - T_0\right)/2\alpha_n\gamma_{2n}\hbar$.

4.5.2 Fluctuation

The solution of 4.7 is given by

$$B\left(\tau\right) = B_\infty + \left[B\left(0\right) - B_\infty\right]\exp\left(-\lambda\tau\right) + \frac{1}{\omega_0}\int_0^\tau c^{in}\left(\tau'\right)\exp\left[-\lambda\left(\tau - \tau'\right)\right]d\tau' \quad (4.25)$$

The expectation value of $B\left(\tau\right)$ is given by

$$\left\langle B\left(\tau\right)\right\rangle = B_\infty + \left[B\left(0\right) - B_\infty\right]\exp\left(-\lambda\tau\right). \quad (4.26)$$

The variance is given by

$$\begin{aligned}\left\langle\left|\Delta B\right|^2\right\rangle &= \left\langle\left|B - \left\langle B\left(\tau\right)\right\rangle\right|^2\right\rangle \quad (4.27)\\ &= \frac{1}{\omega_0^2}\exp\left(-\frac{2\gamma\tau}{\omega_0}\right)\int_0^\tau d\tau'\int_0^\tau d\tau''\exp\left[\frac{i\left(\omega_p - \omega_0\right)\left(\tau' - \tau''\right)}{\omega_0}\right]\times\\ &\times\exp\left[\frac{\gamma\left(\tau' + \tau''\right)}{\omega_0}\right]\left\langle c^{in*}\left(\tau'\right)c^{in}\left(\tau''\right)\right\rangle. \quad (4.28)\end{aligned}$$

Using Eq. 4.4

$$\begin{aligned}\left\langle\left|\Delta B\right|^2\right\rangle &= \frac{G}{\omega_0}\exp\left(-\frac{2\gamma\tau}{\omega_0}\right)\int_0^\tau d\tau'\exp\left[\frac{2\gamma\tau'}{\omega_0}\right]\\ &= \frac{G}{2\gamma}\left[1 - \exp\left(-\frac{2\gamma\tau}{\omega_0}\right)\right]. \quad (4.29)\end{aligned}$$

4.5.3 Evolution between transitions

In general, the solution of Eq. 4.14 is given by

$$\Theta\left(\tau\right) = \Theta\left(0\right)\exp\left(-g\tau\right) + g\int_0^\tau \Theta_\infty\left(\tau'\right)\exp\left[g\left(\tau' - \tau\right)\right]d\tau'. \quad (4.30)$$

Assume the case where $\Theta \neq 1$ in the time interval $(0, \tau)$. Disregarding noise, the solution of Eq. 4.7 is given by

$$B\left(\tau\right) = B_\infty\left[1 + \frac{B\left(0\right) - B_\infty}{B_\infty}\exp\left(-\lambda\tau\right)\right], \quad (4.31)$$

thus using the notation

$$\beta = \frac{B\left(0\right) - B_\infty}{B_\infty}, \quad (4.32)$$

$$\Theta_{\infty 0} = \frac{2\alpha\gamma_2\rho\left|B_\infty\right|^2}{\omega_0 g}, \tag{4.33}$$

one has

$$\Theta_\infty(\tau') = \Theta_{\infty 0}\left[1 + \beta\exp(-\lambda\tau') + \beta^*\exp(-\lambda^*\tau') + |\beta|^2\exp\left[-(\lambda+\lambda^*)\tau'\right]\right]. \tag{4.34}$$

Therefore using the identity

$$\int_0^\tau \exp(a\tau')\,d\tau' = \frac{e^{a\tau}-1}{a} \tag{4.35}$$

one finds

$$\Theta(\tau) = \exp(-g\tau)\,\Theta(0) + \\ +g\Theta_{\infty 0}\exp(-g\tau)\left(\frac{e^{g\tau}-1}{g} + \beta\frac{e^{(g-\lambda)\tau}-1}{g-\lambda} + \beta^*\frac{e^{(g-\lambda^*)\tau}-1}{g-\lambda^*} + |\beta|^2\frac{e^{(g-\lambda-\lambda^*)\tau}-1}{g-\lambda-\lambda^*}\right). \tag{4.36}$$

Adiabatic Case

In this limit $\gamma/g\omega_0 \ll 1$. To estimate the value of this parameter in our samples, consider the case were nonlinearity is originated by a hotspot of lateral area A, forming in the meander strip. Let d be the thickness of the NbN film. The heat capacity C of the hotspot is given by $C = C_v A d$, where C_v is the heat capacity per unit volume. Moreover, we assume the substrate to be isothermal and that the hotspot is dissipated mainly down into the substrate rather than along the film [30]. In this case the heat transfer coefficient H can be expressed as $H = A\alpha$, where α is the heat transfer coefficient per unit area. These parameters at temperature $T = 4.2\,\mathrm{K}$ are estimated for NbN on Sapphire substrate in [30], $C_v \simeq 0.8\times10^{-3}\,\mathrm{J\,cm^{-3}\,K^{-1}}$ and $\alpha \simeq 16\,\mathrm{W\,cm^{-2}\,K^{-1}}$, yielding

$$g = \frac{H}{C\omega_0} = \frac{\alpha}{2\pi C_v d f_0} = 3.2\left(\frac{d}{10\,\mathrm{nm}}\right)^{-1}\left(\frac{f_0}{1\,\mathrm{GHz}}\right)^{-1}, \tag{4.37}$$

where f_0 is the resonance frequency. Using the material parameters as estimated in [50], $C_v \simeq 2.7\times10^{-3}\,\mathrm{J\,cm^{-3}\,K^{-1}}$ and $\alpha \simeq 1.5\,\mathrm{W\,cm^{-2}\,K^{-1}}$ leads to

$$g = 8.8\times10^{-2}\left(\frac{d}{10\,\mathrm{nm}}\right)^{-1}\left(\frac{f_0}{1\,\mathrm{GHz}}\right)^{-1}. \tag{4.38}$$

On the other hand the quality factor $\omega_0/\gamma \simeq 10^3$ in our resonators, thus $\gamma/g\omega_0 \simeq 10^{-3}$.

In the adiabatic case one expects that $\Theta(\tau) \simeq \Theta_\infty(\tau)$, thus it is convenient to rewrite Eq. 4.14 as

$$\frac{d\xi}{d\tau} + g\xi = -\frac{d\Theta_\infty}{d\tau}, \tag{4.39}$$

where ξ is

$$\xi(\tau) = \Theta(\tau) - \Theta_\infty(\tau). \tag{4.40}$$

Multiplying Eq. 4.39 by an integration factor

$$\frac{d}{d\tau}\left(\xi e^{g\tau}\right) = -e^{g\tau}\frac{d\Theta_\infty}{d\tau}, \tag{4.41}$$

leads to

$$\xi(\tau) = e^{-g\tau}\xi(0) - e^{-g\tau}\int_0^\tau e^{g\tau'}\frac{d\Theta_\infty(\tau')}{d\tau}d\tau'. \tag{4.42}$$

Using 4.34

$$\frac{d\Theta_\infty}{d\tau} = -\Theta_{\infty 0}\left[\lambda\beta e^{-\lambda\tau} + \lambda^*\beta^* e^{-\lambda^*\tau} + (\lambda+\lambda^*)|\beta|^2 e^{-(\lambda+\lambda^*)\tau}\right], \tag{4.43}$$

thus

$$\begin{aligned}\xi(\tau) &= e^{-g\tau}\xi(0) + e^{-g\tau}\Theta_{\infty 0}\int_0^\tau\left[\lambda\beta e^{(g-\lambda)\tau'} + \lambda^*\beta^* e^{(g-\lambda^*)\tau'} + (\lambda+\lambda^*)|\beta|^2 e^{(g-\lambda-\lambda^*)\tau'}\right]d\tau' \\ &= e^{-g\tau}\xi(0) + \\ &+ \Theta_{\infty 0}\left[\lambda\beta\frac{e^{-\lambda\tau}-e^{-g\tau}}{g-\lambda} + \lambda^*\beta^*\frac{e^{-\lambda^*\tau}-e^{-g\tau}}{g-\lambda^*} + (\lambda+\lambda^*)|\beta|^2\frac{e^{-(\lambda+\lambda^*)\tau}-e^{-g\tau}}{g-\lambda-\lambda^*}\right].\end{aligned} \tag{4.44}$$

In the adiabatic limit $g >> \operatorname{Re}\lambda = \gamma/\omega_0$. Using this and assuming $g\tau >> 1$ yield

$$\begin{aligned}\xi(\tau) &\simeq \frac{\Theta_{\infty 0}}{g}\left(\lambda\beta e^{-\lambda\tau} + \lambda^*\beta^* e^{-\lambda^*\tau} + (\lambda+\lambda^*)|\beta|^2 e^{-(\lambda+\lambda^*)\tau}\right) \\ &= -\frac{1}{g}\frac{d\Theta_\infty(\tau)}{d\tau},\end{aligned} \tag{4.45}$$

or

$$\Theta(\tau) = \Theta_\infty(\tau) - \frac{1}{g}\frac{d\Theta_\infty(\tau)}{d\tau}. \tag{4.46}$$

Thus, as $\Theta_\infty(\tau)$ is directly related to the mode amplitude through Eq. 4.16, this expression indicates that the temperature follows behind the mode amplitude.

Resonance Moreover, assume for simplicity the case of pump at resonance frequency, namely $\omega_p = \omega_0$. For this case B is pure imaginary and its time evolution is given by

$$\frac{B(t) - B_\infty}{B(0) - B_\infty} = \exp\left(-\frac{\gamma\tau}{\omega_0}\right), \tag{4.47}$$

where

$$B_\infty = -\frac{i\sqrt{2\gamma_1}b^{in}}{\gamma}. \tag{4.48}$$

Moreover, since in the present case β is real and $\lambda = \gamma/\omega_0$, one has

$$\Theta_\infty(\tau) = \Theta_{\infty 0}\left(1 + 2\beta e^{-\frac{\gamma\tau}{\omega_0}} + \beta^2 e^{-\frac{2\gamma\tau}{\omega_0}}\right), \tag{4.49}$$

$$\begin{aligned}\frac{d\Theta_\infty}{d\tau} &= -\frac{\gamma}{\omega_0}\Theta_{\infty 0}\left(2\beta e^{-\frac{\gamma\tau}{\omega_0}} + 2\beta^2 e^{-\frac{2\gamma\tau}{\omega_0}}\right) \\ &= \frac{\gamma}{\omega_0}\left[\Theta_{\infty 0} - \Theta_\infty(\tau)\right].\end{aligned} \tag{4.50}$$

Thus Eq. 4.46 reads

$$\Theta(\tau) = \Theta_\infty(\tau) - \frac{\gamma}{g\omega_0}\left[\Theta_{\infty 0} - \Theta_\infty(\tau)\right]. \tag{4.51}$$

Consider the case where no steady state solution exist. Switching between SC and NC states occurs when $\Theta(t) = 1$. At that time the mode amplitude B can be found from the value of Θ_∞. Using Eq. 4.51 one finds

$$\Theta_\infty = \frac{1 + \frac{\gamma}{g\omega_0}\Theta_{\infty 0}}{1 + \frac{\gamma}{g\omega_0}}, \tag{4.52}$$

or to first order in $\gamma/g\omega_0$

$$\Theta_\infty = 1 + \frac{\gamma\left(\Theta_{\infty 0} - 1\right)}{g\omega_0}. \tag{4.53}$$

Using

$$\Theta_\infty = \frac{2\alpha\gamma_2\rho\left|B\right|^2}{\omega_0 g}, \tag{4.54}$$

$$\Theta_{\infty 0} = \frac{2\alpha\gamma_2\rho\left|B_\infty\right|^2}{\omega_0 g}, \tag{4.55}$$

one finds the mode amplitude at switching

$$\left|B\right|^2 = \left|B_0\right|^2\left[1 + \frac{\gamma}{g\omega_0}\left(\left|\frac{B_\infty}{B_0}\right|^2 - 1\right)\right], \tag{4.56}$$

where

$$\left|B_0\right|^2 = \frac{\omega_0 g}{2\alpha\gamma_2\rho} \tag{4.57}$$

is the value of $\left|B\right|^2$ for which $\Theta_\infty = 1$. Thus to first order in $\gamma/g\omega_0$ the value of B at switching is given by

$$\left|B\right| = \left|B_0\right|\left[1 + \frac{\gamma}{2g\omega_0}\left(\left(\frac{B_\infty}{B_0}\right)^2 - 1\right)\right]. \tag{4.58}$$

We denote by B_s (B_n) the value of $|B|$ at switching from SC to NC (NC to SC) states.

The period of self modulation is denoted as

$$\mathcal{T} = \mathcal{T}_s + \mathcal{T}_n, \tag{4.59}$$

where $\mathcal{T}_s$ ($\mathcal{T}_n$) is the time period, at which the hotspot is in SC (NC) state. Using 4.47 one finds

$$\mathcal{T}_s = \frac{1}{\gamma_s} \log \frac{B_n - B_{\infty s}}{B_s - B_{\infty s}}, \tag{4.60}$$

$$\mathcal{T}_n = \frac{1}{\gamma_n} \log \frac{B_s - B_{\infty n}}{B_n - B_{\infty n}}. \tag{4.61}$$

Near onset of SM one has $B_s \simeq B_{\infty s}$. In this case one expects that $\mathcal{T}_s \gg \mathcal{T}_n$ (unless incidentally also $B_n \simeq B_{\infty n}$). Moreover writing $\mathcal{T}_s$ as

$$\mathcal{T}_s = \frac{1}{\gamma_s} \left(\log \frac{B_{\infty s} - B_n}{B_{0s}} + \log \frac{B_{0s}}{B_{\infty s} - B_s} \right), \tag{4.62}$$

and neglecting the first term, which is much smaller than the second one, yield

$$\mathcal{T} \simeq \mathcal{T}_s \simeq -\frac{1}{\gamma_s} \log \frac{B_{\infty s} - B_s}{B_{0s}} = -\frac{1}{\gamma_s} \log \left[\frac{B_{\infty s}}{B_{0s}} - 1 - \frac{\gamma}{2g\omega_0} \left(\left(\frac{B_\infty}{B_0} \right)^2 - 1 \right) \right]. \tag{4.63}$$

Let b_0^{in} be the input amplitude associated with onset of SM, namely

$$B_{0s} = -\frac{i\sqrt{2\gamma_{1s}} b_0^{in}}{\gamma_s}. \tag{4.64}$$

Thus, using the notation

$$\vartheta = \frac{b^{in} - b_0^{in}}{b_0^{in}} \tag{4.65}$$

one finds near onset, where $\vartheta \ll 1$

$$\mathcal{T} \simeq \frac{1}{\gamma_s} \log \frac{1}{\vartheta \left(1 - \frac{\gamma}{g\omega_0} \right)} \simeq \frac{1}{\gamma_s} \log \frac{1}{\vartheta}. \tag{4.66}$$

Note that disregarding noise can not be justified very close to onset of the SM, since at that state the system is extremely sensitive to fluctuations.

Spectral Density Near Onset The amplitude $B(t)$ is periodic

$$B(t) = B(t + \mathcal{T}), \tag{4.67}$$

where near onset, where $\mathcal{T}_s \gg \mathcal{T}_n$, one finds

$$B(t) \simeq B_n + (B_{\infty s} - B_n) \left(1 - e^{-\gamma_s t} \right), \tag{4.68}$$

where the time interval, when the hot spot is in NC state, is neglected. Using input-output relation (4.10) yields

$$b_1^{out}(t) = b_1^{in} - i\sqrt{2\gamma_1}B(t). \tag{4.69}$$

The power spectrum of the nth harmonic of b_1^{out} is given by

$$P_n = \frac{1}{\mathcal{T}}\left|\int_0^{\mathcal{T}} b_1^{out}(t)\, e^{i\omega_n t}\, dt\right|^2, \tag{4.70}$$

where

$$\omega_n = \frac{2n\pi}{\mathcal{T}}. \tag{4.71}$$

To find P_n we calculate

$$\begin{aligned}\int_0^{\mathcal{T}} \left(1 - e^{-\gamma_s t}\right) e^{i\omega_n t}\, dt &= \frac{e^{i\mathcal{T}\omega_n}\left(1 - e^{-\gamma_s \mathcal{T}}\right) + i\frac{\gamma_s}{\omega_n}\left(e^{i\mathcal{T}\omega_n} - 1\right)}{i\omega_n - \gamma_s} \\ &= \frac{1 - e^{-\gamma_s \mathcal{T}}}{i\omega_n - \gamma_s},\end{aligned} \tag{4.72}$$

thus for $n \neq 0$

$$P_n = \frac{2\gamma_1 \left(B_{\infty s} - B_n\right)^2 \left(1 - e^{-\gamma_s \mathcal{T}}\right)^2}{\mathcal{T}\left(\omega_n^2 + \gamma_s^2\right)}. \tag{4.73}$$

Using 4.68 yields

$$\left(B_{\infty s} - B_n\right)\left(1 - e^{-\gamma_s \mathcal{T}}\right) = B_s - B_n, \tag{4.74}$$

thus using Eq. 4.66

$$\begin{aligned}P_n &= \frac{2\gamma_1 \left(B_s - B_n\right)^2}{\gamma_s \log\frac{1}{\vartheta}\left(1 + \frac{4\pi^2 n^2}{\left(\log\frac{1}{\vartheta}\right)^2}\right)} \\ &\simeq \frac{2\gamma_1 \left(B_s - B_n\right)^2}{\gamma_s \log\frac{1}{\vartheta}}\left(1 - \frac{4\pi^2 n^2}{\left(\log\frac{1}{\vartheta}\right)^2}\right).\end{aligned} \tag{4.75}$$

Near onset the separation between harmonics is small, thus it is convenient to rewrite Eq. 4.75 as a function of ω_n

$$P(\omega_n) = \frac{2\gamma_1 \left(B_s - B_n\right)^2}{\gamma_s^2 \mathcal{T}}\left[1 - \left(\frac{\omega_n}{\gamma_s}\right)^2\right]. \tag{4.76}$$

4.5.4 Numerical results

The parameters used for the simulation are displayed in table 4.1. The values are extracted from the measurements done on E16 and detailed at section 3.3, where ω_2 is the second resonance frequency of E16 (in GHz), and noise is neglected.

Fig. 4.31 shows numerical solution of the equation of motion of the mode ampli-

Table 4.1: Numerical Model Parameters

Parameter	Eq.	Value	Parameter	Eq.	Value
ω_0	4.24	$\omega_{0s} = \omega_2 \quad \Theta < 1$ $\omega_{0n} = 0.99\omega_2 \quad \Theta > 1$	γ_1	4.24	$0.009/\omega_2 \quad \Theta < 1$ $0.009/\omega_2 \quad \Theta > 1$
γ_2	4.24	$0.017/\omega_2 \quad \Theta < 1$ $15 * 0.017/\omega_2 \quad \Theta \cong 1$ $0.017/\omega_2 \quad \Theta > 1$	ρ	4.17	$2.8e-7$
g	4.15	$4.2105e-2$			

tude in the resonator (Eq. 4.7), and the thermal balance equation in the meander strip (Eq. 4.20). It has three panels, and each has three subplots. The two left subplots describe the normalized mode amplitude B_N (top), and normalized bridge temperature T_N (bottom), as a function of time, where both are normalized by their critical values, at which a transition from the SC to the NC state occurs. The right subplot describes the normalized steady state solution of the mode amplitude, as a function of the normalized frequency, for the case where the bridge temperature is in steady state. The solution is again normalized by its critical value, and the frequency is normalized by the SC resonance frequency. Solid and dashed curves describe stable and unstable solutions, respectively. The blue and red curves are solutions for the SC and NC cases, respectively. Panel (a) shows results calculated for a pump power value below threshold. T_N does not reach its critical value, therefore the SC solution is steady state for all values of the mode amplitude and B_N reaches its steady state. Panel (b) shows results calculated for a pump power value above threshold. The evolution of B_N in time is described as followed. At start, the mode amplitude inside the resonator increases towards its steady state value. At $t_1 = 38.6\,\text{ns}$, it reaches its critical value, T_N however slightly lags behind, as predicted by Eq. 4.46, and reaches its critical condition at $t_2 = 40.15\,\text{ns}$. At that time the resonator switches to the NC state, and thus the NC steady state solution becomes stable and the SC steady state solution unstable. B_N reaches its maximum and starts to decrease towards the value predicted by the NC steady state solution. As a response T_N starts to decrease until, at t_3, it is decreased below the critical value, thus the resonator switches back to the SC state, B_N starts to increase again, and a new cycle begin. Panel (c) shows results calculated for a pump power value above the second threshold. At this power the SC steady state solution is unstable at the frequency of excitation and the NC solution has a stable solution. Therefore B_N crosses the critical value, and after a few overshot oscillations, it is stabilized at a value above critical. In correlation, T_N is stabilized above its critical temperature.

4.6 Summary

The self-oscillation phenomena, both at high and low frequency, is a robust behavior that characterizes our devices. It is observed in all devices, at various resonance

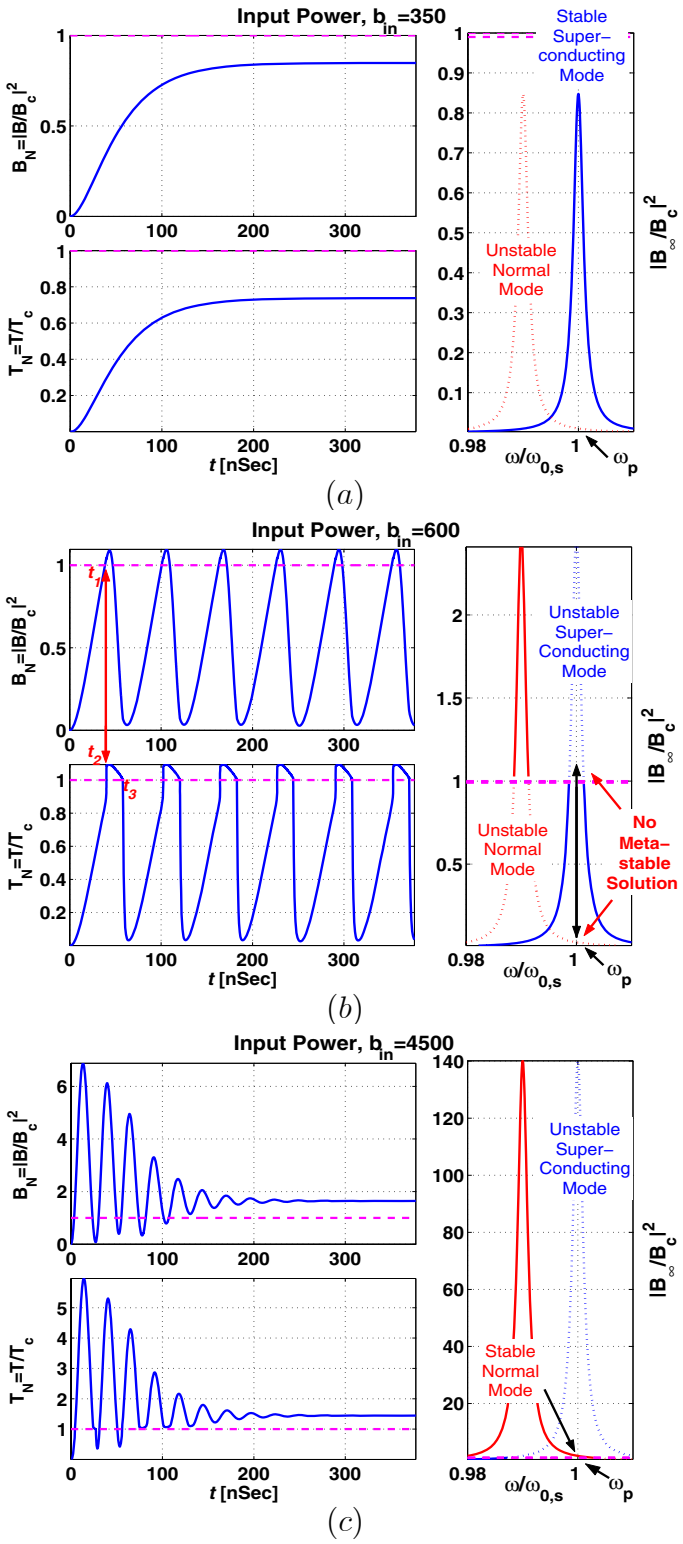

Figure 4.31: Numerical solution at pump powers (a) below, (b) above first , and (c) above second threshold. The subplots describe the mode amplitude (left top), and bridge temperature (left bottom), as a function of time, and the steady state solution of the mode amplitude, as a function of the frequency (right). Solid and dashed curves describe stable and unstable solutions, respectively. Blue and red curves describe solutions for the superconducting and normal cases, respectively.

frequencies and various power ranges. Similar HFSM dependence on pump frequency and power is repeatedly measured at all devices. They all experience a threshold power at which the HFSM starts. The behavior of the devices at threshold slightly differs between devices but is usually chaotic-like and always extremely nonlinear and unpredictable. The HFSM threshold power is followed by a larger power range at which regular HFSM are observed. The HFSM ends at a second threshold power at which the behavior is device dependence.

LFSO with a frequency of a few Hz exist concurrently, and coupled to LFSO with a time period of tenth of seconds. Both are correlated to the high frequency self-modulations. In addition, LFSO, with a time period of several second, are observed at lower pump power frequencies, and are probably not correlated to thee HFSM.

As the devices differ in geometry, the HFSM behavior also has device dependent characteristics. E15 shows HFSM at two power ranges, between which the resonance frequency shifts. It is also characterized by a chaotic-like behavior at the second threshold power. E16 has a much lower threshold powers for the HFSM phenomena. Its resonance frequencies shift and is reconstructed, rather than disappear at the second threshold power. Its time-dependent oscillations are less stable than the ones measured at other devices. E13 is characterized by a strong nonuniformity of the HFSM sidebands at threshold powers and asymmetric frequency response around the resonance frequency. the asymmetric frequency response can be originated from coupling to neighboring resonance frequencies, as described in the next chapter.

A theoretical model according to which the self-sustained oscillations are originated by thermal instability in the meander strip is proposed to account for our findings. A comparison of the model's predictions with experimental results yields a partial qualitative agreement. The model is presently still being developed so the outcome is still not final.

Chapter 5

Giant Nonlinear Phenomenons

5.1 Introduction

The HFSM phenomena is a robust and strong nonlinear behavior that occurs in our devices. During the process of characterizing the HFSM phenomena we have noticed that several nonlinear phenomenons manifest themselves in correlation with the HFSM. In this chapter these nonlinearities are described and characterized. An emphasis is put on the correlation between the HFSM and these phenomenons. The following phenomenons are described:

1. Self-excitation of resonance modes.
2. Intermodulation.
3. Period doubling of various orders.
4. Noise squeezing - Phase sensitive amplification.
5. Optical and RF signal mixing.

Self-excitation and period doubling are only measured in E13. All other phenomenons are measured is all devices, without substantial differences between different devices. As so, each phenomena is described using typical results, taken at the same device and resonance mode.

5.2 Self-Stimulation of Resonance Modes

While characterizing the HFSM phenomena, seen at E13 device, we have witnessed another nonlinear phenomena in which self-excitation of self-resonance modes (SE) occurs. The SE occurs due to coupling between resonance modes, that takes place when one of the modes is externally stimulated and undergoes HFSM. Fig. 5.1 shows a typical measurement, in which the SE is observed. This graph shows the reflected pump power P_{refl}, in a frequency band of 700 MHz, as a function of the pump power P_{pump}, centered around $n2a$ resonance mode, $f_c = f - f_{2a}$. The frequency band also shows $n2b$ resonance mode, whose resonance frequency is approximately 350 MHz

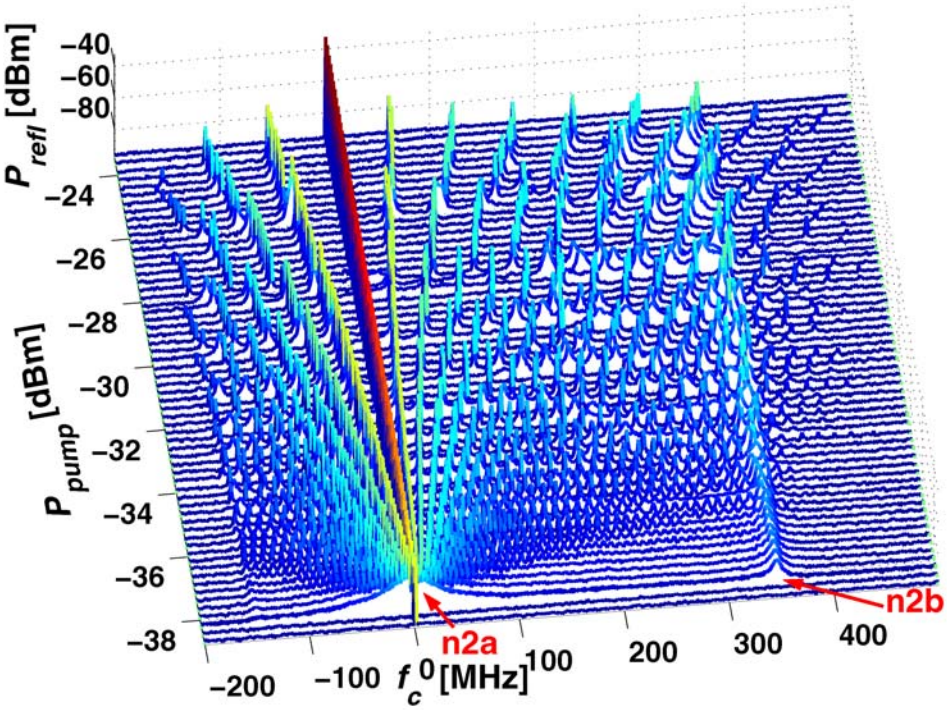

Figure 5.1: SE measurement. Reflected power P_{refl}, in a frequency band of 700 MHz around $n2x$ resonance, as a function of pump power P_{pump}.

higher than f_{2a}. The device is stimulated by a pump signal at frequency f_{2a}. The HFSM threshold power is also the threshold power, in which SE of $n2b$ begins, and power is being measured at that mode. As the input power increases, HFSM of the self-excited mode are observed. Naturally, the sidebands that appear around $n2b$ are weaker than the ones around $n2a$, but as a result of the coupling, the sidebands around $n2a$ are asymmetric and stronger towards $n2b$.

The SE is measured at resonance modes $n1x$, $n2x$, and $n4x$ of E13. It is also measured at E16 but an additional suppression of the resonator, by injection of external noise, is needed for the SE to occur.

5.3 Intermodulation

5.3.1 Introduction

One of the common ways to characterize nonlinearities in superconductors is intermodulation measurement [45]. Intermodulation or intermod (IM) is the result of two signals of different frequencies being mixed together by a nonlinear system, forming additional signals at frequencies that are linear combinations (integer multiples) of both. The largest IM products appear at $f_1 + f_2$ or $f_1 - f_2$ (second-order IM), and less so at $2f_1 - f_2$ or $2f_2 - f_1$ (third order IM) [14]. The experiment setup used for IM is depicted at Fig. 5.2. The resonator is stimulated by two phase-locked sig-

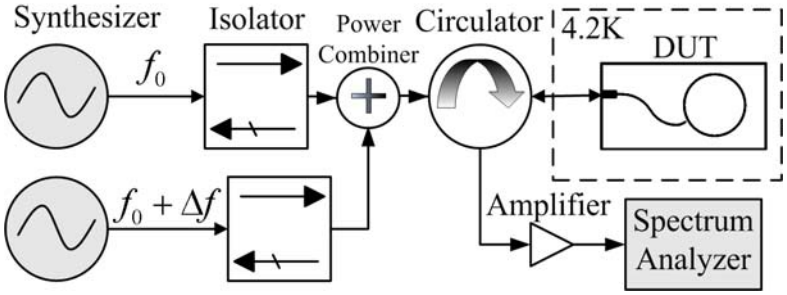

Figure 5.2: Setup used for IM reflection measurements.

nal. One, called Pump, is a relatively strong signal, that biases the resonator into the nonlinear region. The other, called Signal, is a relatively weak signal, whose frequency, $f_{sig} = f_{pump} + \Delta f$, is deviated by a few hundreds Hz away from the pump frequency f_{pump}. The reflected power off the resonator is measured with a SA. The focus of the measurement is put on measuring the reflected Pump, Signal and Idler tones. The Idler is a third order IM tone, measured at frequency $f_{Idler} = 2f_{pump} - f_{sig} = f_{pump} - \Delta f$ [5].

5.3.2 Experimental results

Fig. 5.3 shows a typical IM measurement taken at $n3$ resonance of E15. The resonator is stimulated as described in the previous paragraph, where $\Delta f = 800\,\text{Hz}$. The pump power is set to the threshold of the HFSM. The reflected power P_{refl}, is plotted in a frequency band of 3.5 kHz centered around the resonance frequency, $f_c = f - f_3$. The reflected Pump, Signal and Idler tones are easily detected, as well as higher order mixing products.

The strength of the IM is characterized using two parameters. One is IM signal gain, defined as the ratio between the output signal power to the input signal power. The other is IM Idler gain, defined as the ratio between the output Idler power to the input signal power,

$$G_{sig}^{IM} \equiv \frac{P_{sig}^{out}}{P_{sig}^{in}};\ G_{sig}^{IM} \equiv \frac{P_{idler}^{out}}{P_{sig}^{in}}. \tag{5.1}$$

Fig. 5.4(a) plots a 3DFV summarizing graph, in which the IM Signal gain is plotted as a function of the Pump and Signal powers. The areas of strong amplification are indicated by red shaded colors. Two areas of strong amplifications are easily noticed, at relatively low and high pump powers. At power region in between no amplification occurs. A very strong and strong amplification of 30.66dBm and 17.77dBm is achieved at the first and second areas, respectively. To emphasize the strength of these amplifications we must note that, usually no amplification at all is achieved at such measurements in superconducting resonators. Fig. 5.4(b) plots the Signal gain, as a function of pump power, for a signal power of −86dBm, for which the maximum in the Signal amplification is achieved. This graph emphasizes how

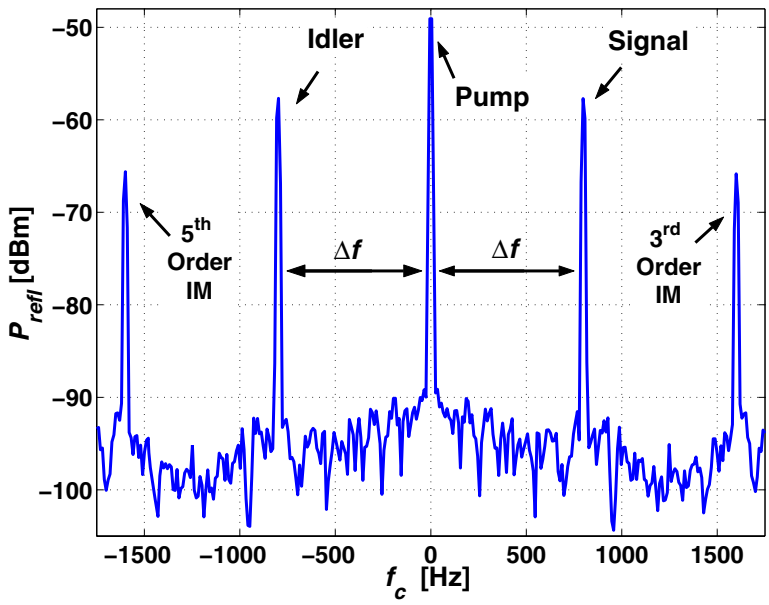

Figure 5.3: 2D IM measurement. Reflected power in a frequency band of 3.5 kHz around $n3$ resonance mode.

narrow the power range, at which large Signal gain is achieved, is. It appears as a nearby delta function in a logarithmic scale, and is only approximately 5 nW wide.

The same measurement data is used to extract the Idler gain. The results are plotted is Fig. 5.5. In correlation to the Signal amplification, two areas of strong amplifications are easily noticed at rather low and high pump powers. A very strong amplification of 30.85dBm and a strong amplification of 16.36dBm is achieved at the first and second areas, respectively. As expected, these values closely match the Signal gain values. A much weaker, but yet not negligible, Idler signal is detected outside these narrow power ranges. The detection of an Idler, especially before the first threshold power, probably indicates the presence of additional nonlinear mechanisms that cause signal mixing. These nonlinearities are, by far, much weaker then the HFSM nonlinearity as they don't produce a gain greater than unity.

In order to check the correlation between the IM phenomena and the HFSM phenomena, HFSM measurement data has been collected simultaneously with the IM data. Fig. 5.6 plots one on top of the other two graphs. The blue graph shows the IM Signal gain as a function of pump power, as plotted in Fig. 5.4(b). The green curve shows the HFSM frequency as a function of the pump power. The comparison clearly shows that the strong IM gain is achieved at the threshold powers, at which the HFSM starts and ends. This finding indicates that there is a strong correlation between these two phenomenons and greatly increase the interest in analyzing the behavior of the devices at these regions.

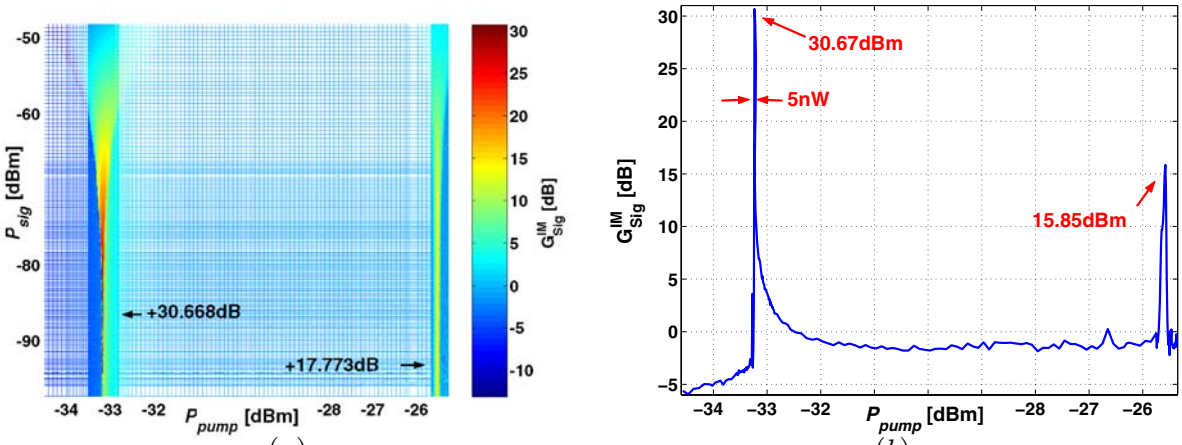

(a) (b)

Figure 5.4: IM signal gain as a function of pump power and, (a) Signal power, (b) Signal power equals to −86dBm.

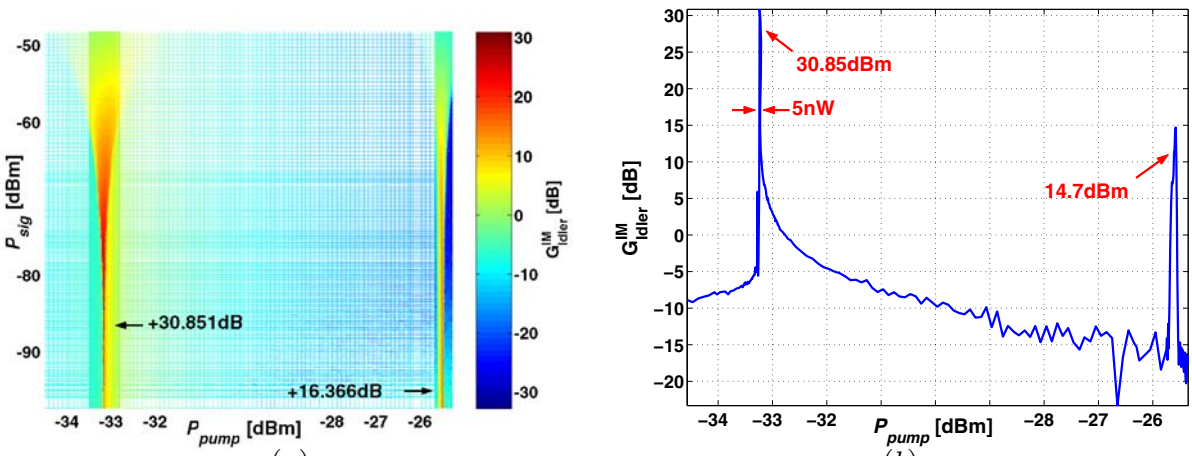

(a) (b)

Figure 5.5: IM Idler gain as a function of pump power and, (a) Signal power, (b) Signal power equals to −86dBm.

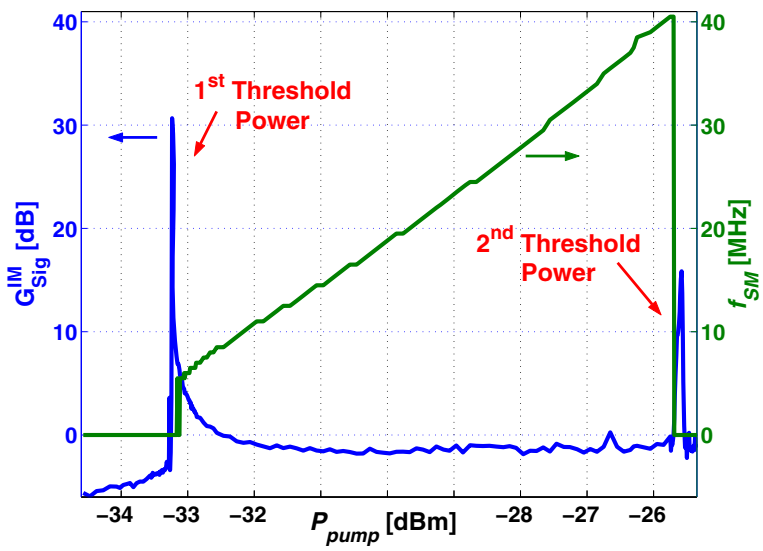

Figure 5.6: IM Signal gain and SM frequency as a function of pump power.

5.3.3 Summary

IM is measured at all resonance modes that show HFSM. The IM gain is very strong at the threshold power regions where the HFSM starts and stops. Very strong IM gain is measured in E15, and slightly weaker in E13. A much weaker, but still impressive IM gain of $G^{IM}_{idler} = 8.55$dBm is achieved at E16, around a threshold power of -50.5dBm. The correlation between the HFSM threshold power and the IM amplification greatly increases the interest in analyzing the behavior of the devices at these regions.

5.4 Period doubling of various orders

5.4.1 Introduction

It has been found that in some nonlinear systems the transition to chaos can occur via consecutive period doubling bifurcations (PDB) instability of various orders [42], [19], [38], [8]. It was shown that near the onset of a PDB, any dynamical system can be used to amplify perturbations near half the fundamental frequency. The closer the bifurcation point, the greater the amplification [53]. Our device exhibits PDB, which might explain the strong amplification at the HFSM threshold power.

5.4.2 Experimental results

The observation of PDB route to chaos is done at E13 device. Naturally, the sub-harmonics that result from PDB do not coincide with self-resonance modes of the resonator and therefore can not be directly measured. The measurement of PDB is done using IM mixing, where the sub-harmonics of the Pump and Signal mix together and appear at new frequencies in the vicinity of the stimulated resonance mode.

This measurement scheme has limitations. We observe one nonlinear phenomena using another nonlinear phenomena and this introduces distortions and noises to the measurement. One such noise is a second order mixing between the Pump or Signal tones and low frequency tones, which produces new tones at close frequencies to the measured tones originated by the PDB.

Fig. 5.7 shows four panels, in which PDB is observed. Each panel shows an IM measurement, in which the reflected power is plotted in a frequency band of 4 kHz around the resonance frequency. The device is stimulated by a strong pump power, that equals the threshold power of the HFSM, at $n4a$ resonance, and a weak signal, 800 Hz apart from the pump. Although the threshold power of the IM is very narrow, we use the fact that, the power resolution of the SYN instrument is constant in logarithmic scale, and make many different IM measurement by only varying the weak Signal power. In this way we make a large variety of measurements at the HFSM threshold power. Looking at panel (a) the usual tones measured at IM, Pump, Signal, Idler, and high order tones, are easily observed. In addition we observe a new type of reflected tones which are half integer multiples of the Pump and Signal frequencies. For example, the two marked tones are found at $(f_p + f_s)/2$, and $(3f_p - f_s)/2$ frequencies. This measurement is a clear evidence that a period doubling of the second order occurs in the resonator. Panel (b) and (c) show additional measurements, at a slightly different signal power, in which period doubling of forth and triple orders occur, respectively. Panel (d) shows a measurement in which a chaotic-like behavior is observed. This behavior is characterized by a strong amplification of the noise floor and an high absorption of the pump power.

5.4.3 Summary

PDB is indirectly observed at our device, by using IM measurement technique. Various orders of PDB as well as broadband and strong amplification of the noise floor are measured. The measurement technique distorts the measured data in a way that prevents quantitative comparison to the PDB theory.

5.5 Noise squeezing - Phase sensitive amplification

5.5.1 Introduction

A parametric amplifier can establish correlations [58] between the output at $f_p + \Delta f$ and $f_p - \Delta f$, where $\Delta f = |f_s - f_p|$, as a result of IM gain. When delivered to a mixer, operated in the homodyne mode, whose local oscillator is phase-locked to the pump, these correlations can result in noise fluctuations reduced below that which the mixer would see if the signal delivered to the parametric amplifier were, instead, directly delivered to the mixer [59]. This noise reduction is called squeezing, and can occur with either thermal [56] or quantum noise [46]. The theory is detailed in [58], and summarized in [57]. The noise being squeezed in our resonator is the sidebands spectral power produced by the HFSM phenomena. As this is not a broadband white noise, which is usually referred to as noise in papers dealing with squeezing,

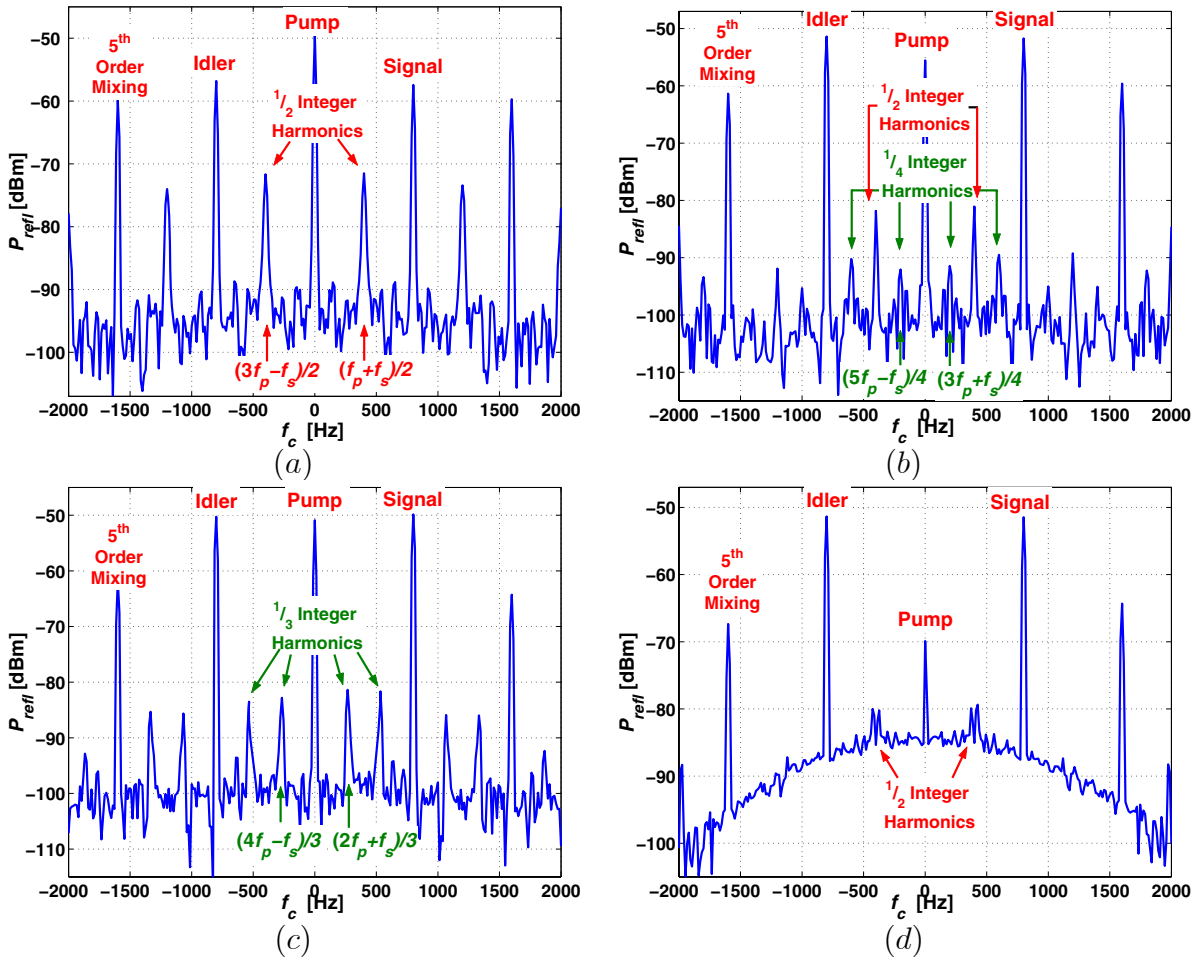

Figure 5.7: Period doubling measurement. Reflected power measurement in a frequency band of 4KHz. The usual Pump, Signal, and Idler tones, and in addition (a) half, (b) quarter, and (c) third integer multiples of the Pump and Signal tones are measured. Panel (d) shows chaotic-like behavior, characterized by a strong amplification of the noise floor.

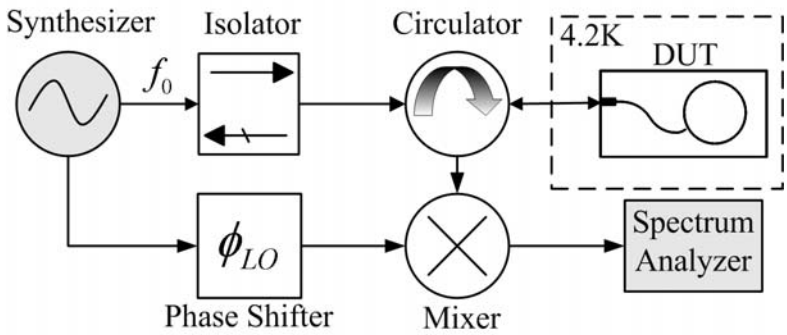

Figure 5.8: Setup used for PSA measurement.

we will refer to noise squeezing in our device, as phase sensitive amplification (or deamplification) (PSA).

The experiment setup used for PSA, which utilizes homodyne detection measurement scheme, is depicted in Fig. 5.8. The resonator is stimulated by a CW pump signal, and the reflected power is fed to an external mixer, driven by a local oscillation (LO) signal whose frequency equals the pump frequency. The LO is phase-locked with the pump and its phase is controlled by a motor-driven phase shifter. The output of the mixer is measured by a SA.

5.5.2 Experimental results

Fig. 5.9 shows a typical PSA measurement taken at E15. The resonator is stimulated with a pump at frequency f_2 driving the resonator into the HFSM state. The mixer's output power is measured in a frequency band starting from DC and ending at 45 MHz. The graph has three curves. The blue curve shows the measured spectrum at its maximum value. The pump signal is down converted to dc and the HFSM sidebands are down-converted, respectively to the pump. We'll refer to this measurement as taken with a zero LO phase, $\phi_{LO} = 0$. The red and greed curves are taken with $\phi_{LO} \cong \pi/2$, one slightly below and slightly above $\pi/2$, respectively. The deamplification of the noise, relatively to $\phi_{LO} = 0$ data is clear. A comparison of the two curves revels that, the deamplification is very sensitive to the LO phase. Different frequencies has slightly different phases so they reach their minimum value at slightly different LO phase. We define the squeezing factor as the ratio of the measured signal at its maximum value to the measured signal at its minimum value.

Fig. 5.10 shows a 3D graph of the measurement just described, taken for various LO phase values. The dependence of the reflected power on the LO phase is clearly observed, where the phase period equals π, as expected.

The same measurement presented in Fig. 5.10 is repeated for various input powers, and the squeezing factor is calculated for each measurement. Fig. 5.11 plots the squeezing factor as a function of pump frequency and power. One can observe, that large and broadband squeezing is achieved at two power ranges, where the strong IM gain is measured. In addition the HFSM sidebands undergo strong squeezing, with a maximum that reaches 40.5dBm.

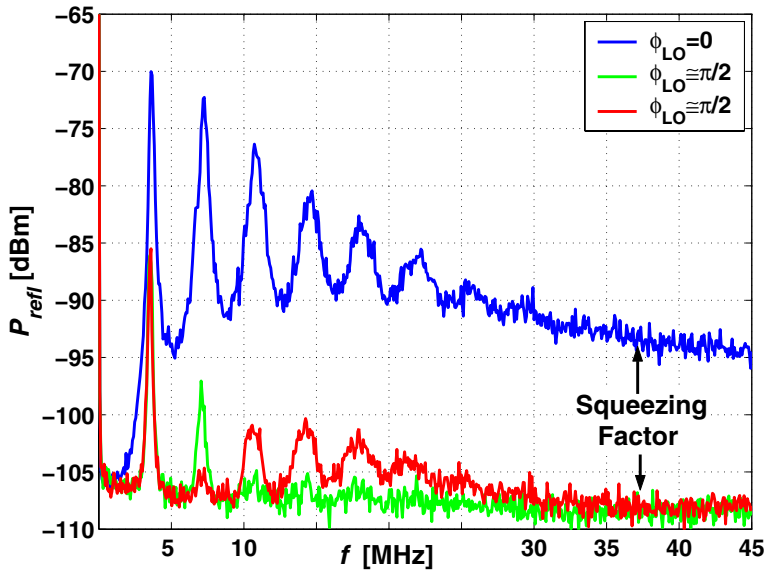

Figure 5.9: PSA measurement. Reflected power measurement in a 45 MHz frequency band, taken for $\phi_{LO} = 0, \tilde{}\pi/2$.

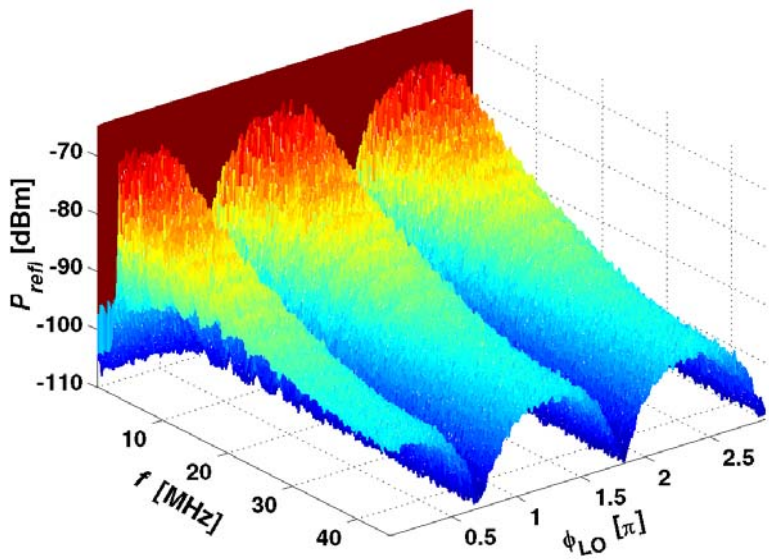

Figure 5.10: PSA measurement. Reflected power measurement in a 45 MHz frequency band as a function of the local oscillator phase.

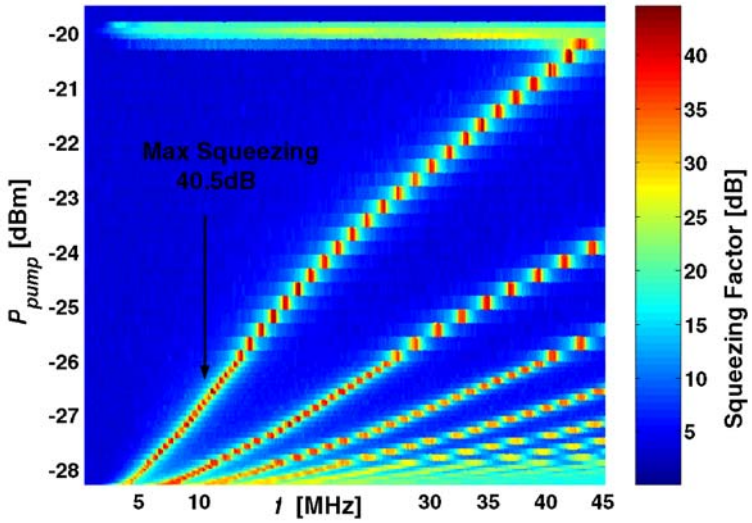

Figure 5.11: Squeezing factor as a function of frequency and pump power.

5.5.3 Summary

Strongly correlated to the IM phenomena, the PSA is measured at all resonance frequencies and devices that show HFSM. The phase sensitive amplification is broadband and strong at the threshold powers where the HFSM begins and ends. In additional, an even stronger squeezing is achieved at the HFSM sidebands where a maximum of 40.5dBm is measured.

5.6 Optical and RF Signal Mixing

5.6.1 Introduction

Optical and RF Signal mixing (ORSM) mechanism is based on parametric excitation that causes fast resonance frequency modulation. The frequency modulation mechanism, we employ here, is based on changing the boundary conditions of a SC resonator. This is done by switching a small section of the resonator to a NC state by using optical illumination. The switching time in superconductors is usually limited by the relaxation process of high-energy quasi-particles, also called 'hot-electrons', giving their energy to the lattice, and recombining to form Cooper pairs. Recent experiments with photodetectors, based on a thin layer of SC NbN, have demonstrated an intrinsic switching time on the order of 30 ps and a counting rate exceeding 2 GHz (see [24] and references therein). Resonance frequency shift by optical radiation [12], [10], [51], or high-energy particles [15], [52] (for which the required condition $\xi Q \cong 1$ has been achieved) was demonstrated, though no periodic modulation was reported. Resonance frequency tuning [9] and switching [41] as well as optical and microwave signal mixing [36], [26] were demonstrated in NC GaAs microstrip ring resonators.

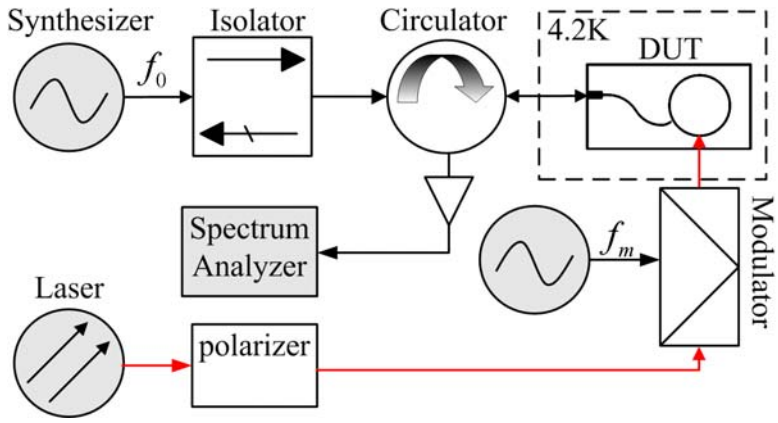

Figure 5.12: Setup used for optical and RF signal mixing.

5.6.2 Experimental results

Optical and RF Signal Mixing is performed using the experimental setup depicted in Fig 5.12, in E16 device. The resonator is excited by a CW pump signal, at frequency $f_0 = 3.71\,\text{GHz}$, which coincides with the second resonance frequency. The optical signal is modulated at frequency f_m, using a Mach-Zener modulator driven by a second CW signal, phase locked with the first one. The reflected power is mainly composed of three tones. One is the reflected pump signal at frequency f_0. The other two are sidebands, produced by mixing the pump signal and the optical modulation signal, and are found at frequencies $f_{a,b} = f_0 \pm f_m$. Occasionally, higher orders of the mixed signals are also detected. The amplified reflected power is measured using a SA, which tracks the $f_a = f_0 + f_m$ tone for $f_m \lessapprox f_0$ frequency and $f_b = f_m - f_0$ for $f_m \cong 2f_0$ frequency. No dc bias is needed in this measurement as the RF probe signal also serves as a bias signal for the HED. This bias scheme has two major advantages over the dc bias scheme; first the RF pump bias signal has lower noise, as the $1/f$ and line noises are avoided. Second, the induced optical signal is being amplified by the same nonlinear phenomena that produces the strong IM gain.

Fig. 5.13 shows the reflected power in a frequency band around $n2$ resonance. The pump power is set to the HFSM threshold power, -50.8dBm. The optical signal power, impinging on the HED, is set to approximately 220fW, and is being modulated at frequency $f_m = 2f_0 + \Delta f \cong 7.74\,\text{GHz}$, where $\Delta f = 800\,\text{Hz}$. The measured reflected power spectrum resembles the one measured in IM measurement, and for good reasons. We identify a tone at frequency $f_s = f_m - f_0 = f_0 + \Delta f$, which is exactly Δf apart from f_0. This tone is the product of a second order mixing between the optical modulated signal and the RF pump signal. Moreover, by having two tones, Pump and Signal, whose origin is of no importance, IM occurs, and therefore an Idler tone and higher order tones are also observed.

The correlation between the ORSM and the HFSM phenomena, is tested, as is done in IM measurement. Fig. 5.14 plots, one on top of the other, the optical tone detection level (blue) and HFSM frequency (green) as a function of the pump power. The comparison clearly shows that the strongest detection is achieved at the threshold

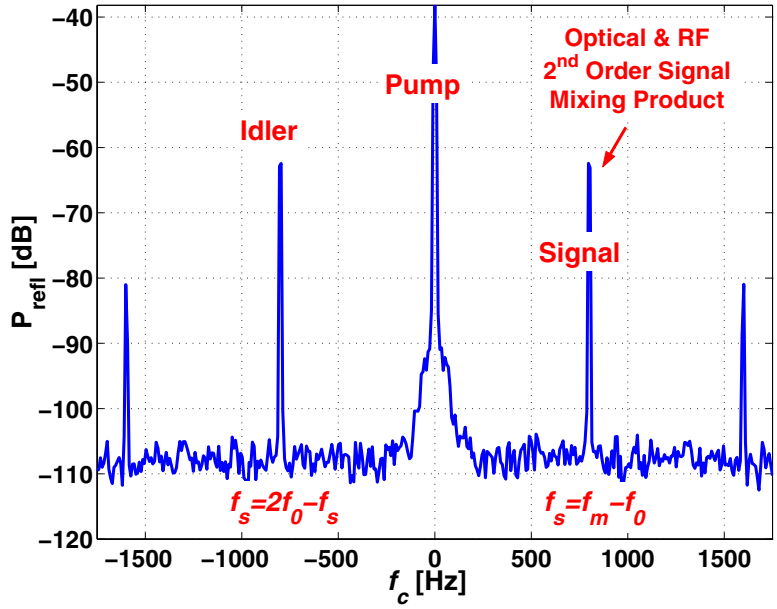

Figure 5.13: ORSM measurement. Reflected power measurement in a frequency band of 3.5 kHz around $n2$ mode.

power, at which the HFSM starts. This finding indicates that there is a strong correlation between the optical detection ability, IM nonlinearity and HFSM phenomena. The detection of high frequency modulated optical signals becomes possible only due to the very strong IM gain that occurs on the threshold of HFSM.

The device is not designed for radiation detection. Nevertheless, we find it useful to characterize the response to optical modulation by its noise equivalent power (NEP). Fig. 5.15 shows the NEP of the device for various optical modulation frequencies. Each NEP data point is derived out of several reflected power measurements in the vicinity of f_a, where each measurement is performed with a different pump power, ranges between -54.7 dBm and -45.7 dBm. The best NEP is measured for a modulation frequency of $f_m \cong 7.74$ GHz and equals $34\text{fW}/\sqrt{\text{Hz}}$. The second best is measured for for a modulation frequency of $f_m = 10$ MHz and equals $38\text{fW}/\sqrt{\text{Hz}}$. A rather low NEP of $370\text{fW}/\sqrt{\text{Hz}}$ is measured for a modulation frequency of $f_m = 1.699$ GHz. For this modulation frequency, f_a coincides with the third resonance frequency of the resonator. We must note that the detection of such high modulation frequencies is surprising, as for most frequencies f_a does not coincide with any self-resonance frequency of the resonator, and therefore should have been significantly suppressed. For a stationary system, this observation would probably indicates a rather low Q-factor. As it is not appropriate to use the term Q-factor for a dynamical changing system, it is more accurate to indicate that the IM gain, that occurs on the threshold of the HFSM, is of a broadband nature. This means that the response of the resonator is not limited to a narrow frequency band around its resonance frequencies.

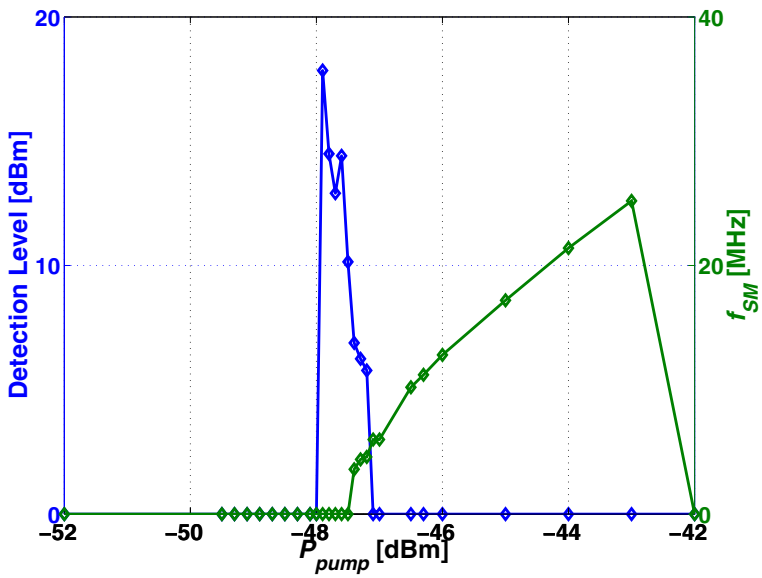

Figure 5.14: Optical and RF signal mixing detection level compared to self-modulation frequency as a function of pump power.

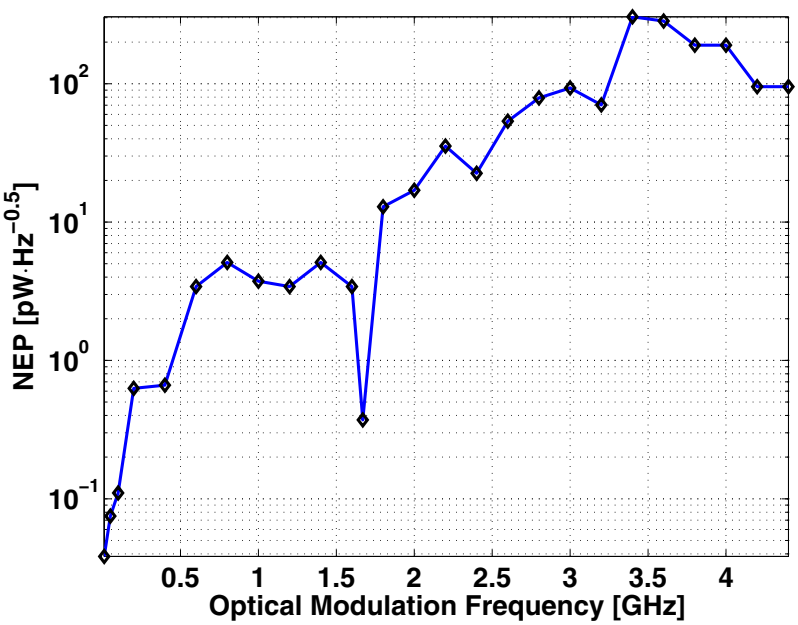

Figure 5.15: NEP for various optical modulation frequencies.

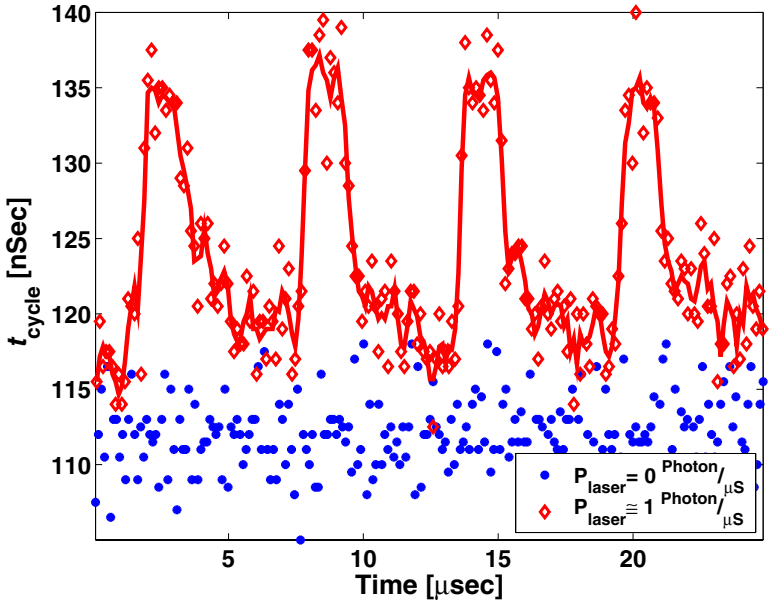

Figure 5.16: SM cycle time as a function of time under CW illumination.

5.6.3 Single photon detection

Our devices has, in theory, the ability to detect a single photon absorption event. In this section we present a preliminary data, according to which this ability is indeed realized. At present, we do not have an experiment setup, that can directly detect a change in the reflected power, due to an event of photon absorption. Therefore a different measurement scheme is employed. We hypothesize that the degree of freedom, which is most likely to respond to a photon absorption, is the time phase of the self-oscillations. We stimulate E13 resonator with a pump power that produces HFSM and measure the time phase between sequent oscillations. Fig. 5.16 show that measurement, where the time phase between oscillations is plotted as a function of time. The red and blue curves are taken with and without illumination, respectively. The illumination power is attenuated down to the point, where the photon flow that impinges the HED equals approximately to 1 photon per microsecond. Looking at the red curve we observe oscillations of the self-oscillations cycle time. The oscillations occur approximately once every 6 μs. The oscillation frequency is in good correlation with the impinging photon frequency, taking into account the quantum efficiency of NbN, which is less than 10% [33]. The oscillation's lineshape is composed of a sharp increase followed by a slower relaxation decrease in the cycle time. Currently, we can't determinate the exact interaction between the hotspot produced by a photon absorption and the HFSM which are probably also originated by hotspot formation. Intuitively, when a photon is absorbed the local temperature of the HED is increased and relaxation oscillations such as the HFSM should have a longer cycle time.

5.6.4 Discussion

Fast modulation of the resonance frequency is experimentally demonstrated in this section. Furthermore, the parametric gain threshold condition is achieved in a CW measurement, described in section 3.5. The main problem, that currently prevents parametric gain to occur, is the relatively low photon flux that impinges the HED. Due to losses along the optical path, especially the expansion of the Gaussian beam from the tip of the fiber to the HED, described in section A.B, the largest photon flux we currently manage to apply is approximately 13 photons per modulation cycle, at twice the resonance frequency. Taking into account the effective area of the HED and its quantum efficiency [33] we estimate that the optical power flux is two orders of magnitude lower than the threshold power. Therefore parametric gain can not be achieved using the present device.

The single photon detection measurement is of preliminary nature only. It was only performed once, and more measurements are needed to characterize the exact response of the HFSM to light absorption. Nevertheless, there is a great potential of improving the current results. First, this measurement was done in E13 device, which has a reduce response to illumination compared to E16. Moreover, with the suitable experimental setup, the response of the resonator to photon absorption can be tested, while the device is biased to the HFSM threshold power, in which the device experiences the strongest nonlinearity. These results encourage us to further pursue the goal of single photon detection, as our device, being utilizing strong nonlinearity, has a great potential to outperform all currents detectors in sensitivity [33] and quantum efficiency, while maintaining rather high detection frequency.

5.6.5 Summary

We study the response of the device to IR (1550 nm wavelength) illumination impinging on the meander strip. To characterize the response time of the system we modulate the impinging optical power with a varying frequency. We observe extremely fast (modulation frequencies of up to 8 GHz) and sensitive (optical power below 50 fW) response near the onset of the self-sustained oscillations. Preliminary data also shows that the device has an ability to detect a single photon absorption.

5.7 Summary

Our devices exhibit strong nonlinear behavior, which is realized in various ways, in correlation with the HFSM phenomena. Self-excitation of resonance modes occurs in E13 between coupled resonance modes, and moreover the self-excited mode undergoes HFSM. Intermodulation occurs in all of our devices, and is characterized by very strong Signal and Idler gain at the HFSM threshold power. Period doubling of various orders occurs at the threshold power of the HFSM in E13, and is measured by using IM upconversion of the low frequency tones. Phase sensitive amplification is measured at all of our devices, and shows strong squeezing factor in correlation with the IM strong gain. Finally optical and RF signal mixing is observe, with extremely fast and

sensitive response near the onset of the self-sustained oscillations.

Chapter 6

Summary

We study microwave superconducting stripline resonators made of NbN on Sapphire substrate, operating at low cryogenic temperature of 4.2 K, while the devices are fully immersed in liquid Helium. The research original goal has been to achieve parametric gain in superconducting microwave resonators. To achieve this goal one of the resonance frequencies of the resonator has to be regularly modulated in a frequency, which is twice the resonance frequency. Therefore the resonators are designed to have tunable resonance frequencies, which can be quickly shifted by external constrains. We employ new technological ideas, taken from the field of single IR photon detectors, and design a section of the resonator, which is made of a narrow (150 nm) and thin (8 nm) meander strip, which implements a single photon detector as a monolithic part of the resonator. In this way, the resonator is made extremely sensitive to external constrains applied directly on the detector, such as dc voltage or current, and IR light (or any other higher frequency radiation), or to indirect constrains, such as the microwave power that stimulates the resonator. These constrains can shift a resonance frequency by more than its 3dB width, while maintaining high Q-factor, and thus fulfill the second demand that is required for parametric gain. A theoretical model, that describes the resonator as a transmission line, that its ends are connected together by a discrete impedance element, which represents the detector, produces a good prediction to the dependence of the resonance frequencies and the damping rate on the resistance of the detector.

In addition to the resonance frequency shift, the resonator exhibits a new kind of nonlinear behavior, originated by thermal instability. Novel, self-sustained oscillations of the reflected power, at frequencies of down to 0.01 Hz and up to 60 MHz are observed, when a continuous wave at frequency close to one of the resonances is injected into the resonator and the reflected power off the resonator is measured. Non of the self-sustaining oscillation frequencies are a self resonance frequency of the res-

onator. The modulation frequencies are divided into two groups. One includes high modulation frequencies, that ranges between 5 MHz to 60 MHz. The second includes low modulation frequencies, which again can be divides into three subgroups, that includes modulation frequencies of a few Hertz, modulation with cycle time of a few seconds and modulation with cycle time of a few tenth of seconds. These groups are coupled together through their dependence on the pump power, that stimulates the resonator, and differ one from another by the power, at which they occur, and by the line shape of the oscillations. Up to three distinct oscillation frequencies can be concurrently observed.

The existence of the oscillations are bounded by both pump power and frequency, where the device experiences strong nonlinearity and even chaotic-like behavior at the boundaries, at which the self-modulation starts and ends. The fast modulation frequencies are positively correlated to the pump power and discretely correlated to the pump frequency, this means that a small change of the pump frequency can abruptly start or stop the modulations, but while the modulations occur, it has a weak dependence on the pump frequency. To the best of our knowledge such oscillations were not reported before in similar systems. To account for our findings, a theoretical model according to which the self-sustained oscillations are originated by thermal instability in the meander strip is proposed. The instability is originated from the coupling between the equation of motion of the mode amplitude in the resonator and the heat balance equation in the detector. A comparison of the model's predictions with experimental results yields a partial qualitative agreement.

Near the onset of these oscillations the device exhibits a chaotic like behavior and is characterized by giant nonlinearity. Intermodulation characterization performed in this state yields extremely high intermodulation gain (about 30dB). The intermodulation is accompanied by a very strong noise squeezing, also known as phase sensitive amplification phenomena. When making an homodyne detection of the reflected power off the resonator, the measured reflected power is strongly dependant on the phase of the local oscillator. The strongest amplification is measured at the threshold power of the self-modulation and at its measured sidebands, where the difference between the strongest and weakest measured power can reach up to 45dB. In addition, by taking advantage of the strong signal mixing that occur in the resonator we observe another nonlinear phenomena called period doubling of various orders, that occurs at the self-modulation threshold power. The period doubling is characterized by the creation of new tones at frequencies, which are rational fractions of the injected signals. In our devices we observe tones at frequencies, which are half integer, quarter and third of the original pump frequency, and in additional a broadband chaotic-like

amplification of the noise floor. Finally, coupling of resonance modes is realized by self-exitation of self resonance modes, while the device under goes self-oscillations, and also the self-excited mode undergoes self-oscillations.

As part of the goal of achieving parametric gain, we study the response of the device to IR (1550 nm wavelength) illumination impinging on the meander strip. To characterize the response time of the system we modulate the impinging optical power with a varying frequency, and perform optical and RF signal mixing. We observe extremely fast (modulation frequencies of up to 8 GHz) and sensitive (optical power below 50 fW) response near the onset of the self-modulation, which is realized due to the strong intermodulation gain at that region. In addition, a preliminary measurement, in which the influence of a single photon absorption on the self-modulation cycle time, is tested. In this measurement we observe oscillations in the cycle of the self modulation, where an oscillation cycle lasts a few micro-seconds, in correlation to the photon flux impinging the detector.

To achieve parametric gain on future devices the optical intensity impinging the detector should be approximately two orders of magnitude stronger that the current one. We design and implement Fresnel lenses, which would focus and intensify the IR light on the meander strip. Future devices will fully integrate this lens with our current devices.

Appendix A

Fresnel Zone Plate

A.1 Introduction

As discussed in 5.6.4, parametric gain can not be achieved in the current device due to insufficient light intensity impinging the HED, and therefore a lens is needed in order to focus the light on the HED. The lens has to deal with the following demands. First, it has to efficiently focus the light onto a rather close focal plane. Second, it has to withstand cooldown cycles to liquid Helium temperature. Third, it has to be compatible with microelectronics fabrication processes. Finally, it has to be aligned to the HED, where no alignment can be performed after device cooldown.

Fresnel zone plate (FZP), or Fresnel lens, has the right characters that fits these tight demands. It is manufactures as part of the device, during the fabrication process, on the back side of the Sapphire, using the same EBL and etching techniques used to manufacture the device itself. The alignment is done as part of the manufacturing process, and is ignorant to the cooldown strains, in good approximation. Finally, the characteristic dimensions, needed for focusing the light on the HED, as calculated by Eq. A.9, are easily achieved in standard EBL process.

This appendix describes the FZP theory, and the calculation used for the design of FZP in our devices. It concludes with some preliminary results of various test lenses we have produced.

A.2 Fresnel Zone Plate Theory

The amplitude transmission function of a FZP is given by

$$t\left(r\right)=\frac{1}{2}\left[1+\operatorname{sgn}\left(\cos\left(\gamma r^{2}\right)\right)\right], \tag{A.1}$$

where $r=\sqrt{x^2+y^2}$ is the distance from the origin, the function sgn is the sign function, and γ is a real constant. In general, the function seen in Fig A.1 can be written as a Fourier series

$$f\left(x\right)=\sum_{m=-\infty}^{\infty}\frac{\sin\left(\pi m/2\right)}{\pi m}\exp\frac{i2\pi mx}{X}. \tag{A.2}$$

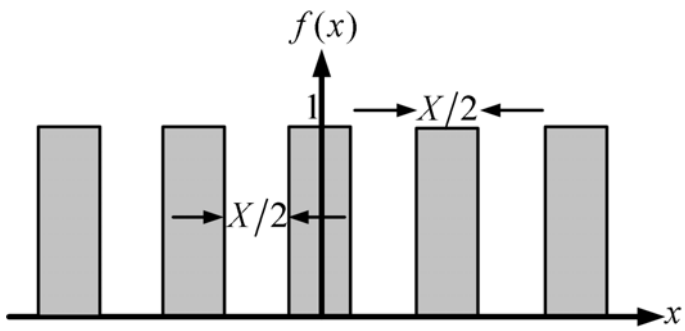

Figure A.1: Fresnel block diagram.

Thus,

$$t(r) = \sum_{m=-\infty}^{\infty} \frac{\sin(\pi m/2)}{\pi m} \exp\left(im\gamma r^2\right). \tag{A.3}$$

The transmission function of a lens with focal length f is given by

$$t_L(r) = \exp\left(-i\frac{\pi r^2}{\lambda f}\right), \tag{A.4}$$

where $\lambda = \lambda_0/n_s$ is the wavelength in Sapphire. Thus the term $\exp(im\gamma r^2)$ represents a lens with a focal length $f_m = -\pi/m\lambda\gamma$. The intensity of the terms in Eq. A.3 is given by

$$I_m = \frac{\sin^2(\pi m/2)}{(\pi m)^2} = \begin{cases} \frac{1}{4} & m = 0 \\ \frac{1}{(\pi m)^2} & m \text{ odd} \\ 0 & m \text{ even} \end{cases}. \tag{A.5}$$

Thus, the relative intensity of the term $m = 1$ is given by

$$\begin{aligned} I_{-1}\left(\sum_{m=-\infty}^{\infty} I_m\right)^{-1} &= \frac{1}{\pi^2}\left[\sum_{m=-\infty}^{\infty} \frac{\sin^2(\pi m/2)}{\pi^2 m^2}\right]^{-1} \\ &= \left[\frac{\pi^2}{4} + 2\sum_{m=0}^{\infty} \frac{1}{(2m+1)^2}\right]^{-1} \\ &= \left[\frac{\pi^2}{4} + 2\frac{\pi^2}{8}\right]^{-1} = \frac{2}{\pi^2} \simeq 0.2 \end{aligned} \tag{A.6}$$

Note - The width δ of a strip at radius $r >> \gamma^{-1/2}$ is found from $2\gamma r\delta = \pi$, thus the focal length for $m = 1$ can be expressed as

$$f_1 = \frac{\pi}{\lambda\gamma} = \frac{2r\delta}{\lambda}. \tag{A.7}$$

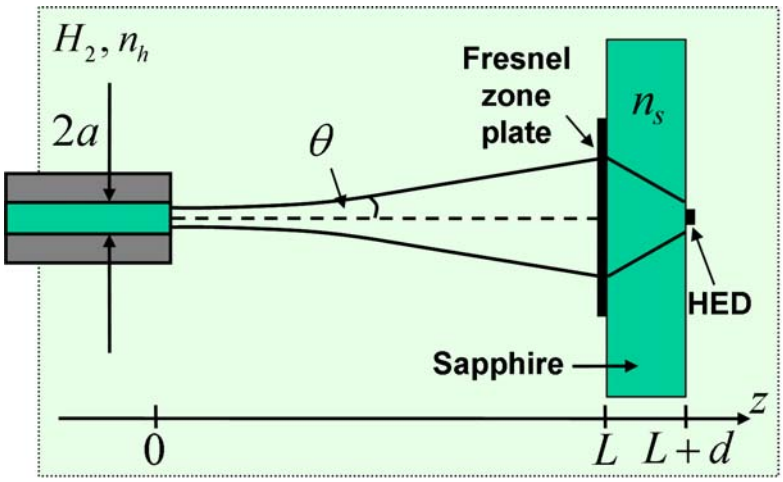

Figure A.2: Gaussian beam propagation.

For example, taking $r = 0.6\,\text{mm}$ one has

$$\delta = \frac{\pi}{2 \times (16.3\,\mu\text{m})^{-2} \times 0.6\,\text{mm}} = 0.695\,\mu\text{m}, \tag{A.8}$$

which is easily achieved with standard EBL process. Using Eq. A.1, one finds the radius of the central transparent circle is

$$r_0 = \sqrt{\frac{\pi}{2\,(16.3\,\mu\text{m})^{-2}}} = 20.4\,\mu\text{m} \tag{A.9}$$

A.3 Fresnel Zone Plate Design

The optical propagation path is view in Fig. A.2. The optical beam is assumed to have a Gaussian shape as given in Eq. A.26. The waist of the beam are found at the fiber edge, $z = 0$, thus $w\,(0) = w_0$ and $R\,(0) = \infty$. Assuming numerical aperture $\# = 0.13$, laser wave length $\lambda_0 = 1.55\,\mu\text{m}$, Helium refraction index $n_h = 1.026$, and using Eq. A.34 and Eq. A.30 one finds the smallest Gaussian beam (GB) radius w_0, and the Rayleigh length

$$w_0 = \frac{\lambda_0}{\pi n_h \#} = 3.699\,1\,\mu\text{m}, \tag{A.10}$$

$$z_0 = \frac{\pi w_0^2 n_h}{\lambda_0} = 28.455\,\mu\text{m}. \tag{A.11}$$

At the plane of the Fresnel zone plate (FZP) $z = L^-$ the Gaussian wave function is given by

$$\psi\left(z = L^-\right) = \psi_0 \frac{w_0}{w\,(L)} \exp\left[-i\,[kL - \eta\,(L)] - r^2\left(\frac{1}{w^2\,(L)} + \frac{ik}{2R\,(L)}\right)\right]. \tag{A.12}$$

For our Faraday package $L = 8.55\,\mathrm{mm}$, and the GB radius $w(L)$, and curvature $R(L)$ are calculated as

$$w(L) = \sqrt{w_0^2\left(1 + \frac{L^2}{z_0^2}\right)} = 1.14\,\mathrm{mm}, \tag{A.13}$$

$$R(L) = L\left(1 + \frac{z_0^2}{L^2}\right) \cong 8.55\,\mathrm{mm} \tag{A.14}$$

At the plane $z = L^+$ the Gaussian wave function is given by

$$\psi\left(z = L^+\right) = t(r)\,\psi\left(z = L^-\right), \tag{A.15}$$

where $t(r)$ is the transmission function of the FZP. Neglecting all terms with $m \neq 1$ in Eq. A.3 one finds for the plane $z = L^+$

$$\psi\left(z = L^+\right) = \frac{1}{\pi}\exp\left(i\gamma r^2\right)\psi\left(z = L^-\right). \tag{A.16}$$

The scalar field $\psi(z = L^+)$ is a GB with

$$\tilde{A} = \frac{1}{w^2(L)} + \frac{ik}{2R(L)} - i\gamma. \tag{A.17}$$

Using Eq. A.33 one finds that the waist of the beam is located at the plane of the photo detector $z = L + d$ if

$$\frac{\mathrm{Im}\,\tilde{A}}{\left|\tilde{A}\right|^2} = -\frac{2d}{k}, \tag{A.18}$$

and substituting Eq. A.17

$$\frac{\frac{k}{2R(L)} - \gamma}{\frac{1}{w^4(L)} + \left(\frac{k}{2R(L)} - \gamma\right)^2} = -\frac{2d}{k}, \tag{A.19}$$

thus

$$\frac{k}{2R(L)} - \gamma = \frac{k}{4d}\left[-1 \pm \sqrt{1 - \frac{16d^2}{w^4(L)\,k^2}}\right], \tag{A.20}$$

or keeping only lowest order terms of the small parameter of geometrical optics $1/k$

$$\frac{k}{2R(L)} - \gamma = -\frac{k}{2d}, \tag{A.21}$$

or

$$\gamma = \frac{k}{2}\left(\frac{1}{d} + \frac{1}{R(L)}\right), \tag{A.22}$$

where γ is inversely proportional to the FZP focal length, and is used as the design parameter of the lens. Assuming Sapphire refraction index $n_s = 1.74$ and width

$d = 1\,\mathrm{mm}$, one finds

$$\gamma^{-1/2} = \left[\frac{\pi}{\lambda_0}\left(\frac{n_s}{d} + \frac{1}{R(L)}\right)\right]^{-1/2} = 15.933\,\mu\mathrm{m} \tag{A.23}$$

The waist parameter at the plane of the HED is found using A.32

$$\tilde{w}_0^2 = \frac{\frac{1}{w^2(L)}}{\frac{1}{w^4(L)} + \left(\frac{k}{2R(L)} - \gamma\right)^2} = 0.242\,\mu\mathrm{m}, \tag{A.24}$$

The depth of focus is given by Eq. A.30,

$$\tilde{z}_0 = \frac{\pi w_0^2 n_s}{\lambda_0} = 0.216\,\mu\mathrm{m} \tag{A.25}$$

A.4 Preliminary results.

Using the design, which is described in the previous section, we have fabricated several FZP, having different γ values. The lenses are made of 1000 Å thick Nb on a Sapphire wafer, using EBL followed by direct RIE etching. Fig. A.3 (a) and (b) show a picture of the FZP taken with IR and regular CCD camera, respectively. The lens diameter is 1 mm, and the narrowest line has a width of approximately $0.5\,\mu$m. Fig. A.3 (c) shows the measured focal spot size, taken with IR CCD camera.

A.A Gaussian Beam Propagation

Consider a Gaussian beam (GB) propagating in the z direction. The scalar field $\psi(r,z)$ (where $r = \sqrt{x^2+y^2}$) is given by [55]

$$\psi = \psi_0 \frac{w_0}{w(z)} \exp\left[-i\left[kz - \eta(z)\right] - r^2 A(z)\right], \tag{A.26}$$

where the wave number $k = 2\pi n/\lambda_0$, n is the refraction index, λ_0 is the GB wavelength at vacuum, and

$$A(z) = \frac{1}{w^2(z)} + \frac{ik}{2R(z)}, \tag{A.27}$$

where the GB radius $w(z)$ is given by

$$w^2(z) = w_0^2\left(1 + \frac{z^2}{z_0^2}\right), \tag{A.28}$$

and the radius of curvature of the wave front is

$$R(z) = z\left(1 + \frac{z_0^2}{z^2}\right), \tag{A.29}$$

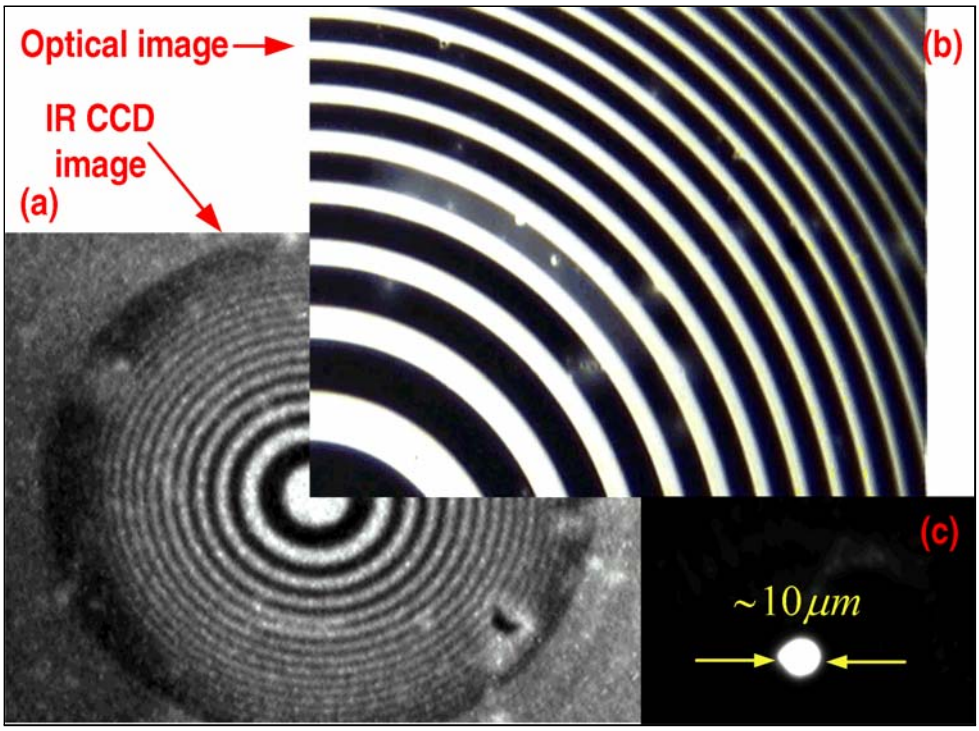

Figure A.3: (a) and (b) show a picture of the FZP taken with IR and regular CCD camera, respectively. The lance diameter is 1 mm, and the narrowest line has a width of approximately 0.5 μm. (c) shows the measured focal spot size.

the Rayleigh length (depth of focus) is

$$z_0 = \frac{\pi w_0^2 n}{\lambda_0} = \frac{k w_0^2}{2}, \tag{A.30}$$

and the Gouy phase shift is

$$\eta(z) = \tan^{-1}\left(\frac{z}{z_0}\right). \tag{A.31}$$

The following identities hold

$$\frac{\operatorname{Re} A}{|A|^2} = \frac{\frac{1}{w^2(z)}}{\frac{1}{w^4(z)} + \frac{k^2}{4R^2(z)}} = w_0^2, \tag{A.32}$$

$$\frac{\operatorname{Im} A}{|A|^2} = \frac{\frac{k}{2R(z)}}{\frac{1}{w^4(z)} + \frac{k^2}{4R^2(z)}} = \frac{2z}{k}. \tag{A.33}$$

The numerical aperture of the fiber, #, is related to the waist radius w_0 in the following way. For any given z the radius r for which $|\psi(r)/\psi(0)| = 1/e$ is given by $r = w_0\sqrt{1 + (z/z_0)^2}$. Thus, for $z >> z_0$ one has

$$r/z = \lambda_0/\pi w_0 n \simeq \#. \tag{A.34}$$

The fundamental mode HE_{11} of a step index fiber can be approximated as a Gaussian beam. The waist radius w_0 of the Gaussian is given by the following approximation [Pollock, *Optoelectronics*, page 144]

$$w_0/a = 0.65 + 1.619V^{-3/2} + 2.87V^{-6}, \tag{A.35}$$

where a is the radius of the core, and V *number* of the fiber is

$$V = \frac{2\pi a}{\lambda_0}\sqrt{n_{core}^2 - n_{clad}^2}. \tag{A.36}$$

A.B Beam intensity at plane of detector with no lens

The following calculation is used to calculate the ratio between the laser intensity at the edge of the optical fiber, and on the HED, where no Fresnel lens is used (current case). For $L_1 = L + d/n_s = 9.1397\,\mathrm{mm}$ one finds

$$w(L) = \sqrt{w_0^2\left(1 + \frac{L^2}{z_0^2}\right)} = 1.1881\,\mathrm{mm} \tag{A.37}$$

The irradiance distribution of the Gaussian is given by

$$I = \frac{2P}{\pi\omega^2} e^{-\frac{2r^2}{\omega^2}}.$$

Assuming a very small detector, so the intensity on the detector is uniform, the irradiation power on the detector is given by:

$$I = \frac{2P}{\pi\omega^2} A = 3.608 \times 10^{-6} P,$$

and dividing by the total power in the plane of the detector one finds the following scale factor

$$S_f = \frac{\frac{2P}{\pi\omega^2} A}{P \int_0^\infty \frac{2}{\pi\omega^2} e^{-\frac{2r^2}{\omega^2}} r dr} = 2.267 \times 10^{-5},$$

where A is the effective area of the detector.

Bibliography

[1] "Processing guidelines," *MicroChem*, 2001. [Online]. Available: http://www.microchem.com/products/pdf/PMMA_Data_Sheet.pdf

[2] "Efficient removers for poly(methylmethacrylate)," *J. Vac. Sci. Technol. B*, vol. 21, no. 1, pp. 91–97, Jan 2003.

[3] B. Abdo, E. Segev, O. Shtempluck, and E. Buks, "Nonlinear coupling in Nb/NbN superconducting microwave resonators," Jan. 2005, arXiv:cond-mat/0501236 v1.

[4] ——, "Observation of bifurcations and hysteresis in nonlinear NbN superconducting microwave resonators," *cond-mat/0501114 v2*, 2005.

[5] ——, "Intermodulation gain in nonlinear NbN superconducting microwave resonators," *Appl. Phys. Lett.*, vol. 88, no. 1, p. 022508, Jan. 2006.

[6] ——, "Nonlinear dynamics in the resonance lineshape of NbN superconducting resonators," *cond-mat/0601146*, 2006.

[7] S. M. Anlage, H. J. Snortland, and M. R. Beasley, "A current controlled variable delay superconducting transmission line," *IEEE Trans. Magn.*, vol. 25, no. 2, pp. 1388–1391, Mar. 1989.

[8] I. Balberg and H. Arbell, "Temperature as a bifurcation parameter in nonlinear electronic circuits," *Phys. Rev. E*, vol. 49, no. 1, pp. 110–113, Jan 1994.

[9] K. Chang, S. Martin, F. Wang, and J. L. Klein, "On the study of microstrip ring and varactor-tuned ring circuits," *IEEE Trans. Microwave Theory Tech.*, vol. MTT-35, no. 12, pp. 1733–1739, Dec. 1987.

[10] S. Cho and C.-S. Son, "Observation of bolometric optical response in superconducting microwave meander lines," *J. Appl. Phys.*, vol. 84, no. 10, pp. 5657–5661, Nov. 1998.

[11] S. Cho, J.-C. Park, and C. Lee, "Current and temperature controlled variable inductance insuperconducting microstrip lines," *IEEE Trans. Appl. Superconduct.*, vol. 11, no. 1, pp. 3090–3093, Mar. 2001.

[12] S. Cho and C.-S. Son, "Modulation of the resonance frequency of superconducting microwave resonators," *IEEE Trans. Appl. Superconduct.*, vol. 13, no. 2, pp. 3659–3662, Jun. 2003.

[13] R. E. Collin, *Foundations for Microwave Engineering*, 2nd ed. New York: McGraw-Hill, 1992, pp. 538-541.

[14] T. Dahm and D. J. Scalapino, "Theory of intermodulation in a superconducting microstrip resonator," *J. Appl. Phys.*, vol. 81, no. 4, pp. 2002–2009, Feb. 1997.

[15] P. K. Day, H. G. LeDuc, B. A. Mazin, A. Vayonakis, and J. Zmuidzinas, "A broadband superconducting detector suitable for use in large arrays," *Nature*, vol. 425, pp. 817–821, Oct. 2003.

[16] B. Delaeta, J.-C. Villegierb, W. Escoffierb, J.-L. Thomassinb, P. Feautriera, I. Wangc, P. Renaud-Goudc, and J.-P. Poizat, "Fabrication and characterization of ultra-thin NbN hot electron bolometer for near infrared single photon detection," *Nucl. Instr. and Meth. A*, vol. 520, pp. 541–543, 2004.

[17] V. Dimitrova, D. Manova, T. Paskova, T. Uzunov, N. Ivanov, and D. Dechev, "Aluminium nitride thin films deposited by DC reactive magnetron sputtering," *Vacuum*, vol. 51, no. 2, pp. 161–164, 1998.

[18] V. V. Dodonov and A. B. Klimov, "Generation and detection of photons in a cavity with a resonantly oscillating boundary," *Phys. Rev. A*, vol. 53, no. 4, pp. 2664–2682, Apr. 1996.

[19] M. J. Feigenbaum, "Quantitative universality for a class of nonlinear transformations," *J. Stat. Phys.*, vol. 19, no. 1, pp. 25–52, Jul. 1978.

[20] N. V. Fomin, O. L. Shalaevand, and D. V. Shantsev, "Parametric resonance in superconducting micron-scale waveguides," *J. Appl. Phys.*, vol. 81, no. 12, pp. 8091–8096, Jun. 1997.

[21] C. W. Gardiner and M. J. Collett, "Input and output in damped quantum systems: Quantum stochastic differential equations and the master equation," *Phys. Rev. A*, vol. 31, pp. 3761–3774, 1985.

[22] P. Gardner, D. K. Paul, and K. P. Tan, "Planar microstrip ring resonator filters," *Antennas for Personal Communication Systems, IEE Colloquium*, pp. 6/1 – 6/6, Feb. 1994.

[23] M. A. Golosovsky, H. J. Snortland, and M. R. Beasley, "Nonlinear microwave properties of superconducting Nb microstrip resonators," *Phys. Rev. B*, vol. 51, no. 10, pp. 6462–6469, 1995.

[24] G. N. Goltsman, A. Korneev, I. Rubtsova, I. Milostnaya, G. Chulkova, O. Minaeva, K. Smirnov, B. Voronov, W. Sysz, A. Pearlman, A. Verevkin, and R. Sobolewski, "Ultrafast superconducting single-photon detectors for near-infrared-wavelength quantum communications," *Phys. Status Solidi C*, vol. 2, no. 5, pp. 1480–1488, 2005.

[25] G. N. Goltsman, K. Smirnov, P. Kouminov, B. Voronov, N. Kaurova, V. Drakinsky, J. Zhang, A. Verevkin, and R. Sobolewski, "Fabrication of nanostructured superconducting single-photon detectors," *IEEE Trans. Appl. Superconduct.*, vol. 13, no. 2, pp. 192–195, Jun. 2003.

[26] G. K. Gopalakrishnan, B. W. Fairchild, C. L. Yeh, C.-S. Park, K. Chang, M. H. Weichold, and H. F. Taylor, "Experimental investigation of microwave-optoelectronic interactions in a microstrip ring resonator," *IEEE Trans. Microwave Theory Tech.*, vol. 39, no. 12, pp. 2052–2060, Dec. 1991.

[27] D. Gu, Y. Zhuang, and S. Yngvesson, "Bistability in NbN HEB mixer devices," $14^{th} ISSTT03$, 2003.

[28] ——, "New results on bistability effects in HEB devices," $15^{th} ISSTT04$, 2004.

[29] A. V. Gurevich and R. G. Mints, "Self-heating in normal metals and superconductors," *Rev. Mod. Phys.*, vol. 59, no. 4, pp. 941–999, Oct. 1987.

[30] M. W. Johnson, A. M. Herr, and A. M. Kadin, "Bolometric and nonbolometric infrared photoresponses in ultrathin superconducting NbN films," *J. Appl. Phys.*, vol. 79, pp. 7069–7074, 1996.

[31] A. M. Kadin and M. W. Johnson, "Nonequilibrium photon-induced hotspot: A new mechanism for photodetection in ultrathin metallic films," *Appl. Phys. Lett.*, vol. 69, no. 25, pp. 3938–3940, Dec. 1996.

[32] J. Kitaygorsky, J. Zhang, A. Verevkin, A. Sergeev, A. Korneev, V. Matvienko, P. Kouminov, K. Smirnov, B. Voronov, G. GolŠtsman, and R. Sobolewski, "Origin of dark counts in nanostructured NbN single-photon detectors," *IEEE Trans. Appl. Superconduct.*, vol. 15, no. 2, pp. 545–548, Jun. 2005.

[33] A. Korneev, P. Kouminov, V. Matvienko, G. Chulkova, K. Smirnov, B. Voronov, G. N. Goltsman, M. Currie, W. Lo, K. Wilsher, J. Zhang, W. Slysz, A. Pearlman, A. Verevkin, and R. Sobolewskic, "Sensitivity and gigahertz counting performance of NbN superconducting single-photon detectors," *Appl. Phys. Lett.*, vol. 84, no. 26, pp. 5338–5340, Jun. 2004.

[34] L. Landau and E. Lifshits, *Mechanics.* New York: Oxford, 1976.

[35] J. Lee, H. Cho, D. C. Hays, C. R, Abernathy, S. J. Pearton, R. J. Shul, G. A. Vawter, and J. Han, "Dry etching of GaN and related materials: Comparison of techniques," *IEEE J. Select. Topics Quantum Electron.*, vol. 4, no. 3, pp. 557–563, May 1998.

[36] J.-C. Lee, H. F. Taylor, and K. Chang, "Degenerate parametric amplification in an optoelectronic GaAs CPW-to-slotline ring resonator," *IEEE Microwave Guided Wave Lett.*, vol. 7, no. 9, pp. 267–269, Sep. 1997.

[37] A. Lichtenberger, D. Lea, and F. Lloyd, "Investigation of etching techniques for superconducting Nb/Al-Al_2O_3/Nb fabrication processes," *IEEE Trans. Appl. Superconduct.*, vol. 3, no. 1, pp. 2191–2196, Mar. 1993.

[38] P. S. Linsay, "Period doubling and chaotic behavior in a driven anharmonic oscillator," *Phys. Rev. Lett.*, vol. 47, no. 19, pp. 1349–1352, Nov. 1981.

[39] A. Mahmood, N. Rakov, and M. Xiao, "Nfluence of deposition conditions on optical properties of aluminum nitride (AlN) thin films prepared by DC-reactive magnetron sputtering," *Mater. Lett.*, vol. 57, pp. 1925–1933, 2003.

[40] D. Manova, V. Dimitrova, W. Fukarek, and D. Karpuzovc, "Investigation of d.c.-reactive magnetron-sputtered AlN thin films by electron microprobe analysis, x-ray photoelectron spectroscopy and polarised infra-red reflection," *Surf. Coat. Technol.*, vol. 106, pp. 205–208, 1998.

[41] T. S. Martin, F. Wang, and K. Chang, "Theoretical and experimental investigation of novel varactor-tuned switchable microstrip rmg resonator circuits," *IEEE Trans. Microwave Theory Tech.*, vol. 36, no. 12, pp. 1733–1739, Dec. 1988.

[42] R. M. May, "Simple mathematical models with very complicated dynamics," *Nature*, vol. 261, p. 459, Jun. 1976.

[43] M. A. McCord and M. J. Rooks, *Handbook of Microlithography, Micromachining, and Microfabrication*, P. Rai-Choudhury, Ed. Wa: Bellingham, 1997, vol. 1: Microlithography, chapter 2. [Online]. Available: HTTP//www.cnf.cornell.edu/cnf_spietoc.html

[44] J. R. Mileham, S. J. Pearton, C. R. Abernathy, J. D. MacKenzie, R. J. Shul, and S. P. Kilcoyne, "Wet chemical etching of AlN," *Appl. Phys. Lett.*, vol. 67, no. 8, pp. 1119–1121, Aug. 1995.

[45] R. Monaco, A. Andreone, and F. Palomba, "Intermodulation measurements in nb superconducting microstrip resonators," *j. Appl. Phys.*, vol. 88, no. 5, pp. 2898–2905, Sep. 2000.

[46] R. Movshovich, B. Yurke, P. G. Kaminsky, A. D. Smith, A. H. Silver, R. W. Simon, and M. V. Schneider, "Observation of zero-point noise squeezing via a josephson-parametric amplifier," *Phys. Rev. Lett.*, vol. 65, no. 12, pp. 1419–1422, Sep. 1990.

[47] S. J. Pearton and C. R. Abernathy, "Low bias electron cyclotron resonance plasma etching of GaN, AIN, and InN," *Appl. Phys. Lett.*, vol. 64, no. 17, pp. 2294–2296, Apr. 1994.

[48] D. Saeedkia, A. H. Majedi, S. Safavi-Naeini, and R. R. Mansour, "Frequency and time-varying scattering parameters of a photo-excited superconducting microbridge," *IEEE Microwave Wireless Compon. Lett.*, vol. 15, no. 8, pp. 510–512, Aug. 2005.

[49] B. C. Sanders and G. J. Milburn, "Complementarity in a quantum nondemolition measurement," *Phys. Rev. A*, vol. 39, no. 2, pp. 694–702, Jan. 1989.

[50] K. W. U. Strom, S. A. Wolf, and D. U. Gubser, "Use of granular NbN as a superconducting bolometer," *J. Appl. Phys.*, vol. 52, pp. 4888–4889, 1981.

[51] M. Tsindlekht, M. Golosovsky, H. Chayet, and D. Davidov, "Frequency modulation of the superconducting parallel-plate microwave resonator by laser irradiation," *Appl. Phys. Lett.*, vol. 65, no. 22, pp. 2875–2877, Nov. 1994.

[52] R. Wedenig, T. Niinikoski, P. Berglund, J. K. R. Inen, L. Costa, M. Valtonen, R. Linna, J. Salmi, H. SeppaK, and I. Suni, "Superconducting NbN microstrip detectors," *Nucl. Instrum. Methods Phys. Res. A*, vol. 443, no. 3, pp. 646–663, Sep. 1999.

[53] K. Wiesenfeld and B. McNamara, "Period-doubling systems as small-signal amplifiers," *Phys. Rev. Lett.*, vol. 55, no. 1, pp. 13–16, Jul. 1985.

[54] K. R. Williams, K. Gupta, and M. Wasilik, "Etch rates for micromachining processing - part II," *J. Microelectromech. Syst.*, vol. 12, no. 6, pp. 761–778, Dec. 2003.

[55] A. Yariv, *Quantum Electronics*, 3rd ed. New York: Wiley, 1989, pp. 46-49.

[56] B. Yurke, P. G. Kaminsky, R. E. Miller, E. A. Whittaker, A. D. Smith, A. H. Silver, and R. W. Simon, "Observation of 4.2-k equilibrium-noise squeezing via a josephson-parametric amplifier," *Phys. Rev. Lett.*, vol. 60, no. 9, pp. 764–767, Feb. 1988.

[57] ——, "Observation of 4.2-k equilibrium-noise squeezing via a josephson-parametric amplifier," *IEEE Trans. Magn.*, vol. 25, no. 9, pp. 1371–1375, Feb. 1989.

[58] B. Yurke, "Squeezed-coherent-state generation via four-wave mixers and detection via homodyne detectors," *Phys. Rev. A*, vol. 32, no. 1, pp. 300–310, Jul. 1985.

[59] B. Yurke and E. Buks, "Performance of cavity-parametric amplifiers, employing kerr nonlinearites, in the presence of two-photon loss," *arXiv:quant-ph/0505018 v1*, pp. 1–9, 2005.

[60] J. Zhang, W. Slysz, A. Pearlman, A. Verevkin, R. Sobolewski, O. Okunev, G. Chulkova, and G. N. Goltsman, "Time delay of resistive-state formation in superconducting stripes excited by single optical photons," *Phys. Rev. B*, vol. 67, 132508, 2003.

[61] J. Zhang, W. Slysz, A. Verevkin, O. Okunev, G. Chulkova, A. Korneev, A. Lipatov, G. N. Goltsman, and R. Sobolewski, "Response time characterization of NbN superconducting single-photon detectors," *IEEE Trans. Appl. Superconduct.*, vol. 13, no. 2, pp. 180–183, Jun. 2003.